

Preparation of supported metal catalysts via thermo-destabilization of microemulsions

vorgelegt von

M.Sc. Riny Yolandha Parapat

Aus Jakarta, Indonesia

der Fakultät II - Mathematik und Naturwissenschaften
der Technischen Universität Berlin
zur Erlangung des akademischen Grades
Doktor der Naturwissenschaften

-Dr.rer.nat.-

genehmigte Dissertation

Promotionsausschluss:

Vorsitzender: Prof. Dr. M. A. Mroginski

Berichter: Prof. Dr. R. Schomäcker

Berichter: Prof. Dr. C. Stubenrauch

Verteidigung am: 25. Oktober. 2013

Berlin 2014

D 83

To:

My dearly beloved Lord Jesus Christ,

The one whom I love to the uttermost



I pray that
out of His glorious riches,
He may strengthen you with power
through His Spirit
into your inner being,
so that Christ may dwell in your heart through faith.

And I pray that you,
being rooted and established in love,
may have power,
together with all of the Lord's holy people,
to grasp how wide and long and high and deep is
the love of Christ,
and to know this love surpasses knowledge
that you may be filled to the measure
of all the fullness
of God."

~Ephesians 3:16-19

Acknowledgements

I thank and praise God Almighty, my heavenly Father, and to my savior and beloved, the Lord Jesus Christ, whom I trust, and to the Holy Spirit who has been my help, strength and wisdom to complete this work. The Triune God is the one who get the glory and honor.

I would like to express my sincere appreciation and deep gratitude to my supervisor, Prof. Reinhard Schomäcker for his encouragement and guidance throughout the stages of my Ph.D. studies. I am thankful for the pleasant working environment and many important learning opportunities.

My thanks particularly go to Michael Schwarze for the nice cooperation and to Patrick Littlewood for valuable help and comments on the manuscripts. I would also like to thank Sören Selve for performing the TEM/HRTEM investigations and to Astrid Müller for assisting with the ICP measurements. To Veronica, Mulianny, Anton, and Henky, I really thank you for your contributions. Thanks to Gabi Vetter for all her generous help in the laboratory and also extended to all my colleagues in TC-08 particularly for all the friendship and support during my research.

I gratefully acknowledge financial help from the Directorate General of Higher Education of Indonesia (Dikti) and from Unicat Project of TU- Berlin.

Finally, and most importantly, I would like to thank family in Indonesia especially to my mother, who always pray for me. I thank God for the church in Berlin, for their prayer, support and genuine love. Without their spiritual and emotional support, I would not have made it this far.

Berlin, October 2013

Riny Yolanda Parapat

Abstract

The physical and chemical properties of metal nanoparticles depend mostly on their size and shape. Therefore, it is very important to develop synthetic routes that give non-agglomerated, well-controlled size and shape with a narrow size distribution. Many researchers have successfully produced small Pt particles with different shapes; however, they still remain in the colloidal state which can only be stable for a limited time. A new technique to deposit small nanoparticles synthesized in reverse micellar microemulsions onto support material without agglomeration, namely thermal-destabilization of microemulsions, is presented in this study. The microemulsion components in the first attempt are Triton X-100, pentanol, cyclohexane, and either H_2PtCl_6 or N_2H_4 in the water phase. Characterization included ICP, SEM, TEM, IR, XRD, UV spectrophotometry and Zeta Potential measurement. The hydrogenation of α -methyl styrene and methyl crotonate served as catalytic testing reactions

When using the N_2H_4 as the reductant, the multifaceted Pt crystals, mostly truncated octahedron, were produced at room temperature with an average size of 2.5 nm and a narrow size distribution. After deposition, the Pt crystals were found to be well dispersed on the support with an average size of 2.5 nm. After testing with hydrogenation of α -methyl styrene, the Pt-catalyst showed higher activity (6 times higher) than commercial ones. The performance of the catalyst is optimized by keeping the small size but changing the shape of Pt nanocrystals to anisotropic structure by means of a weaker reducing agent such as ascorbic acid. The catalyst activity is further improved by changing the metal precursor to K_2PtCl_4 . We found that our catalysts are 3-4 times more active than those we prepared with N_2H_4 as the reductant.

The parameters that significantly influence the activity of the produced catalysts are the heating rate during thermal destabilization process, molar ratio of water to surfactant (ω), initial molar ratio metal to reducing agent, growing time, zeta potentials of the particles, pretreatment of the support, and calcinations temperature. Preparation of other supported metal nanoparticles such as Pd, Ru and Ag catalysts are also studied to elucidate the recipe. Testing the produced Ru and Pt catalysts with a challenging reaction such as hydrogenation of levulinic acid shows that their conversions are better ($\sim 20\%$) than those are prepared by other researchers even with milder reaction condition. The insignificant difference of activity ($< 1\%$) of produced catalyst from different batches indicates that this method is adaptable and reproducible.

Kurzfassung

Die physikalischen und chemischen Eigenschaften von Metall-Nanopartikeln werden stark durch ihre Größe und Form bestimmt. Daher ist es wichtig, Syntheserouten zu entwickeln, die eine Herstellung von nicht agglomerierten Nanopartikeln mit gut kontrollierbaren Größen und Formen erlauben. Viele Forscher haben erfolgreich Platin-Nanopartikel mit verschiedenen Größen erzeugt, die nach der Synthese weiterhin in kolloidalen Dispersionen vorliegen, die nicht dauerhaft stabil sind. Eine neue Technik, die die Herstellung und Abscheidung von Platin-Nanopartikeln auf Trägermaterialien aus w/o-Mikroemulsionen ohne deren Agglomeration erlaubt, ist Gegenstand dieser Arbeit. Dafür wurde eine Auswahl der Tenside und Lösungsmittel zur Herstellung der Mikroemulsionen vorgenommen. Die erzeugten Partikel wurden mit Hilfe von ICP, SEM, TEM, XRD und UV-Spektroskopie und Zetapotenzialmessungen charakterisiert. Die katalytischen Eigenschaften wurden durch die Hydrierungen von α -Methylstyrol und Methylcrotonat getestet.

Vielfach facettierte Platin-Kristallite, häufig abgeflachte Octaeder, wurden bei Raumtemperatur in inversen Mizellen mit mittleren Durchmessern von 2,5 Nanometern bei enger Partikelgrößenverteilung hergestellt. Diese Partikel konnten ohne Agglomeration auf Trägermaterialien abgeschieden werden. In der Hydrierung von α -Methylstyrol zeigen die Katalysatoren eine höhere Aktivität als kommerzielle Katalysatoren. Durch den Einsatz von Ascorbinsäure als Reduktionsmittel wurden Partikel gleicher Größe aber mit anisotroper Form erzeugt, die eine noch höhere Aktivität zeigen. Eine weitere Aktivitätssteigerung wurde durch den Wechsel des Platin-Precursors von H_2PtCl_6 zu K_2PtCl_4 erreicht.

Die Syntheseparameter, die die Aktivität der resultierenden Katalysatoren beeinflussen, sind die Heizrate während des Abscheidungsprozesses, die Größe der inversen Mizellen, das stöchiometrische Verhältnis von Metall Precursor zu Reduktionsmittel, das Zetapotenzial und die Vorbehandlung des Trägermaterials sowie die Kalzinierungstemperatur. Die Übertragung der Präparationsmethode auf die Herstellung von Palladium-, Ruthenium und Silber-Nanopartikel zeigte vergleichbare Ergebnisse und dieselben Abhängigkeiten. Ein Test der so hergestellten Ruthenium-Katalysatoren in einer schwierigen Reaktion wie der Hydrierung von Levulinsäure zeigte deutlich bessere Ergebnisse als mit anderen Katalysatoren bislang erreicht wurden. Dabei zeigt sich eine gute Übertragbarkeit und Reproduzierbarkeit der entwickelten Synthesestrategie auf andere Metalle.

Table of Contents

Acknowledgement	iii
Abstract	iv
Kurzfassung	v
Table of Contents	vi
1. Introduction	15
2. Design and synthesis of supported metal catalyst	24
2.1 Synthesis of metal nanoparticles via reverse micelles	25
2.1.1 Mechanism of nanocrystals formation	25
2.1.2 Mechanism of particles formation in microemulsions	26
2.2 Size and shape control of metal nanoparticles	31
2.2.1 Thermodynamic Control	33
2.2.2 Kinetic control	34
2.3 Growth mechanism in metal reduction	38
2.4. Preparation of supported catalysts with microemulsions	42
3. General Experimental Section	47
3.1 Chemicals	47
3.2 Experimental Procedure	48
3.2.1 Phase Behaviour of Microemulsion Systems	48
3.2.2. Synthesis of supported metal nanoparticles	50
3.2.3. Catalytic testing	53
3.3 Catalyst performance	55
3.4 Catalyst characterization	56
3.4.1 Transmission Electron Microscopy (TEM)	56
3.4.2 Scanning Electron Microscope (SEM)	57

3.4.3 Inductively Coupled Plasma Optical Emission Spectroscopy (ICP-OES)	57
3.4.4 BET surface area measurement	58
3.4.5 X-Ray Diffraction (XRD)	59
3.4.6 Zeta potential (ζ -potential)	60
3.4.7. UV-Vis spectrometer	60
4. A new method to synthesize very active and stable supported metal Pt catalysts: thermo-destabilization of microemulsions	61
4.1 Introduction	61
4.2 Experimental Section	65
4.2.1 Materials	65
4.2.2 Catalyst Preparation	66
4.3 Results and discussion	70
4.3.1 Choosing the surfactant and co-surfactant	70
4.3.3 Choosing the precursor	72
4.3.4 The effect of the heating rate	72
4.3.5 Effect of the support feeding prior to deposition process	73
4.3.6 Effect of the growing time	73
4.3.7 The effect of the initial concentration ratio	77
4.3.8 The deposition process by thermal-destabilization method	78
4.3.9 Effect of the support material and comparison with other catalysts	82
4.3.10 Effect of calcinations	83
4.3.11 Other Parameters	85
4.3.12 Stability test	85
4.4 Conclusion	87
5. Particle shape optimization by changing from isotropic to anisotropic nanostructure	90
5.1. Introduction	90
5.2. Experimental Section	93
5.2.1 Materials	93
5.2.2 Catalyst Preparation	93
5.3 Results and discussion	95

5.3.1	Effect of reducing agent on catalytic activity.	95
5.3.2	Structure of Pt nanodendrites in reverse micelles	96
5.3.3	Effect of support acidity on catalytic activity	98
5.3.4	Effect of pH on the structure of nanodendrites	101
5.3.5	Effect of metal precursor on catalytic activity	104
5.3.6	Catalytic testing with different substrates	105
5.3.7	Stability testing	105
5.4.	Conclusion	107
6.	Preparation of Pd, Ru and Ag supported metal catalysts	110
6.1	Microemulsion composition for the synthesis of metal nanoparticles	111
6.2	Effect of growth time	113
6.3	Effect of feeding rate	115
6.4	Effect of initial concentration of metal precursor	116
6.5	Effect of the Zeta potential to the deposition yield and the activity	118
6.6	Effect of the support type to the activity	121
6.7	Effect of pre-calcination of the support	122
6.8	The activity of supported metal catalysts in hydrogenation of AMS	126
6.9	The activities of supported metal catalysts in hydrogenation of Levulinic Acid	128
6.10	Conclusion	128
7.	Conclusion	133
	Appendix	136
	A. Physical and Chemical Properties	137
	B. Experimental Data	139
	C. Calculations	146

List of Figures

Figure 1.1	Face-centered cubic (fcc) metals with low index facets.....	16
Figure 1.2	Face-centered cubic (fcc) metals with high index facets.....	17
Figure 1.3	Illustration of terrace, kink and step in a crystal structure.....	18
Figure 1.4	Unit stereographic triangle of fcc metal single-crystal and models of surface atomic arrangement (from ref 16).....	19
Figure 2.1	Plot of atomic concentration against time according to La Mer model for the generation of atoms, nucleation, and subsequent growth of colloidal synthesis.	26
Figure 2.2	Schematic diagram of the nucleation and growth process showing the dependence of the Gibbs free energy (ΔG) on the crystal size. Reversible process takes place below a critical radius (r^*) and turn to irreversible when $r > r^*$. (Modified from Dalmaschio et.al ³)	27
Figure 2.3	Schematic representation of a fused dimer after a two droplets collision showing the channel opened in between. (Modified from the ref. 12).....	30
Figure 2.4	A schematic illustration of the reaction pathways that lead to metal nanostructures with different shapes. The green, orange, and purple colors represent the $\{100\}$, $\{111\}$, and $\{110\}$ facets, respectively. The parameter R is defined as the ratio between the growth rates along the $\langle 100 \rangle$ and $\langle 111 \rangle$ axes. (Modified from ref. 8).....	32
Figure 2.5	Size-distribution focusing (a.u., arbitrary units).....	35
Figure 2.6	Illustration of the kinetic shape control by selective adhesion of surfactant.....	38
Figure 2.7	Schematic representations of reaction pathways controlled by reductants. When the metal precursor PtCl_4^{2-} ions are reduced by a weak reductant, the intermediate $\text{Cl}_3^2\text{-Pt} - \text{PtCl}_3^{2-}$ dimer and the subsequent dimer clusters and their aggregations into higher linear ' Pt_nCl_x ' complexes are formed in the nucleation stage. For the stronger reducing agent, PtCl_4^{2-} ions are reduced into Pt^0 atom which then aggregated into Pt_2^0 , Pt_3^0 and large Pt_n^0 clusters. (Modified from Yao et al. ⁴⁶).....	41
Figure 3.1	Schematic illustration of the experiment to prepare a fish diagram.....	49
Figure 3.2	The reactor setup for synthesis of supported nanoparticles with thermo-destabilization of microemulsions method.....	52
Figure 3.3	The hydrogenation reactor setup for catalytic testing.....	53

Figure 3.4	The excel program for the hydrogenation reaction.....	54
Figure 3.5	List of hydrogenation reactions for catalytic testing.....	55
Figure 4.1	Mechanism of Pt nanoparticle formation	62
Figure 4.2	Principle of the deposition process for Pt nanoparticles via thermo-destabilisation of μ E: schematic phase prism (upper right), schematic experimental setup for phase behaviour observation (upper left), flowchart of synthesis (bottom left), and illustration of the deposition process.....	64
Figure 4.3	A representative profile of AMS hydrogenation with 0.01% Pt/ Al_2O_3 at 20 °C and 1 bar.....	69
Figure 4.4	Phase diagram of microemulsions with equal amounts of oil and water ($\alpha = 0.5$) as a function of surfactant concentration (ψ) and temperature for four different surfactants.....	71
Figure 4.5	The activities of the produced catalysts prepared in different heating rates	73
Figure 4.6	The activities of the Pt-catalysts prepared in different support feeding prior to deposition process.....	74
Figure 4.7	The activities of the produced catalysts prepared in different growing times and the corresponding TEM images: a,b,c are the Pt particles after growing 1 min, 15 min and 30 min respectively.	75
Figure 4.8	Activities of the Pt-catalysts prepared with different ratios of initial concentrations.....	77
Figure 4.9	Phase diagrams of microemulsions and the ranges of temperature of deposition, $\alpha_1 = 0.5$ (left) and $\alpha_2 = 0.92$ (right).....	78
Figure 4.10	TEM images of Pt nanoparticles inside of the microemulsions before and after deposition process at different ω and their corresponding size distributions.....	79
Figure 4.11	EDX analysis of one sample of the produced supported Pt catalysts which shows the location Pt-metal on the surface of the Al_2O_3	83
Figure 4.12	The activities of the Pt catalysts (upper) and the corresponding TEM-images (bottom). The scale bars are 10 nm.	84
Figure 4.13	The activities of the Pt catalysts prepared in different temperature of calcinations and the corresponding TEM images. Each calcinations temperature was held for 2 h.....	85
Figure 4.14	Six hydrogenation runs of 1 g of AMS: a) conversion vs time, b) initial reaction rate of each hydrogenation run c) and d) TEM images of synthesized 0.1% Pt@ γ - Al_2O_3 before and after the hydrogenation reactions.....	86

Figure 5.1	Illustration of the role of the reducing agent to produce different shapes of Pt nanoparticles.....	96
Figure 5.2	Pt clusters produced with ascorbic acid as reductant in the presence of the surfactant (A), in the absence of the surfactant (B), HRTEM of a branch of Pt dendrite (C), and its Fast Fourier transform (FFT) with the lattice indexes (D)	97
Figure 5.3	Upper left: activities of Pt catalysts reduced with either hydrazine or AA and deposited on acidic (A), neutral (B), basic (C) alumina supports. Upper right: degrees of dispersion of the corresponding catalysts with the Delaunay network method (Modified with permission from Ref 27). Middle and bottom are the TEM and SEM images of the corresponding catalysts respectively.	100
Figure 5.4	Pt nanodendrites supported on acidic Al ₂ O ₃ prepared with different initial molar ratios of Pt to AA, 1:25 (left) and 1: 50 (right). The upper and bottom insets are the corresponding TEM images with low magnification and the particle size distributions (100 particles were counted).	101
Figure 5.5	Activities of the Pt nanodendrites deposited on SBA-prepared in different molar ratio Pt to AA and the corresponding TEM images (inset).....	102
Figure 5.6	Activities of the supported Pt catalysts prepared with hydrazine and ascorbic acid as reductants and the corresponding TEM images.	103
Figure 5.7	Upper: Activities of the supported Pt catalysts produced from different Pt precursors, K ₂ PtCl ₄ (A) and H ₂ PtCl ₆ (B), and the corresponding TEM images for basic Al ₂ O ₃ . Bottom: the corresponding HRTEM images of Pt nanodendrites inside of reverse micelles. The branches of Pt dendrites were separated and always moving when they were exposed to high voltage electron beams during the TEM investigation.	104
Figure 5.8	Activity testing of Pt/Al ₂ O ₃ prepared via the Thermo-destabilization method (*) compared to commercial Pt/Al ₂ O ₃ for the hydrogenation reaction. All reactions were performed at 20°C and 1.1 bar, except levulinic acid hydrogenation: 70 °C and 1.3 bar.....	106
Figure 5.9	Stability test of Pt/Al ₂ O ₃ catalyst that produced with ascorbic acid.....	107
Figure 6.1	Left: Phase behaviour ‘fish diagrams’ of microemulsions (water-cyclohexane-pentanol-Triton X100) at different oil compositions (α). Right: TEM images of the Pt nanoparticles in the w/o microemulsion prepared according to the value of the corresponding ω (molar ratio of water to surfactant) that is shown in the fish diagrams.....	112
Figure 6.2	The growth profiles of Ag nanoparticles with different amount of metal precursor in the microemulsion (left) look like the profile of the La Mer model for nucleation and growth of particle in colloidal synthesis (right).	114

Figure 6.3	Activities of 0.1%-wt Pd/Al ₂ O ₃ and 0.04%-wt Ru/Al ₂ O ₃ prepared with different growing time. Both catalysts were tested in hydrogenation of methyl crotonate at 20 °C 1.1 bar.	114
Figure 6.4	Differences in catalytic activity of Pt and Pd catalysts for the hydrogenation reactions of alpha methyl styrene (left) and methyl crotonate (right) caused by different feeding method. Both catalysts were prepared with ascorbic acid as the reductant.	115
Figure 6.5	Activities of supported metal catalysts prepared with different initial metal concentrations and with slow feeding rate of reductant. Left : Pd/Al ₂ O ₃ prepared with AA as reductant. Right : Ru/Al ₂ O ₃ prepared with hydrazine as reductant. Both catalysts were tested in hydrogenation of methyl crotonate at 20 °C and 1.1 bar.	117
Figure 6.6	Schematic illustration of Ag nanoparticle deposition onto the acidic alumina. Ions adsorb onto the surface of the Ag nanoparticles creating an electrical double layer. The potential in second layer is measured as a Zeta potential.	119
Figure 6.7	Left: Deposition percentage of different metals on basic Al ₂ O ₃ with thermo-destabilization method. The amount metal precursor prepared in each microemulsions system is 6 mg. Right: The yield of Ag deposition on acidic, basic and neutral alumina. The high deposition yield of Ag to all the supports because of the big difference of the zeta potentials between Ag (-50 mV) and acidic, neutral and basic alumina (+45, +40, +10, respectively).	120
Figure 6.8	Loading of different metal catalysts on basic alumina as function of the amount (mg) of corresponding metal in the precursor solutions. The slope that is shown in each profile indicates the affinity metal particles to the support material.	121
Figure 6.9	Activities of Pd dan Ru catalyst supported on different acidity of Al ₂ O ₃ in hydrogenation of methyl crotonate. The inset is activities of Pt catalyst supported on different acidity of Al ₂ O ₃ in hydrogenation of α-methyl styrene. The opposite trend of activities nbetween Pt catalyst and Pd and Ru catalyst is because of the the different value of zeta potential.	122
Figure 6.10	Activities of Pd dan Ru catalyst supported on different support material in hydrogenation of methyl crotonate at 20 °C and 1.1 bar.	123
Figure 6.11	SEM images of supported Pd catalysts (left) and the corresponding EDX (right): Pd/MCM-41 (top), Pd/SBA-15 (middle), Pd/Al ₂ O ₃ (bottom).	124
Figure 6.12	SEM images of supported Ru catalysts (left) and the corresponding EDX (right): Ru/MCM-41 (top) and Pd/SBA-15 (bottom).	125
Figure 6.13	Effect of precalcinations to the catalytic activity of Pd particles supported on basic alumina and the corresponding SEM images.	127

- Figure 6.14** Activities of different supported metal catalysts prepared with different reducing agents (N_2H_4 and AA), in hydrogenation of α -methyl styrene..... 128
- Figure 6.15** Morphology of Pd (upper) and Pt (bottom) nanoparticles produced by using ascorbic acid as the reductant in the absence of surfactant. 129
- Figure 6.16** Left: Activities of 0.2% $Ru@Al_2O_3$ and 0.1 % $Pt@Al_2O_3$ catalysts (in LA hydrogenation) prepared with N_2H_4 and AA as reductants respectively. Right: Activities of different loadings of Ru/Al_2O_3 in LA hydrogenation. The reaction was conducted at 70 °C and 1.3 bar. 130

List of Tables

Table 3.1	Example of an observation table to prepare a fish diagram where γ is varied at fixed $\alpha = 0.5$ and $\delta = 1$	50
Table 3.2	The compositions of microemulsions that are used in this work	51
Table 4.1	The composition of microemulsions used in the experiments	67
Table 4.2	Comparison of our TEM images and FFT of other results	76
Table 4.3	The comparison between different methods of Pt-nanoparticles preparation	81
Table 5.1	Activities of 0.1%-wt supported Pt catalysts prepared with different molar ratios of Pt to AA	99
Table 6.1	Zeta Potentials of the support materials and metal nanoparticles	118
Table 6.2	Effect of pre-calcination of the support on the yield of deposition and activity. Both supported Pt and Pd catalyst were prepared with ascorbic acid as the reductant.	125

Chapter 1

Introduction

The progressive development in industrial sectors constrains industries to improve their processes. Because many industrial processes are depending on catalysis, any progress in catalyst design can give significant benefits to society. Great efforts of researchers in industries and academic institutions have been made continually either in finding new strategies or in improving methods to upgrade catalyst performance. A new and improved catalyst can be a great advantage to industry for a competitive manufacturing cost and thus can be the key to industrial success.

In carrying out industrial catalyst research and development, nanotechnology has significant influence on the utilized tools. It can be said that catalysis is the largest application of nanotechnology because a major aspect of catalyst optimization is optimizing the usage of active precious nanomaterials.¹ Since the invention of the scanning tunneling microscope (STM) in 1981 and the discovery of the atomic force microscope (AFM) in 1986,² nanomaterial applications in various fields are developing rapidly. The technique of STM has revolutionised the understanding of surface chemistry, due to its ability to image at the atomic and molecular scale. Taking advantage of the development in nanotechnology, a wide range of nanoparticles synthesis have been developed. The control of surface structure and chemical reactivity at the nanometer length scale is paramount in catalysis research and engineering.

Metal nanoparticles are used as catalysts in many industrial reactions, from refining chemicals to producing polymers, pharmaceutical and biofuels. How well these metal nanoparticles perform as catalysts in the reactions depend on many aspects. In general,

catalyst performance is sensitive to particle size because the surface structure and electronic properties can change greatly in this size range. Particles ranging in size from roughly 1 to 50 nm exhibit physical and chemical properties that are intermediate between those of the smallest element such as a metal atom and those of the bulk material.³

Nanomaterials are more effective than conventional catalysts because their extremely small size yields an extremely large surface area-to-volume ratio and their properties are not found for their macroscopic counterparts. These two reasons account for the usefulness and effectiveness of nanocatalysts. Catalysts that have higher surface area-to-volume ratios provide more contact area between the substrate and their active site and thus accelerate the chemical reactions. Therefore, many experimental studies on nanocatalysts have focused on correlating catalytic activity with particle size. One strategy to control the particle size is by stopping the reaction at different growth stages. The matter about the particle size control is covered extensively in Chapter 2.

Controlling the shape of nanocrystals is the-state-of-the-art in nanomaterials research especially in catalysis field. During the last decade, researchers discovered that the catalyst performance is not only affected by the particle size but also by the particle shape. The effects of particle shapes on catalytic performance were first reported by Narayanan and El-Sayed.⁴⁻⁷ They found that the percentage of atoms that are located at corners and edges relative to the total surface atoms was highest for tetrahedral nanocrystals, followed by truncated octahedral and cubic nanocrystals, leading to a decrease in the catalytic activity of cubic shapes. However, their study was limited only to shapes bound by low-index planes $\{111\}$ and $\{100\}$.

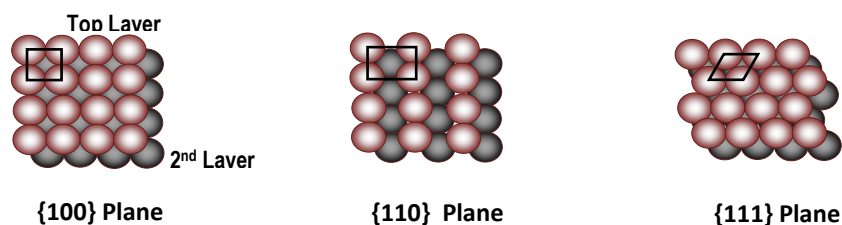


Figure 1.1 Face-centered cubic (fcc) metals with low index facets.

Fundamental studies on the single-crystal surfaces of bulk Pt have shown that high-index planes exhibit much higher catalytic activity than common, stable, low-index planes, such as $\{111\}$ and $\{100\}$.⁸ The reason is because high-index planes have a greater density of unsaturated atomic steps, ledges, and kinks which can serve as active sites for breaking chemical bonds. Thus, it is reasonable that an increase of high-index surfaces with rich corner and edge sites should be the criteria for selection of an excellent nanocatalyst. However, the common shapes of face-centered cubic (fcc) metals are enclosed by $\{111\}$ and $\{100\}$ facets and contain a low percentage of corner and edge sites.⁹ Therefore, controlling the growth of the metal catalyst has opened the possibility to optimize the geometry of the particles for enhanced activity.

In relation to the control of particle shape, it is important to recognize that the performance of nanocrystals used as catalysts depends strongly on the surface structure of the crystal facets. For a pure metal, the surface energy relies on coordination numbers of surface atoms as well as their density. Surface energy is defined as the surface excess free energy per unit area of a particular crystal facet.¹⁰ For a material with an isotropic surface energy such as an amorphous solid, total surface energy can be lowered simply by decreasing the amount of surface area corresponding to a given volume. As a result, the particle shape is a perfectly symmetric sphere.

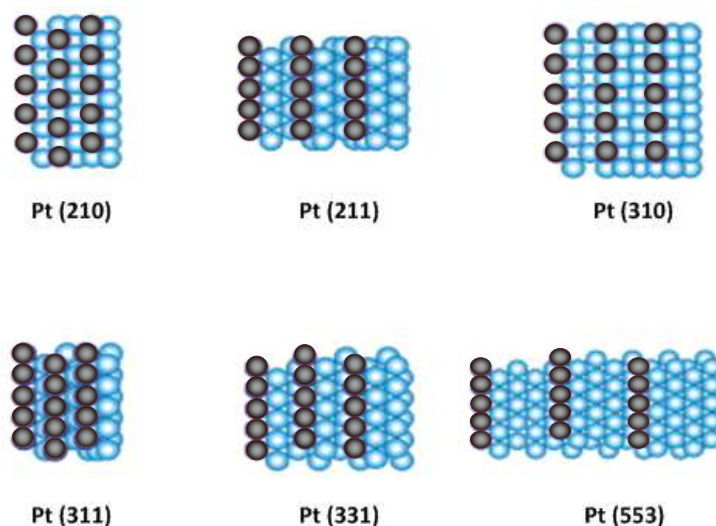


Figure 1.2 Face-centered cubic (fcc) metals with high index facets.

Noble metals adopt a face-centered cubic (fcc) lattice and possess different surface energies for different crystal planes. This anisotropy results in stable morphologies where free energy is minimized by particles bound by the low-index crystal planes that exhibit closest atomic packing.¹¹ The surface energy increases in the order of $\gamma_{\{111\}} < \gamma_{\{100\}} < \gamma_{\{110\}} < \gamma_{\{hkl\}}$ on a face-centered cubic (fcc) metal, where $\{hkl\}$ represents high-index planes with at least one Miller index larger than 1.¹² Generally, high-energy surfaces have an open surface structure and possess exceptional properties. Long term fundamental studies in surface science have shown that Pt high-index planes with open surface structure exhibit much higher reactivity than that of (111) or (100) low-index planes, because high-index planes have a large density of low-coordinated atoms situated on steps and kinks, with high reactivity required for high catalytic activity. Figure 1.3 shows an illustration of a crystal surface which has terrace, kink and step.¹³

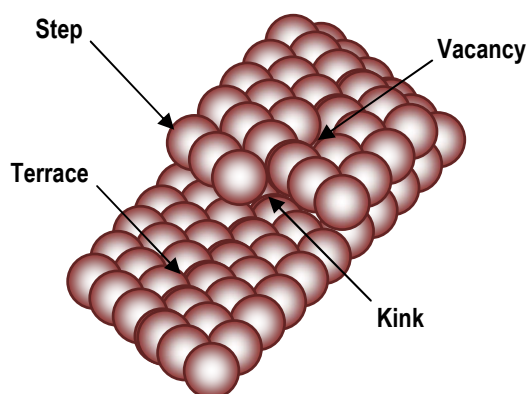


Figure 1.3 Illustration of terrace, kink and step in a crystal structure

On high-index planes, there exist steric sites that are considered as active sites and consist of the combination of several step and terrace atoms. Due to synergistic effect between step and terrace atoms, steric sites usually serve as catalytically active sites.^{14,15} Figure 1.4 depicts a model of surface atomic arrangement of fcc metal single-crystal such as Platinum to illustrate the coordinates of different crystal planes. Three vertexes of the triangle represent the three low-index planes i.e., (111), (100), and (110).

Among them, the (111) and (100) planes are atomic-scale flat with closely packed surface atoms, whereas the (110) plane is rough with step atoms. The coordination numbers of top layer atoms on (111), (100), and (110) are 9, 8, and 7, respectively. Other planes lying in the sidelines and locating inside the triangle are high-index planes. The three sidelines of the triangle represent $[\bar{0}11]$, $[\bar{1}10]$, and $[\bar{0}01]$ crystallographic zones, in which the planes exhibit terrace-step structure and are thus also called stepped surfaces. To illustrate the terrace-step structure straightforwardly, a microfacet notation is often introduced to denote the stepped surfaces.¹⁶

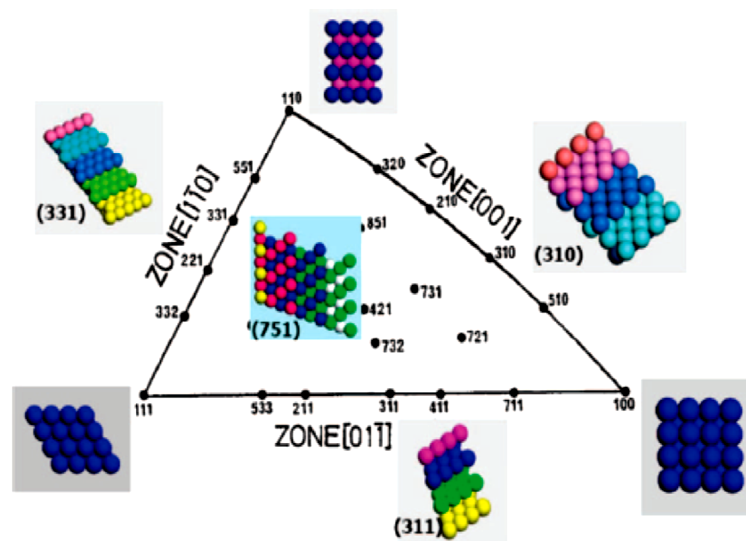


Figure 1.4 Unit stereographic triangle of fcc metal single-crystal and models of surface atomic arrangement (from ref 16).

Because most physical and chemical properties of metal nanoparticles depend on their size and shape, it is very important to develop synthetic routes that give non-agglomerated, uniform nanoparticles with a well-controlled size and shape with a narrow size distribution.¹⁷ The metal that is used to demonstrate a new synthesis method in this study (will be described later) is Platinum. Pt nanocrystals are widely used and are indispensable catalysts due to their excellent activity and stability.¹⁴ Because of their unique properties, Platinum clusters are of special interest and are the subject of intense study.¹⁸ As Pt is particularly expensive, there is a real incentive to reduce the amount of Pt required in processes. To this goal, much research has been devoted to size reduction of Pt catalysts so to maximize the surface area.¹⁹

Generally, nanoparticles in solution have a strong tendency to form into spherical or near spherical polyhedral structures to minimize the total surface energy. Platinum adopts the highly symmetrical face-centred-cubic (fcc) crystal structure. The predicted thermodynamic equilibrium shape for an fcc nanocrystal is a truncated octahedron bound by six $\{100\}$ and eight $\{111\}$ planes.²⁰ Therefore, to synthesize metal nanocrystals with unspherical or near-spherical polyhedral forms and also with high index facets is a challenging work.

There are some factors that can control the shape of nanoparticles during the synthesis process such as surfactant, variation of reaction temperature, introduction of seeds or foreign species, and reducing agent.²⁰ This phenomenon will be described in more detail in Chapter II. In this work, the reducing agent is chosen to be the shape controlling factor instead of the surfactant to keep the phase behavior of the microemulsion (because changing the type of surfactant results in changes of the phase behavior of microemulsions). Shape controlled synthesis of Pt nanocrystals with high-index facets offers a good approach for creating Pt nanocatalyst materials with much higher activities than currently available with commercial Pt catalyst.¹⁴

Despite of many researchers having successfully produced Pt particles of small size with different shapes, they still remain in the colloidal state which can only be stable for a limited time. The catalytic activity may quickly decay due to the growth of nanoparticles as the result of particle sintering during reactions, undergo aggregation and suffer from poisoning under the reactions conditions, resulting in deactivation and loss of catalytic activity.²¹ In addition, the organic ligands or inorganic capping materials which are used to stabilize the nanoparticles during their initial synthesis (core-shell-type particle as well as colloids and soluble polymers), may block the access of the target molecules to the catalyst surface and therefore severely reduce the catalytic activity.

To create more stable catalysts, nanoparticles need to be deposited on support materials. In general, it is difficult to preserve the size and shape of nanoparticles and to control the dispersion during the deposition process. This is a major challenge when

preparing supported catalysts by deposition. The increasing metal dispersion and decreasing metal particle size generally results in increasing catalyst activities.

This thesis provides a comprehensive presentation about a new method of synthesis active and stable supported metal nanoparticles, namely thermo-destabilization of microemulsions. The detail features of this method are described in Chapter IV and V which present the published papers of this work. In principle, this method comprises two main steps. The first is designing the size and the shape of metal nanoparticles via microemulsions and the second is dispersing the prepared nanoparticles on the support material. In preparing the catalyst nanoparticles, the core of the micelles is considered as a nanoreactor. The size of nanoparticles is controlled by some parameters such as an appropriate choice of the water-to-surfactant molar ratio and the concentration of salts inside of the water pools. In order to gain a low cost process, we determine the surfactant concentration (γ) and oil concentration (α) that can produce nanoparticles at room temperature. Although many parameters can be involved in the synthesis process, there are some important parameters which are dominantly influence the size and the shape, as described in Chapter IV and V. The nanoparticles are transferred onto the supports by destabilizing the microemulsions with temperature change. The deposition process is optimized in order to well-disperse the nanoparticles on the support materials without agglomeration.

The first goal of this study is to find the strategies to prepare an active and stable Pt catalyst using thermo-destabilization of microemulsion. The initial approach to obtain the active catalyst was decreasing the catalyst particles size (less than 5 nm). Many parameters were involved to reach this goal such as finding the microemulsion composition that can produce small Pt particles at room temperature (for energy saving), support material which can well adsorb the particles, calcinations temperature which can hinder sintering effect, etc. After having found the strategy to produce high surface area and stable catalysts (in the first goal), the next step was to find a strategy to produce particle shapes with higher index facets. So, the second goal is to increase the catalyst activity by making the particle shape more irregular which provides high-index planes. To analyze the sizes and morphologies of Pt nanoparticles, a transmission electron microscope is used to image the Pt nanoparticles on these carbon-film-coated copper grids.

This thesis is divided into seven parts. Chapter I presents a general overview about the research work including the background and aim. The explanation about the growth mechanism of Platinum will be described extensively in Chapter II. It is interesting that the assumption generally made about the specific mechanism through which platinum nucleate and start growing is the following: The Pt-(II) or Pt(IV) complexes first react with the reducing agent to give isolated Pt(0) atoms. After a while, when a critical concentration of Pt(0) atoms is reached, metal clusters start forming at an appreciable rate^{22,23} by aggregation of these atoms. However, Ciacchi et al. claim that no direct evidence of the isolated Pt(0) atoms has ever been presented. The presence of Pt(0) atoms is generally assumed from the kinetics of the whole reduction process.¹⁸ They suggest that the formation of metal-metal bonds between complexes in oxidation states higher than zero is a key step in the nucleation mechanism of colloidal particles upon reduction of platinum salt. Chapter II comprises also the fundamental theory of nanoparticles synthesis with microemulsions and its recent development together with the account of important factors that influence the properties of metal catalyst.

The general experimental part is explained comprehensively in Chapter III. Substantially, the main part of this thesis can be found in Chapter IV and V. The published paper in those chapters comprises the important results and discussions. Chapter VI composes significant additional results that can support the main part of this work. It addresses the synthesis of other metal supported catalysts such as Ag, Pd and Ru nanoparticles including their performance and characterization thus elucidating the synthesis method that is used in this work. The last part, Chapter VII, comprises a compact discussion and conclusion concerning all the results including the supporting results described in Chapter VI.

References

1. R. Schlögl and S. B. Abd Hamid, *Angewandte Chemie International Edition*, 2004, **43**, 1628–1637.
2. Berger, Michael, in *Nano-Society: Pushing the Boundaries of Technology*, 2009.
3. A. T. Bell, *Science*, 2003, **299**, 1688–1691.

4. R. Narayanan and M. A. El-Sayed, *Journal of the American Chemical Society*, 2004, **126**, 7194–7195.
5. R. Narayanan and M. A. El-Sayed, *Nano Letters*, 2004, **4**, 1343–1348.
6. R. Narayanan and M. A. El-Sayed, *J. Phys. Chem. B*, 2005, **109**, 12663–12676.
7. R. Narayanan and M. A. El-Sayed, *The Journal of Physical Chemistry B*, 2004, **108**, 5726–5733.
8. G. A. Somorjai and D. W. Blakely, , *Published online: 18 December 1975*; | *doi:10.1038/258580a0*, 1975, **258**, 580–583.
9. Y. Xiong, B. J. Wiley, and Y. Xia, *Angewandte Chemie International Edition*, 2007, **46**, 7157–7159.
10. J. Kollár, L. Vitos, B. Johansson, and H. I. Skriver, *physica status solidi (b)*, 2000, **217**, 405–418.
11. A. R. Tao, S. Habas, and P. Yang, *Small*, 2008, **4**, 310–325.
12. Z. L. Wang, *J. Phys. Chem. B*, 2000, **104**, 1153–1175.
13. G. A. Somorjai and Y. Li, *Introduction to Surface Chemistry and Catalysis*, John Wiley & Sons, 2010.
14. Z.-Y. Zhou, N. Tian, J.-T. Li, I. Broadwell, and S.-G. Sun, *Chemical Society Reviews*, 2011, **40**, 4167.
15. N. P. Lebedeva, M. T. M. Koper, J. M. Feliu, and R. A. van Santen, *J. Phys. Chem. B*, 2002, **106**, 12938–12947.
16. Z.-Y. Zhou, N. Tian, Z.-Z. Huang, D.-J. Chen, and S.-G. Sun, *Faraday Discussions*, 2009, **140**, 81.
17. E. G. Castro, R. V. Salvatierra, W. H. Schreiner, M. M. Oliveira, and A. J. G. Zarbin, *Chemistry of Materials*, 2010, **22**, 360–370.
18. Ciacchi, L.C, Pompe, W, and De Vita, A, *J. Am. Chem. Soc.*, 2001, **123**, 7371–7380.
19. Y. Xia, Y. Xiong, B. Lim, and S. E. Skrabalak, *Angew. Chem. Int. Ed. Engl*, 2009, **48**, 60–103.
20. S. Cheong, J. D. Watt, and R. D. Tilley, *Nanoscale*, 2010, **2**, 2045.
21. J. M. Campelo, D. Luna, R. Luque, J. M. Marinas, and A. A. Romero, *ChemSusChem*, 2009, **2**, 18–45.
22. D. G. Duff, P. P. Edwards, and B. F. G. Johnson, *J. Phys. Chem.*, 1995, **99**, 15934–15944.
23. Y. Mizukoshi, R. Oshima, Y. Maeda, and Y. Nagata, *Langmuir*, 1999, **15**, 2733–2737.

Chapter 2

Design and synthesis of supported metal catalyst

Interest in synthesis of metal nanoparticles has been growing progressively due to the distinctive position of nanomaterials which is between atoms and bulk solids as well as their novel properties. The novel properties of a metal nanocrystal are strongly determined by their physical parameters include size, shape, composition, and structure. In principle, one can design the properties of a metal nanoparticle by controlling any one of those parameters. For the application in catalysis field, properly designed of nanoparticle as a catalyst (nanocatalyst) should have a good impact to the essential attributes such as the activity, stability and selectivity. Therefore, it is crucial to understand the fundamental subject in the preparation method of the nanocatalyst.

Many preparation methods of nanocatalyst have been developed through the liquid phase route. The classical chemical synthesis methods are co-precipitation, impregnation and deposition-precipitation. Some other novel greener routes include precipitation from water-in-oil emulsions, photochemistry, chemical vapor deposition and electrochemical reduction.

The following sub-chapter will describe the synthesis method that is used in this work i.e. water-in-oil droplet microemulsion particularly the mechanism of nanoparticle formation that takes place during the synthesis process.

2.1 Synthesis of metal nanoparticles via water-in-oil droplet microemulsion

Microemulsions are colloidal nano-dispersions of water-in-oil droplets or oil-in-water droplets stabilized by surfactant. These thermodynamically stable dispersions can be considered as real nanoreactors which can be used to perform chemical reactions to synthesize nanomaterials. In principle, different reactants (metal precursor and reductant) solubilized in separate microemulsion solutions are allowed to react upon mixing. Through the microemulsion method, new and particular properties of nanomaterials can be designed by appropriate control of the synthesis parameters. Therefore the microemulsion method is a very flexible technique which allows the preparation of a great variety of nanomaterials, just alone or in combination with other techniques. However, the precise control of all the parameters which can be varied affecting the final particle sizes and shapes is still remaining a challenge.¹

2.1.1 Mechanism of nanocrystals formation

The development of synthetic routes to produce nanocrystals with controlled size, size distribution and shape is directly correlated with the ability to control the nucleation and growth process.^{2,3} In a typical synthesis of metal nanocrystals, a precursor compound is either decomposed or reduced to generate zero-valent atoms, the building blocks of a metal nanocrystal. Depending on the explicit route to atoms, the nucleation process might take completely different pathways.

In the early 50's, LaMer and coworkers proposed a mechanism of nucleation and growth for the decomposition route (Figure 2.1).⁴ The mechanism is based upon an extensive study of the solution-phase synthesis of monodisperse sulfur colloids. In the context of metal nanocrystal synthesis, the concentration of metal atoms steadily increases with time as the precursor is decomposed. Once the concentration of atoms reaches a point of supersaturation, the atoms start to aggregate into small clusters such as nuclei in homogeneous or heterogeneous nucleation. Once these nuclei are formed, they will grow very fast causing the concentration of metal atoms to drop. If the concentration of atoms drops quickly below the level of minimum supersaturation, no additional nucleation events will occur. With a continuous supply of atoms via ongoing precursor decomposition, the nuclei will grow into nanocrystals of increasing size until

an equilibrium state is reached between the atoms on the surface of the nanocrystal and the atoms in the solution. Besides growth via atomic addition, the nuclei and nanocrystals can directly merge into larger objects via agglomeration.⁶

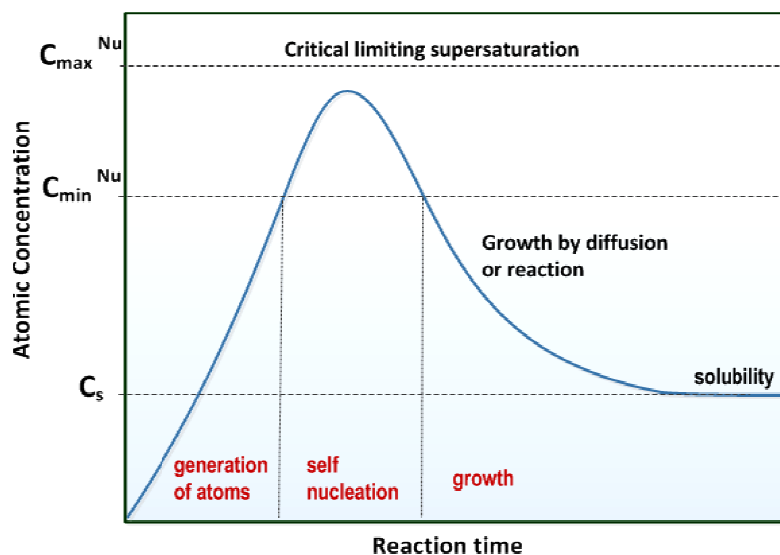


Figure 2.1 Plot of atomic concentration against time according to La Mer model for the generation of atoms, nucleation, and subsequent growth of colloidal synthesis.

2.1.2 Mechanism of particles formation in microemulsions

In general, the mechanism of nanoparticle formation occurs in three different steps i.e. nucleation, growth by autocatalysis, and growth by ripening.⁶ In microemulsions system, these steps take place inside the droplets. Having more theories and experiments, a number of scientists proposed some other growth mechanisms of nanocrystals. Based on some literatures,^{3,6,7} the mechanism can be divided into two parts, i.e. a reversible and an irreversible part, as illustrated in Figure 2.2. The process that happens in the reversible part is random collisions and intermolecular forces which cause molecules to form and break apart. According to the theory of classical nucleation, particle formation is an endothermic process in which molecules that collide and stick together tend to fall apart. The key is to cause enough collisions to occur that a pair is formed.⁹ In the irreversible part, cluster grows indefinitely by condensation

and coagulation until it becomes a particle. In the following a detailed description of this mechanism will be provided.

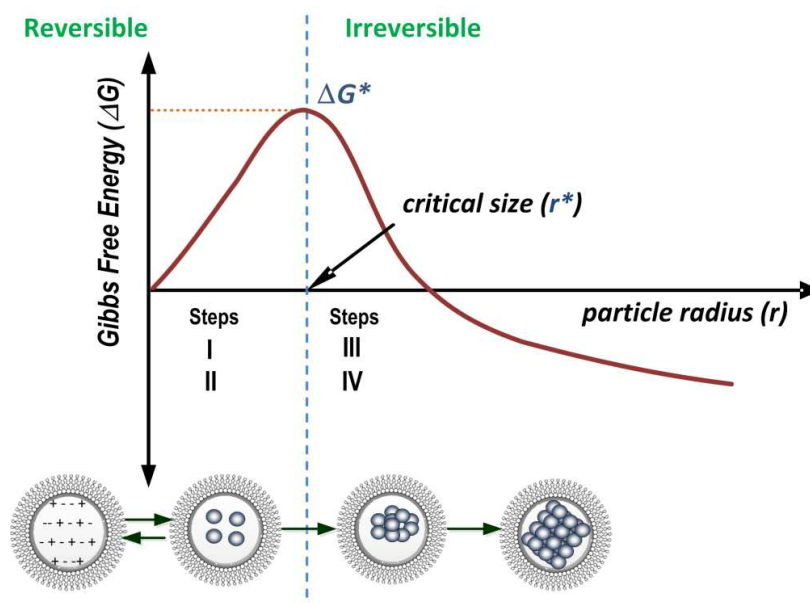


Figure 2.2 Schematic diagram of the nucleation and growth process showing the dependence of the Gibbs free energy (ΔG) on the crystal size. Reversible process takes place below a critical radius (r^*) and turn to irreversible when $r > r^*$. (Modified from Dalmazchio et.al³)

Step I and II

Nucleation is the birth of a new phase which represents the very first stage of any nanocrystal synthesis. It is the process by which atoms (or ions), which are free in solution, interact together to produce a thermodynamically stable cluster of metal. Because the surface molecules are not well bound to their neighbors, their contribution to the free energy of the new phase is greater. At very small size, the nucleus is unstable. Adding one more molecule just increases the free energy of the system. On average, such a nucleus will dissolve rather than grow. But once the nucleus gets large enough, the drop in free energy associated with formation of the bulk phase becomes sufficiently high that the surface free energy is unimportant, and every addition of a molecule to the lattice lowers the free energy of the system. There is an intermediate

size at which the free energy of the system is decreased whether the nucleus grows or dissolves, and this is known as the critical size. This phenomenon is referred to as the Gibbs-Thomson effect. Once the critical size is exceeded, the cluster becomes a supercritical nucleus capable of further growth. If the nucleus is smaller than the critical size, spontaneous dissolution can occur.⁹ Therefore, steps I and II are reversible. This meta-stability is the important feature of nucleation, i.e. the transformation from original to new phase has to overcome a free energy barrier as depicted in Figure 2.2. In another words, the free energy of cluster formation, ΔG , increases with cluster size, reaching a maximal value at the critical size, $r = r^*$, and decreases after the critical size.

Step III

When the cluster grows to a critical size, the process becomes irreversible (thermodynamics condition). Crystal size and shape can be controlled with the aid of stabilizers. To a first approximation, the shape of the crystal is controlled by energetic arguments (this is a thermodynamic condition). In fact, the cluster will grow in a geometric arrangement in order to minimize the surface energy. In this step, in the case of metal nanoparticle synthesis, the reductant and/or surfactant play an important role to control the size and the shape of the nanocrystal. This process takes place in a kinetic condition. Slow process of metal reduction and the preferential adsorption/desorption of the surfactant can result in an anisotropic crystal.^{10,2,11}

Step IV

This consists of the interaction of the nanocrystals formed in step IV to produce larger structures. This nanocrystal-based self-assembly process is governed by particle–particle and particle–solvent interactions. In this step, the formation of agglomerate (disordered assembly) of nanocrystals or even the formation of mesocrystals (mesoscopically structured crystals) may occur.¹³

One of the difficulties in managing good control of the synthesis of colloidal nanocrystals is to split between the nucleation stage and the growth process. Therefore, designing the nanocrystals is not a simple task, because it requires control over the chemical composition and the purity, size, size distribution and shape of the crystallographic phase, as well as the chemical functionality of the nanocrystal surface.²

As earlier mentioned, the water droplets (microemulsion droplets) in these systems can be considered as “nanoreactors”, providing a suitable environment for controlled nucleation and growth. Due to their small size (in the 1-10 nm range), these droplets are subject to Brownian motion, therefore they are very dynamic. As a result, they collide continually, sometimes coalescing to form short-lived dimers, and interchange contents then break apart and redisperse again to form new micelles. Obviously, any inorganic reagents encapsulated inside the water droplets will become mixed. At the latter stages of growth, steric stabilisation provided by the surfactant layer prevents the nanoparticles from aggregating.⁶

The fundamental of the nanoparticles synthesis in this method is the exchange process of the content inside the water droplets through collisions. According to Tojo et.al^{9,6}, as previously described in stage I to IV, there are two interchange criteria:

a. The interchange of reactants in absence of nuclei.

In this stage, two possible situations may happen. First, if both droplets carry the same reactant, one atom from the droplet containing a higher number of reactants will go to the droplet containing a lower number of reactants (concentration gradient). The second is that when the two droplets carry different reactants, the chemical reaction gives rise to the formation of the nuclei ($A + B \rightarrow P$). Assuming again a concentration gradient, this first nucleus will be located inside the droplet carrying a lower number of reactants.

b. The interchange of reactants in the presence of nuclei

In this case, autocatalysis process will take place because the existing nuclei will act like a catalyst. If only one of the two droplets carry a nucleus, the reaction will be performed in the droplet containing the nucleus. If both water pools carry them, the reaction will be performed in the droplet containing the bigger nucleus. As the nuclei grow, the interchange becomes more difficult because it depends on the flexibility of the surfactant film. A highly flexible surfactant film will allow the interchange of larger nuclei than a rigid surfactant film.

As a general principle, the parameters that influence the size and the shape of the final particles inside of the droplets are the following.

- a. Surfactant film flexibility. As previously mentioned, the flexibility of the surfactant film around the droplets influences the reactant interchange among the

nanodroplets. The elasticity of the film depends not only on the surfactant type and the thermodynamic conditions, but also on the presence of additives, like alcohols, electrolytes, block copolymers and polyelectrolites. The interdroplet exchange of the particles growing inside the droplets is inhibited by the inversion of the film curvature in the fused dimer (see Figure 2.3) which, in turns, depends on the film flexibility.¹³

- b. Droplet size, which is greatly dependent on the water-surfactant molar ratio. The size of the droplet is expected to be proportional to the water-surfactant molar ratio. It was experimentally observed,^{6,14} the final size of the particles maybe slightly bigger or smaller than the droplet size, depending on the flexibility of the surfactant film and/or the surfactant adsorption.
- c. Adsorption of surfactants onto the particles. The surfactant adsorption can stop the growth of the particles inside the microemulsion droplets. The particle control by surfactant adsorption can easily be detected by the fact that the particle size is almost constant and independent of the various parameters discussed above which may affect the particle size. Because the adsorption on catalysts is favored this size control by adsorption has been mostly found in the preparation of catalysts particles in microemulsions.

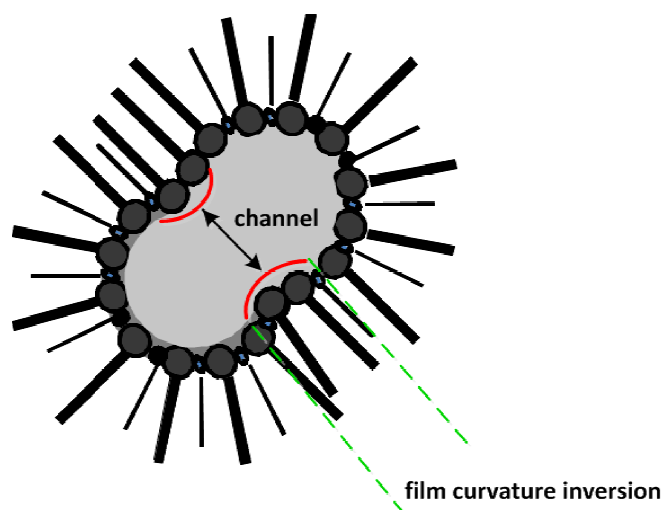


Figure 2.3 Schematic representation of a fused dimer after a two droplets collision showing the channel opened in between. (Modified from the ref. 12)

In general, the exchange of nuclei or particles between the droplets is not favored energetically, because it would produce the formation of a big hole during the collision of the droplets and cause a large change in the curvature of the surfactant layer around the droplets. Because the inorganic salts have very low solubility in the oil phase, the dynamic exchange of reactants between the droplets through the continuous phase is unfavorable. When the particles attain their final size, the surfactant molecules attach themselves to the surface of the particles and stabilize them. Further growth is also prevented by the adsorbed surfactant layer

2.2 Size and shape control of metal nanoparticles

As mentioned above, the synthesis of nanoparticles inside of the water droplets microemulsion involves a nucleation followed by growth stages in which solutes are consumed. The final shape of nanoparticle can be controlled by tuning the shape of nuclei and directing the growth of the nuclei and/or nanocrystals. Nuclei shape has a strong effect on the final nanocrystal shape. It is determined by the chemical potentials of the different crystallographic faces, which are in turn highly dependent on the reaction environment such as temperature and solute concentration.¹⁵ Not only does the formation of nuclei strongly govern the final morphology of the nanoparticles, the subsequent growth stages do also. In general, nanoparticle growth takes place under two different regimes, either in a thermodynamically controlled or kinetically controlled growth regime^{16,17} The schematic illustration of these two shape controls¹⁰ is depicted in Figure 2.4.

Thermodynamic growth is characterized by a sufficient supply of thermal energy and low flux of monomers.¹¹ This often results in uniform growth of all crystal faces which turns to formation of spherical or near-spherical structures. On the contrary, favored and directional growth occurs under the non-equilibrium kinetic growth regime. Therefore, manipulation between the thermodynamic and the kinetic growth regimes is a critical factor in determining nanoparticle shape.¹⁸

In kinetic growth control, preferential adsorption of surfactant to specific facets can hinder or enhance the crystal growth in some directions, thus physically directs the anisotropic growth.¹⁹ The energetic aspects can also play an important role in determining the anisotropic growth of nanoparticles. The formation of anisotropic

structures is a direct consequence of the energetics being dominated by surface energy in nanometer regime. Anisotropic nanoparticles have higher surface to volume ratios than spheres and, consequently, higher energy per atom, even though they can expose facets with lower surface energies (for example 111 facet index in face-centered cubic, *fcc*).²⁰

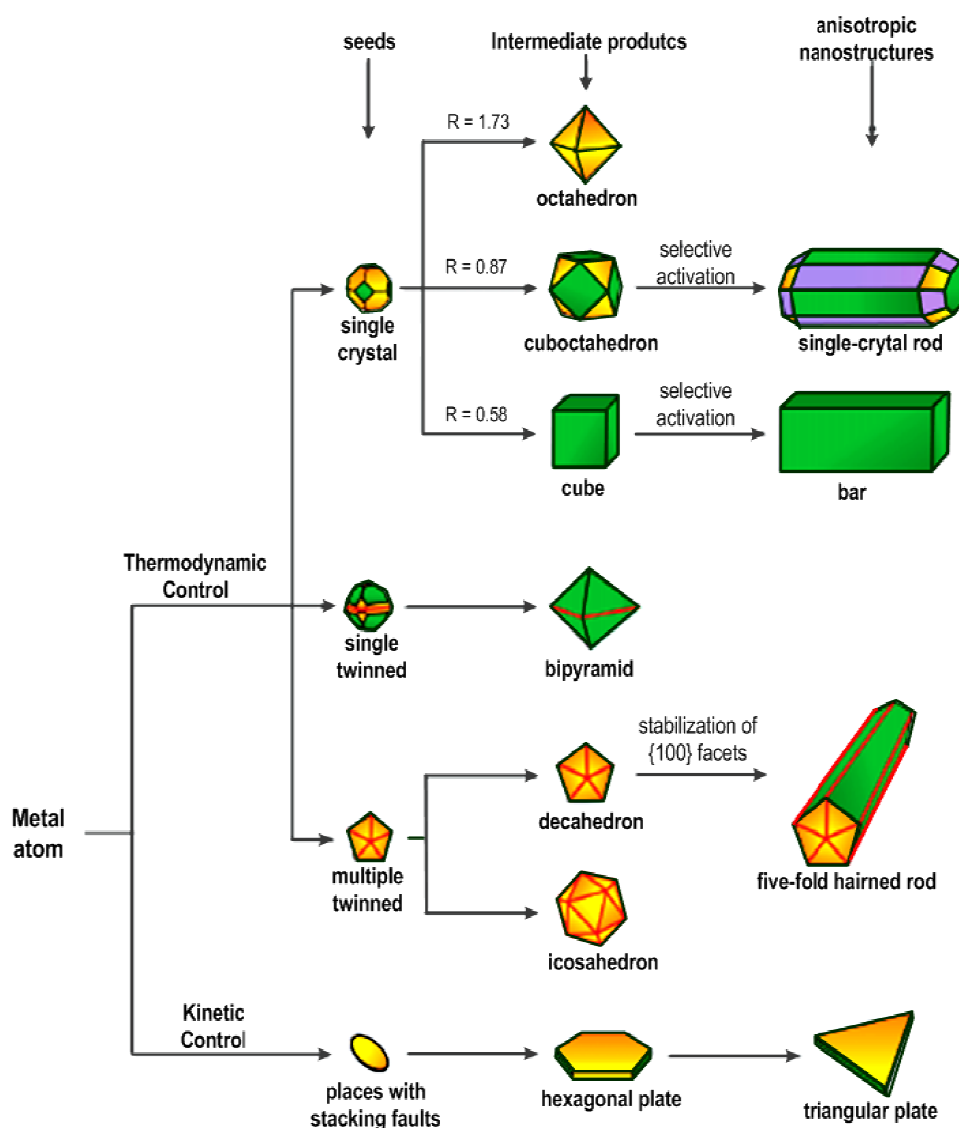


Figure 2.4 A schematic illustration of the reaction pathways that lead to metal nanostructures with different shapes. The green, orange, and purple colors represent the {100}, {111}, and {110} facets, respectively. The parameter R is defined as the ratio between the growth rates along the $\langle 100 \rangle$ and $\langle 111 \rangle$ axes. (Modified from ref. 8)

The energy with which surfactant molecules present in the growth medium adhere to the surfaces of growing nanocrystals is one of the most important parameters influencing crystal growth. The surfactant needs to be able to exchange on and off the growing crystals, so that regions of the nanocrystal surface are transiently accessible for growth, yet entire crystals are, on average, monolayer-protected to block aggregation.²

2.2.1 Thermodynamic Control

2.2.1.1 Thermodynamic Size Control

In the nanocrystal formation under thermodynamic control, the greatest amount of the most stable product will be produced. The most stable product can be predicted through the formation of single-crystal seeds based on the Wulff's theorem, which endeavors to minimize the total interfacial free energy of a system in a given volume (the interfacial free energy can be defined as the free energy required for creating a unit area of "new" surface).²¹ Another attempt to achieve a stable product is by thermodynamical stabilization with the surfactant molecule.

The size of nanocrystal can be thermodynamically controlled in microemulsion systems. Whetten and Gelbart²² assumed that in microemulsion systems, all clusters are in thermodynamic equilibrium with one another. They also suggest that the single-sized nanocrystals also represent self-assembled structures at thermodynamic equilibrium. Leff et al. reported that the size of gold nanocrystals can be thermodynamically controlled by simply varying the gold-to-thiol (stabilizer) ratio.²³ They found that nanocrystal with specific sizes can be obtained as equilibrium products of a room temperature system.²³ The role of long chain thiols in stabilizing nanocrystal thermodynamically has been argued to be analogous to that of surfactant in the more familiar case of water-in-oil microemulsions. The capping agent is used to both control the rate of particle growth and impart useful chemical behavior (solubility, for example) to the final nanocrystal product. It does not, in general, play a role in determining the final particle size and shape distributions.

2.2.1.2 Thermodynamic shape control

In nanoparticle synthesis with microemulsions, surfactant as stabilizing molecules adsorb onto and desorb from the surface of the growing nanocrystal in a dynamic way.² Depending on the type of surfactant, the adsorption and desorption rates could be different on different crystallographic facets and thus affects nanocrystal growth. El-Sayed et al. are the first to demonstrate the effect of stabilizer on the shape control of single-crystal platinum nanoparticles.^{24,25} They found that tetrahedral nanocrystals are formed under high stabilizer concentration, which facilitated a stronger adsorption onto the $\{111\}$ facets. Consequently, this reduced effectively the surface energy and the growth rate of these faces, leading to the formation of $\{111\}$ tetrahedra. From theoretical considerations, clusters with $\{111\}$ faces such as tetrahedral nanoparticles should be the most stable.²⁶ Other groups later also reported for the formation of platinum nanocubes enclosed by $\{100\}$ facets, which were preferentially stabilised by the chosen stabilisers.^{27,28} In these cases, because nanocrystals being terminated by the stabilised or thermodynamically favoured facets growth, it is considered to be thermodynamically controlled. Watt et al. also reported that the shape of nanocrystals can be thermodynamically controlled in a three-step growth process with using the organic stabilizer.

2.2.2 Kinetic control

2.2.2.1 Kinetic size control

Producing nanocrystals with a narrow size distribution is also important for catalyst preparation methods. Especially in the case of structure sensitive catalytic reactions, certain size and morphology for the metal particles on the catalyst surface are necessary for an optimum reaction condition. If a narrow size distribution could be produced, the less effective particles will be excluded and the metal used will be more efficiently. Thus, generally a narrow particle size distribution leads to a better catalytic activity. The dependence of the growth rate on the size of nanocrystal radius is illustrated in Figure 2.5. The left-hand side of the curve shows that very small crystals are unstable because of their large fraction of active surface atoms, as indicated by the negative growth rate. The right-hand side of the curve demonstrates that larger crystals with smaller surface-to-volume ratio are stable and grow. The zero-crossing points to the critical size, where nanocrystals neither grow nor shrink. As mentioned

above, the critical size depends on the monomer concentration with low monomer concentration favoring a larger critical size. The peak in growth rate versus size on the right-hand side arises because increasing the size of large crystals requires the blending of many more atoms than increasing the size of smaller crystals.

Therefore, the growth process of nanocrystals can occur in two different modes i.e. 'focusing' and 'defocusing', depending upon the concentration of the monomer. At a high monomer concentration, the critical size is small and therefore all the particles grow. In this condition, smaller particles grow faster than the larger ones. As a result, the size distribution can be nearly monodisperse. If the monomer concentration is below a critical threshold, small nanocrystals are depleted as larger ones grow and the size distribution broadens. The preparation of nearly monodisperse spherical particles can be achieved by interrupting the reaction while it is still in the regime where a large concentration of monomer is present.

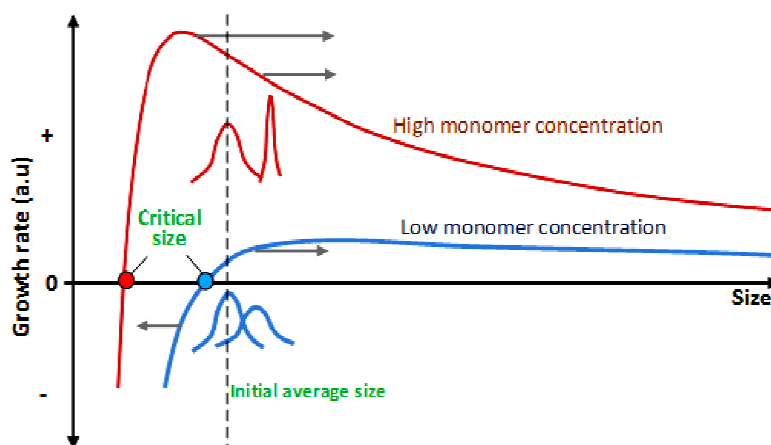


Figure 2.5 Size distribution focusing (a.u., arbitrary units). The growth of nanocrystals can be 'focusing' and 'defocusing', depending upon the concentration of the monomer present.

This can explain why a slow growth rate, which produces equilibrated and nearly round crystals, yields very broad size distributions. The slow growth is related to low monomer concentrations and it is most probably that the critical size falls within the resultant size distribution of nanocrystal. Size focusing is optimal if the monomer concentration is kept such that the average nanocrystal size present is always slightly larger than the critical size. ²

In principle, it is preferable for nucleation to be separated from the growth step to obtain relatively monodisperse samples. This means that nucleation must take place on a short time scale. This can be achieved by rapidly injecting suitable precursors into the solvent to generate transient supersaturation of monomers and induce a nucleation burst. A rapid and intense nucleation burst will lower the monomer concentration below the nucleation threshold, so monomers remaining of solution will only add to the existing nuclei. In many cases, there is some overlap between the nucleation and growth time scales, so the resultant dispersion in nanocrystal sizes needs to be compensated for with focusing. But in optimal cases, it is possible to remain in the fast growth-focusing regime while remaining below the nucleation limit.

2.2.2.2 Kinetic shape control

In practice, kinetic considerations are also critical in determining nanocrystal morphology. This is particularly understandable in colloidal synthesis, where parameters such as reaction time, surfactant and reactant concentration profoundly affect nucleation and growth. Xia et al. are the first to demonstrate the kinetically controlled growth of single-crystalline nanocubes bound by $\{100\}$ crystal facets.²⁹ They found that by regulating the rate of the reducing process, the nucleation events during the reaction can be controlled. Watt et al. have also demonstrated that adding oleic acid to the system leads to the increase in the rate of adatom (an atom that lies on a crystal surface) addition thus allowing fast crystallographically directional growth under a kinetically controlled growth regime.³⁰ The resulting kinetically driven, much faster growth that followed was shown to be entirely random and no crystallographically orientated, which then led to the formation of highly branched palladium nanostructures.¹⁸

In controlling the particle shape, the formation of highly anisotropic shapes is desirable because they have larger surface areas, which renders them metastable and high surface energy forms. Formation of the metastable nanocrystals therefore requires a kinetic growth regime, whereas equilibrium nanocrystals with low aspect ratios are obtained in the slow growth limit under thermodynamic control. At low growth rate, nearly round nanocrystals are formed, with broad size distribution. At higher growth rate, narrow size distribution (focusing regime) is observed. When the growth rate is increased just beyond the focusing regime, a surprising diversity of highly anisotropic shapes are obtained, from simple rods and disks until shapes like arrows and tetrapods.

The equilibrium shape of inorganic nanocrystals, although faceted, they have a low surface energy. The growth rate of a crystal facet depends exponentially on the surface energy, so that at high growth rates, in a kinetically controlled growth regime, high-energy facets grow more quickly than low-energy facets. The kinetic shape control can be widely adjusted using selective adhesion (Figure 2.6) According to the concept of dynamic solvation, organic surfactants exchange on the nanocrystal's surface during growth. In a faceted crystal, however, the exchange rate on the different facets is not necessarily to be the same. The introduction of an organic compound that selectively adheres to a particular crystal facet can be used to effectively lower the energy and slow the growth rate of that facet relative to other. Selective adhesion effects have not been observed directly during nanocrystal growth, but theoretical studies provide a reliability to the concept.³¹ A possible alternative mechanism involves complexation of the reactive monomer species in solution by organic molecules. This leads to an environment with high chemical potential, and it can be used to adjust growth rates.³²

In the kinetic growth regime, it is possible to create sequence events that produce more complicated shapes. A first instance is the outstanding phenomenon of sequential elimination of a high-energy facet.³³ Fast-growing facets will finally disappear during growth process, resulting in a crystal that is terminated by slower-growing facets. An interesting point is when that the relative growth rates of two different low-index facets differ greatly. In this case, the higher-energy facet will grow so rapidly that a second or even third layer of atoms can start to form before a first layer is complete. Another possibility is that when another facet which has intermediate energy, between the low and high energy ones, present initially. In this case, that facet may form transiently during the growth of the high-energy facet. Once such a facet forms, it will continue replacing the initial high-energy facet. This new intermediate-energy facet will still grow more quickly than the initial slow-growing one, so that the shape will develop in a complex pattern during the growth process. This phenomenon has been used to form arrow-shaped nanocrystals of CdSe³³ and zigzag-shaped crystals of TiO₂.³⁴

Another approach to produce the complex shapes nanocrystals is oriented attachment.³⁵ This remarkable process that was first described by Penn et al.³⁶ involves the coalescence of faceted nanocrystals in such a way that it eliminates two high-energy facets. The detailed mechanism of this oriented attachment remains unclear, but it seems to occur in many process syntheses of materials systems. The most frequent

shapes produced with oriented attachment mechanism are rods and wires. The extent and nature of the oriented attachment process can also be manipulated with surfactant control. In fact, the specific chemical transformation of the surfactant on high-energy facets may play a crucial role in some of the synthesis strategies.³⁷

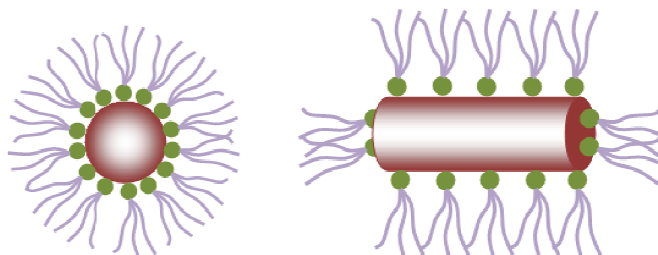


Figure 2.6 Illustration of the kinetic shape control by selective adhesion of surfactant.

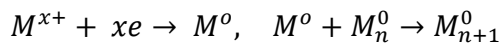
The general procedure for solution-phase synthesis of metal nanoparticles involves the reduction of a metal precursor in the presence of a surfactant or stabilizer. By varying the type and concentration of the metal precursor, the reducing agent and stabilizer, as well as reaction conditions such as temperature and time, a myriad of variables are possible.

2.3 Growth mechanism in metal reduction

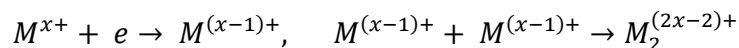
The initial nucleation is a central step to the following growth process and the final shape of the nanocrystal under the given conditions. However, it is rather difficult to structurally determine and further control the newly formed tiny clusters. Because it is generally assumed that metal ions exist as monomeric units through complexation with anions, ligands, or solvent molecules, a reductant may provide possible access to control nucleation kinetics. It has been reported that the reduction process can be manipulated to produce various shape of nanocrystal by employing reductants with different reducing power.^{38,39}

In the metal reduction process, the metal precursor is in a higher oxidation state than the atomic species. The mechanism that is generally reported is that the metal

precursor is reduced first into zero-valent atoms, which aggregate into nuclei and then grow into nanocrystals as expressed by the following equation:



The other path is the formation of a cluster consisting of unreduced metal ions prior to full reduction to the metallic state.⁴⁰⁻⁴²



In the kinetic control mechanism of the particle formation, especially in the case of strong reducing agents, it has been indicated that the nucleation starts from the full reduction of precursor ions and then the metal clusters are formed.⁴³ Interestingly, reducing PtCl_4^{2-} with a moderate reductant, Henglein et al.⁴⁰ have excluded the presence of Pt^0 atoms but postulated the monovalent Pt dimer as the first reaction intermediates. In other words, under moderate reduction conditions, some kind of Pt complex clusters can be formed in the initial nucleation stage prior to the complete reduction of the Pt ions to zero valent Pt atoms.

The molecular mechanism of cluster growth upon the reduction of hydrolyzed PtCl_4^{2-} ions is studied in a series of FPMD simulations. We consider a model of growth where unreduced $\text{PtCl}_2(\text{H}_2\text{O})_2$ complexes react with neutral clusters before reduction. Both in gas-phase simulations and in simulations that explicitly take into account the water environment we observe that the Pt(II) complexes can spontaneously react with Pt_{12} , $\text{Pt}_{12}\text{Cl}_4$, and $\text{Pt}_{13}\text{Cl}_6$ clusters and are completely incorporated into the cluster structure.

The aggregation takes place with a considerable rearrangement of the cluster structure and involves a redistribution of the chlorine ligands on the cluster surface. The adsorption reaction is promoted by electron donation from the filled d_{z^2} orbital of the square-planar Pt(II) complexes to the empty orbitals of the open-shell clusters that extend outside the cluster surface. This is followed by the full incorporation of the Pt atom originally belonging to the Pt(II) complex into the cluster structure, which increases the mean atomic coordination number and thus the cohesive energy per atom of the whole cluster.

The energy barriers associated with the adsorption/incorporation process appear to be negligible at room temperature, suggesting that, in general, low-energy structural rearrangements and ligand fluxionality should be taken into account to realize a

controlled growth of noble-metal clusters in reduction baths. The mechanism suggested by the simulations is fully consistent with the autoaccelerating kinetics of the process of cluster growth and with a face-capping growth mechanism that can account for shape-controlled cluster fabrication.

Ciacchi et al.⁴⁴ investigated the initial nucleation of platinum clusters in synthesis of Pt nanocrystals with K_2PtCl_4 as a metal precursor by a series of FPMD (first principle of molecular dynamic) simulations. They propose a mechanism that the metal precursor compounds can be directly converted into nuclei and add to other precursor-based nuclei or growing nanocrystals without passing through a zero-valent state. They also show that, in synthesis of Pt nanocrystals with K_2PtCl_4 as a metal precursor, a Pt^{II} - Pt^I dimer stabilized with Cl^- can be formed directly from two dissolved $PtCl_2(H_2O)_2$ complexes through the giving of one electron. In this case, the $PtCl_2(H_2O)_2$ complex is the hydrolysis product of $PtCl_4^{2-}$. After that the Pt^I - Pt^{II} dimer is transformed subsequently into a Pt^I - Pt^I dimer by the addition of another electron and the loss of Cl^- . The interesting part is that both the Pt^{II} - Pt^I and Pt^I - Pt^I dimers can react with a third $PtCl_2(H_2O)_2$ complex to form a trimer by blending together to a third reduction step. These dimers and trimers which are partially reduced probably stand for early intermediate units on the way to the formation of larger clusters or nuclei.

Due to orbital delocalization, the dimers and trimers have higher electron affinities than the precursor. Therefore, in the reduction process that likely happens is the electron transfer from the reductant to these dimeric and trimeric units. In this mechanism, the possibility of monomeric precursor complexes to be reduced directly into atoms and then adding to nuclei or growing seeds is omitted. Either the addition of Pt^{II} complexes to a cluster or the detachment of a ligand from a cluster can dramatically accelerate the growth of a metal nanocrystal, which is generally known as autocatalytic growth.^{45,41} The reduction mechanism above is only favorable when employing a mild reducing agent and/or a high concentration of metal precursor. In order that the cluster to be fully reduced into the zero-valent state, its surface is terminated by positively charged metal ions coordinated to ligands or solvated by solvent molecules.

Yao et al. also suggest two distinct nucleation pathways mediated by the reductants in synthesis of Pt nanocrystal from $PtCl_4^{2-}$ ions as schematically shown in Figure 2.7. By employing an *in-situ* characterization UV-vis spectroscopy which can give a direct

evidence and data analysis from XAFS, they hypothesize the scenario of the reductant-manipulated of the nucleation process as follows. When the weak reductant was used, the reduction rate would be substantially slowed down, and the PtCl_4^{2-} ions may be partially reduced into PtCl_3^{2-} ions first. Afterward, two PtCl_3^{2-} ions complex, together via a metal–metal bond, forms a $\text{Cl}_3^{2-}\text{Pt}-\text{PtCl}_3^{2-}$ dimer cluster. Then, these preformed dimer clusters are polymerized to longer linear “Pt.Cl” complexes. This nucleation pathway is consistent with the previous speculation which suggested the formation of a $\text{Pt}^{\text{II}}-\text{Pt}^{\text{I}}$ dimer stabilized with Cl^- in the case of moderate reduction of K_2PtCl_4 precursor, based on the first-principles molecular dynamics simulations.⁴⁴ In case of using a relatively stronger reductant, the PtCl_4^{2-} ions is reduced completely into zero valent Pt^0 atoms which then aggregate into Pt_n^0 (such as Pt_{20} , Pt_{30} , etc.) clusters.

These nucleation pathways have been experimentally elucidated by Yao et al in *in-situ* measurements combining quick-XAFS and UV–vis spectroscopies. The *in-situ* studies confirm that nucleation pathways of Pt nanocrystal are strongly related with the strength of the used reductants. As a result, the produced Pt nanocrystals possess different shapes which show the thermodynamically favored sphere and kinetically controlled wirelike morphologies. These measurements underline the important role of the reductant in mediating the nucleation processes.

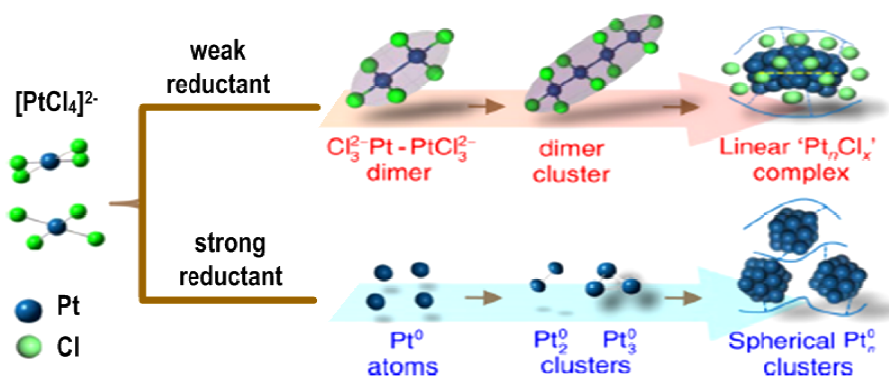


Figure 2.7 Schematic representations of reaction pathways controlled by reductants. When the metal precursor PtCl_4^{2-} ions are reduced by a weak reductant, the intermediate $\text{Cl}_3^{2-}\text{Pt}-\text{PtCl}_3^{2-}$ dimer and the subsequent dimer clusters and their aggregations into higher linear ‘ Pt_nCl_x ’ complexes are formed in the nucleation stage. For the stronger reducing agent, PtCl_4^{2-} ions are reduced into Pt^0 atom which then aggregated into Pt_2^0 , Pt_3^0 and large Pt_n^0 clusters. (Modified from Yao et al.⁴⁶).

Changing to the anisotropic structure of the nanoparticle can enhance its catalytic activity.²⁰ Large surface areas for a given quantity of materials make them good for adsorption at specific sites. Studies on the platinum nanoparticles showed enhanced and selective catalytic activities for different morphologies compared to spherical nanoparticles.⁴⁷ Increasing the number of edges, crystallographic facets, corners, and faces are of critical importance in controlling the catalytic activity and selectivity of metal nanoparticles.

A significant fraction of the total number of atoms in nanostructures is coordinatively undersaturated with respect to the equilibrium bulk structure. Several types of coordinatively undersaturated sites exist on all three-dimensional nanoparticles such as terraces, edges, and kinks which are often summarized as “roughness”. The distribution of these sites distribution is controlled by the morphology of the nanoparticle. It has been suspected for a long time that these sites are representing the active sites.⁴⁸ For instance, Robota et.al (1985)⁴⁹ found that there is a barrier for dissociation of H₂ on the closely packed (111) of nickel while there is no barrier on the open (110) surface. Kratzer et.al (1996) also studied H₂ dissociation over Cu(100) and Cu(111) surfaces and show that the (100) surface is the more reactive one, as would be expected from the lower coordination of the metal atoms in this surface compared to the (111) surface.⁵⁰ Therefore, it would generally be regarded that open surfaces (with lower coordinated surface atoms) are more reactive than closely packed ones, despite of the molecule and the metal considered. There may be other factors having to do with the local bonding of the molecule to the surface that also influence the barrier.⁵¹

2.4. Preparation of supported catalysts with microemulsions

The classic heterogeneous catalysts consist of active metal nanoparticles and a support material such as alumina or silicates. Conventional techniques for the synthesis of supported catalysts contain one or more of the following steps: impregnation, precipitation, coating, rewashing, ion-exchange, pulverization, drying, and calcination. The primary aim of depositing active metal nanoparticles to a support material is to obtain the catalyst in a highly dispersed form. This feature of supported catalysts is particularly important with regard to precious metal catalysts, because it allows more effective usage of the metal than can be achieved in bulk-metal systems. For the metal

catalysts the use of the support is often primarily aimed at improving the catalyst stability. This can be achieved by suitable interaction between the active material and the support.⁵²

As already mentioned in the previous chapter, the particle structure (size and shape) and dispersion of the nanoparticles on the support material determine the catalytic activity and selectivity. On the other hand, the structure, composition and the dispersion of the catalyst may change under the reaction conditions, and thus their performance could be time dependent. Therefore, the synthesis of highly active and stable catalysts still remains a challenging task that constantly grows and improves.

Irrespective of how good the preparation of design nanoparticles is inside of microemulsion droplets, their stability is limited. To increase the stability they need to be transferred and deposited on a support material. In order to obtain a well dispersed supported catalyst, it is necessary to maintain the homogeneous distribution when transferring the particles onto the support. Besides, the particles have to adhere strongly to the support in order to minimize the sintering of the particles at high temperatures. A proper mixing of the microemulsions together with the support powder will increase the possibility of obtaining a homogeneous distribution of the particles on the support. However, this is a difficult task and the success of the method is very much dependent on the properties of the support.

The most common way to carry out this process is the so called solvent destabilization, i.e. to add a solvent like tetra-hydrofuran (THF) to the microemulsion which will destabilize the solution. If the support powder is added at the same time as the solvent, the particles will stick onto the support. This method, however, has some disadvantages such as the difficulty in creating a uniform destabilization in the whole microemulsion system and also producing more liquid waste because more solvent is added to the system. In this work, a new method to prepare supported catalysts from microemulsions is introduced, namely thermo-destabilization of microemulsions. The principle of this method is changing the temperature of microemulsion systems to break the microemulsion droplets so that the nanoparticles can be released and thus be deposited onto the support material. The advantages of this method, in contrast to the solvent destabilization, are the easiness to create a uniform destabilization in the

whole microemulsion system and not producing more liquid waste because no solvent is added into the system.

In this method, the surface charges of the involved materials, i.e. the nanoparticles and the support, which are indicated by the measured zeta potential, play an important role for the degree of dispersion. In principle, the attractive zeta potential can be used to predict the interaction between the nanoparticles and the support material during the deposition process. The preparation of supported catalysts with the thermo-destabilization method will be discussed in more detail in Chapter 4.

References

1. Lopez-Quintela M.A., *Current Opinion in Colloid and Interface Science*, 2003, **8**, 137–144.
2. Y. Yin and A. P. Alivisatos, *Nature*, 2005, **437**, 664–670.
3. C. J. Dalmaschio, C. Ribeiro, and E. R. Leite, *Nanoscale*, 2010, **2**, 2336–2345.
4. V. K. LaMer and R. H. Dinegar, *J. Am. Chem. Soc.*, 1950, **72**, 4847–4854.
5. M. A. Watzky and R. G. Finke, *J. Am. Chem. Soc.*, 1997, **119**, 10382–10400.
6. C. Tojo, M. C. Blanco, F. Rivadulla, and M. A. López-Quintela, *Langmuir*, 1997, **13**, 1970–1977.
7. S. Quintillán, C. Tojo, M. C. Blanco, and M. A. López-Quintela, *Langmuir*, 2001, **17**, 7251–7254.
8. J. L. Schmitt, G. W. Adams, and R. A. Zalabsky, *The Journal of Chemical Physics*, 1982, **77**, 2089–2097.
9. C. Tojo, M. D. Dios, and F. Barroso, *Materials*, 2010, **4**, 55–72.
10. Y. Xiong and Y. Xia, *Advanced Materials*, 2007, **19**, 3385 – 3391.
11. Y. Jun, J.-H. Lee, J. Choi, and J. Cheon, *J. Phys. Chem. B*, 2005, **109**, 14795–14806.
12. J. Polleux, N. Pinna, M. Antonietti, and M. Niederberger, *Advanced Materials*, 2004, **16**, 436–439.
13. M. López-Quintela, J. Rivas, M. Blanco, and C. Tojo, in *Nanoscale Materials*, 2003, pp. 135–155.
14. M. Boutonnet, J. Kizling, R. Touroude, G. Maire, and P. Stenius, *Catal Lett*, 1991, **9**, 347–354.

15. E. E. Finney and R. G. Finke, *Journal of Colloid and Interface Science*, 2008, **317**, 351–374.
16. A. R. Tao, S. Habas, and P. Yang, *Small*, 2008, **4**, 310–325.
17. G. Berhault, M. Bausach, L. Bisson, L. Becerra, C. Thomazeau, and D. Uzio, *J. Phys. Chem. C*, 2007, **111**, 5915–5925.
18. S. Cheong, J. D. Watt, and R. D. Tilley, *Nanoscale*, 2010, **2**, 2045.
19. C. J. Murphy, T. K. Sau, A. M. Gole, C. J. Orendorff, J. Gao, L. Gou, S. E. Hunyadi, and T. Li, *The Journal of Physical Chemistry B*, 2005, **109**, 13857–13870.
20. P. R. Sajanalal, T. S. Sreeprasad, A. K. Samal, and T. Pradeep, *Nano Rev*, 2011, **2**.
21. Y. Xia, Y. Xiong, B. Lim, and S. E. Skrabalak, *Angewandte Chemie International Edition*, 2009, **48**, 60–103.
22. R. L. Whetten and W. M. Gelbart, *J. Phys. Chem.*, 1994, **98**, 3544–3549.
23. D. V. Leff, P. C. Ohara, J. R. Heath, and W. M. Gelbart, *J. Phys. Chem.*, 1995, **99**, 7036–7041.
24. M. A. El-Sayed, *Acc. Chem. Res.*, 2001, **34**, 257–264.
25. R. Narayanan and M. A. El-Sayed, *The Journal of Physical Chemistry B*, 2004, **108**, 5726–5733.
26. J. M. Petroski, Z. L. Wang, T. C. Green, and M. A. El-Sayed, *The Journal of Physical Chemistry B*, 1998, **102**, 3316–3320.
27. H. Lee, S. E. Habas, S. Kveskin, D. Butcher, G. A. Somorjai, and P. Yang, *Angewandte Chemie International Edition*, 2006, **45**, 7824–7828.
28. C.-K. Tsung, J. N. Kuhn, W. Huang, C. Aliaga, L.-I. Hung, G. A. Somorjai, and P. Yang, *Journal of the American Chemical Society*, 2009, **131**, 5816–5822.
29. B. Y. Xia, J. N. Wang, and X. X. Wang, *The Journal of Physical Chemistry C*, 2009, **113**, 18115–18120.
30. J. Watt, N. Young, S. Haigh, A. Kirkland, and R. D. Tilley, *Advanced Materials*, 2009, **21**, 2288–2293.
31. L. Manna, Wang, R. Cingolani, and A. P. Alivisatos, *J. Phys. Chem. B*, 2005, **109**, 6183–6192.
32. W. W. Yu, Y. A. Wang, and X. Peng, *Chem. Mater.*, 2003, **15**, 4300–4308.
33. L. Manna, E. C. Scher, and A. P. Alivisatos, *J. Am. Chem. Soc.*, 2000, **122**, 12700–12706.
34. Y. Jun, M. F. Casula, J.-H. Sim, S. Y. Kim, J. Cheon, and A. P. Alivisatos, *J. Am. Chem. Soc.*, 2003, **125**, 15981–15985.
35. A. P. Alivisatos, *Science*, 2000, **289**, 736–737.

36. R. L. Penn and J. F. Banfield, *Geochimica et Cosmochimica Acta*, 1999, **63**, 1549–1557.
37. J. H. Yu, J. Joo, H. M. Park, S.-I. Baik, Y. W. Kim, S. C. Kim, and T. Hyeon, *J. Am. Chem. Soc.*, 2005, **127**, 5662–5670.
38. T. K. Sau and A. L. Rogach, *Advanced Materials*, 2010, **22**, 1781–1804.
39. B. Lim, M. Jiang, J. Tao, P. H. C. Camargo, Y. Zhu, and Y. Xia, *Advanced Functional Materials*, 2009, **19**, 189–200.
40. A. Henglein and M. Giersig, *J. Phys. Chem. B*, 2000, **104**, 6767–6772.
41. L. C. Ciacchi, M. Mertig, R. Seidel, W. Pompe, and A. D. Vita, *Nanotechnology*, 2003, **14**, 840–848.
42. T. Yao, Z. Sun, Y. Li, Z. Pan, H. Wei, Y. Xie, M. Nomura, Y. Niwa, W. Yan, Z. Wu, Y. Jiang, Q. Liu, and S. Wei, *J. Am. Chem. Soc.*, 2010, **132**, 7696–7701.
43. D. G. Duff, P. P. Edwards, and B. F. G. Johnson, *J. Phys. Chem.*, 1995, **99**, 15934–15944.
44. Ciacchi, L.C, Pompe, W, and De Vita, A, *J. Am. Chem. Soc.*, 2001, **123**, 7371–7380.
45. Y. Xia, Y. Xiong, B. Lim, and S. E. Skrabalak, *Angew. Chem. Int. Ed. Engl*, 2009, **48**, 60–103.
46. T. Yao, S. Liu, Z. Sun, Y. Li, S. He, H. Cheng, Y. Xie, Q. Liu, Y. Jiang, Z. Wu, Z. Pan, W. Yan, and S. Wei, *J. Am. Chem. Soc.*, 2012, **134**, 9410–9416.
47. I. Lee, R. Morales, M. A. Albiter, and F. Zaera, *Proceedings of the National Academy of Sciences*, 2008, **105**, 15241–15246.
48. R. Schlögl and S. B. Abd Hamid, *Angewandte Chemie International Edition*, 2004, **43**, 1628–1637.
49. H. Robota, W. Vielhaber, and G. Ertl, *Surface Science*, 1984, **136**, 111–120.
50. P. Kratzer, B. Hammer, and J. . Nørskov, *Surface Science*, 1996, **359**, 45–53.
51. J. K. Norsko, *Reports on Progress in Physics*, 1990, **53**, 1253–1295.
52. C. Kemball, D. A. Dowden, G. J. K. Acres, A. J. Bird, J. W. Jenkins, and F. King, in *Catalysis*, 2007.

Chapter 3

General Experimental Section

3.1 Chemicals

3.1.1 Synthesis of supported metal catalyst.

The chemicals used for the preparation of different metal nanoparticles with microemulsions method were the following. For the water phase containing the metal salt: Hexachloroplatinic acid hydrate (99.9%, Sigma-Aldrich) and Potassium tetrachloro-platinate(II) (99.9%, Sigma-Aldrich), Silver Nitrate (99.9%, Sigma-Aldrich), Palladium Chloride (99.9%, Sigma-Aldrich) and Ruthenium chloride (99.9%, Sigma-Aldrich). All are dissolved in deionized water. To prepare the Pd salt solution, Palladium Chloride is dissolved in cold deionized water and solubilized by as little NaCl as possible. For the water phase containing the reducing agent: hydrazine monohydrate (98%, Sigma-Aldrich) and L-(+)-ascorbic acid (>99%, Alfa Aesar), both are dissolved in deionized water. These are then prepared for different concentrations.

As surfactant component three kinds of surfactants were tested: (1) non-ionic surfactants: 2-[4-(2,4,4-trimethylpentan-2-yl)phenoxy]ethanol (trade name: Triton X-100, ~100% purity, Sigma-Aldrich) and [2-[(2R,3S,4R)-3,4-dihydroxyoxolan-2-yl]-2-hydroxyethyl] (Z)-octadec-9-enoate (trade name: Span 80, ~70% purity, Sigma-Aldrich); (2) anionic surfactant: sodium 1,4-bis(2-ethylhexoxy)-1,4-dioxobutane-2-sulfonate (trade name: AOT, 98% purity, Sigma Aldrich); (3) cationic surfactant: Cetyl trimethylammonium bromide (CTAB, ~99% purity, Sigma Aldrich). The other

components are 1-pentanol ($\geq 98\%$ purity, Carl-Roth) as co-surfactant and Cyclohexane ($\geq 99.5\%$ purity, Carl-Roth) as the oil phase. Both were used as received. All the chemicals above were used without further purification. The support materials used in the deposition process were (base, neutral and acid)- Al_2O_3 (Sigma-Aldrich), SiO_2 (Sigma-Aldrich), $\alpha\text{-Al}_2\text{O}_3$ (Alfa Aesar), dioxosilane (trade name: Sipernat 310, Evonik) and self prepared SBA-15 and MCM-41 according to the method reported by Zhao et.al. For the washing of the catalysts after the synthesis, acetone ($\geq 99.8\%$ purity, Carl Roth) was used.

Catalytic Testing. In catalytic testing, there are four kinds of substrates that were used in hydrogenation reactions, i.e. α -Methyl Styrene (99%, Sigma-Aldrich), Levulinic Acid (98% purity, Sigma-Aldrich), Methyl Crotonate (99% purity, Sigma-Aldrich), and Itaconic Acid (99% purity, Sigma-Aldrich). As the solvent Methanol ($\geq 99.9\%$ purity, Carl-Roth) was used. All chemicals were used as received.

3.2 Experimental Procedure

3.2.1 Phase Behaviour of Microemulsion Systems

The behavior of microemulsions depends upon three parameters namely pressure, temperature and concentration of the components (water–oil–surfactant). The principle of the synthesis method in this work is utilizing the temperature change to destabilize the microemulsions so that the metal nanoparticles inside the droplets can be released and are thus ready to attach onto the support material. Another thing that also needs to be determined is a composition which can produce a microemulsion with small droplet size at room temperature. Therefore, it is necessary to establish the phase behavior of the microemulsion system so that the composition and the corresponding temperature change can be identified. The mass fraction of the oil in the mixture of oil and water is defined by $\alpha = m_o / (m_o + m_w)$. The mass fraction of surfactant is defined by γ . Because co-surfactant is added to the microemulsions, surfactant is considered now as a pseudo single phase. Hence, $\gamma = (m_s + m_{co-s}) / (m_w + m_o + m_s + m_{co-s})$. The mass ratio of co-surfactant to surfactant is defined by δ . Because the behaviour of microemulsions depends upon three parameters, the complete phase diagram has a three-dimensional

structure (a prism). Several two-dimensional phase diagrams can be extracted from the prism, depending on the number of variables involved, to simplify the phase behavior such as fish diagram (γ vs T) or Shinoda diagram (α vs T). However, as previously mentioned, this method is only needed to identify the temperature range that causes the phase change. The fish diagram is sufficient to provide the information. The procedure to measure a fish diagram is the following. Test tubes were filled with different concentration of the surfactants and co-surfactants (as illustrated in Table 3.1) at the fixed α (the mass ratio of oil to oil and water was the same in all test tubes) with the total volume of 7.5 ml. The sequence in which the components were added was (1) oil, (2) surfactant, (3) co-surfactant and lastly (4) water. The microemulsions needed to be mixed thoroughly to get stabilized. Afterwards, the test tubes were immersed in a thermostated, transparent water glass bath, as shown in Figure 3.1. The phase behavior of the microemulsions was observed every 15 to 20 minutes, in steps of 5 °C between 10 °C and 70 °C. So the temperature in the water glass bath was increased step by step. The observation of the phases and phase changes gave information needed to produce the fish diagrams.

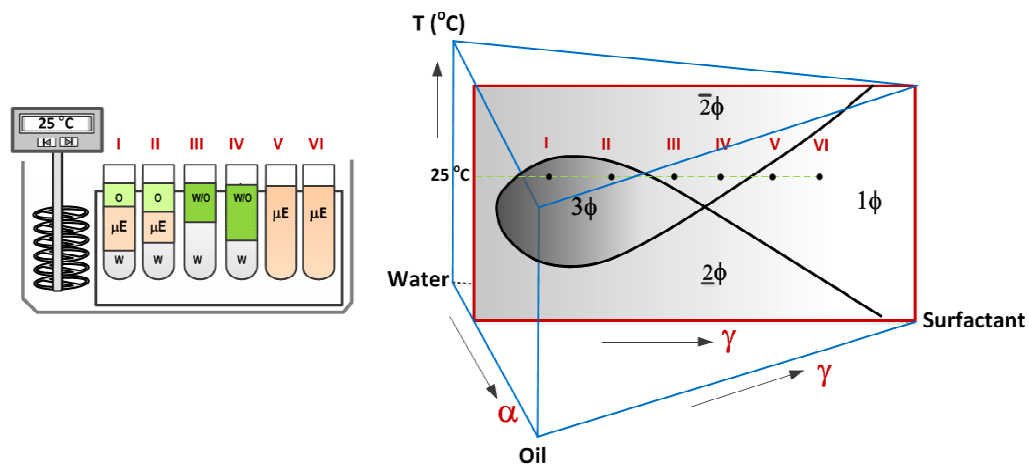


Figure 3.1 Schematic illustration of the experiment to prepare a fish diagram

The first attempt is to measure the fish diagrams with different surfactants to find a proper surfactant which can provide a complete fish diagram in the range of 5 – 70 °C. For that purpose, anionic, cationic and nonionic surfactants were tested. From the fish diagram of the chosen surfactant, the microemulsion composition that gives small droplets (high γ) at room temperature needs to be determined. After choosing the

appropriate composition, the influence of the metal salts and the reducing agent on the phase behavior has to be tested.

3.2.2. Synthesis of supported metal nanoparticles

After determining the destabilization temperature of microemulsion containing the metal salts and the reducing agent, the synthesis of supported metal particles can be carried out. Two microemulsions @50 ml are prepared, one containing the reducing agent solution and the other one containing the dissolved metal precursor. Tabel 3-2 shows the concentration of metal salts and reducing agents (except the variation of concentrations) at different composition that are used in this work. For all the synthesis of the supported metal nanoparticles, a semi batch reactor was used. The reactor is the 200-ml double-walled glass reactor circulated with water from the thermostat to adjust the reactor temperature. To control the heating rate during the deposition process, the thermostat is regulated by a computer program. The reactor is also equipped with a stirrer that has three diagonal blades modulated on top of each other. Each diagonal blade stirrer has two blade stirrers as seen in Figure 3.2.

Table 3.1 Example of an observation table to prepare a fish diagram where γ is varied at fixed $\alpha = 0.5$ and $\delta = 1$

Mass (g)				α	γ	Phase at temperature													
Water	Cyclohex	Triton	Pentanol			10 °C	15 °C	20 °C	25 °C	30 °C	35 °C	40 °C	45 °C	50 °C	55 °C	60 °C	65 °C	70 °C	
4.75	4.75	0.25	0.25	0.5	0.05	2	2	2	2	2	2	3	3	2	2	2	2	2	
4.5	4.5	0.5	0.5	0.5	0.1	2	2	2	2	2	3	3	2	2	2	2	2	2	
4	4	1	1	0.5	0.2	2	2	2	2	2	2	2	2	2	2	2	2	2	
3.5	3.5	1.5	1.5	0.5	0.3	1	1	1	2	2	2	2	2	2	2	2	2	2	
3	3	2	2	0.5	0.4	1	1	1	2	2	2	2	2	2	2	2	2	2	
2.5	2.5	2.5	2.5	0.5	0.5	1	1	1	2	2	2	2	2	2	2	2	2	2	
2	2	3	3	0.5	0.6	1	1	1	1	2	2	2	2	2	2	2	2	2	
1.5	1.5	3.5	3.5	0.5	0.7	1	1	1	1	1	2	2	2	2	2	2	2	2	
1.33	1.33	4	4	0.5	0.75	1	1	1	1	1	1	2	2	2	2	2	2	2	
1.13	1.13	4.5	4.5	0.5	0.8	1	1	1	1	1	1	1	1	1	1	1	1	1	
0.88	0.88	5	5	0.5	0.85	1	1	1	1	1	1	1	1	1	1	1	1	1	
0.61	0.61	5.5	5.5	0.5	0.9	1	1	1	1	1	1	1	1	1	1	1	1	1	

The microemulsion with the reducing agent is added at 0.2 ml/s with the micro pump to the reactor which beforehand has been filled with the microemulsion containing the metal precursor. The reduction takes place under stirring at 700 rpm for 1 hour (if not varied) at 25 °C. The color of the solution changed to dark brown indicating the

reduction of Pt ions to Pt⁰ species. Afterwards, the pre-calcined (if not varied) support material is added directly to the reactor and the temperature is increased to the destabilization temperature, to open the droplets and start the deposition. After 2 hours (if not varied), the stirrer is stopped. The supported catalyst is gravitationally settled and the mixture is cooled down. The catalyst is thoroughly separated from the mixture, washed with pure acetone carefully three times and then calcined at 300 °C for 2 hours.

In case of the synthesis of Ag supported catalyst, the reduction process was completed after 30 minutes. A sample taken from the reaction solution is then measured in the UV-Vis spectrometer (to measure the final concentration of Ag) while the prepared support material is quickly fed into the reactor.

Table 3.2 The compositions of microemulsions that are used in this work

Microemulsion component	Microemulsion I	Microemulsion II	Mass fraction		
			$\alpha_1 = 0.92$ $\gamma_1 = 0.3$ ($\omega_1 = 12.96$)	$\alpha_2 = 0.5$ $\gamma_2 = 0.7$ ($\omega_2 = 14.88$)	$\alpha_3 = 0.75$ $\gamma_3 = 0.4$ ($\omega_3 = 26.96$)
Water phase	H ₂ PtCl ₆	N ₂ H ₄	5.6	15	15
	H ₂ PtCl ₆	Ascorbic acid			
	K ₂ PtCl ₄	Ascorbic acid			
	AgNO ₃	N ₂ H ₄			
	PdCl ₂	AA			
	RuCl ₃	N ₂ H ₄			
Oil phase	Cyclohexane	Cyclohexane	64.4	15	45
Co-surfactant	Pentanol	Pentanol	15	35	20
Surfactant	Triton X-100	Triton X-100	15	35	20

After 30 minutes of deposition, a sample is taken from the mixture to be measured in the UV-Vis spectrometer. Before measured with UV, the solid particles of the support must surely be settled onto the bottom of the cuvette. The clear reaction solution is then quickly replaced to another cuvette and its absorbance measured. Every 30 minutes a sample was taken from the reaction solution to be measured to follow the deposition process. After the absorbance of the solution reaction show no significant increase anymore, the reaction is stopped.

The chemical reactions that are involved in the synthesis of metal nanoparticles during the collisions and interchange of the droplets are the following.

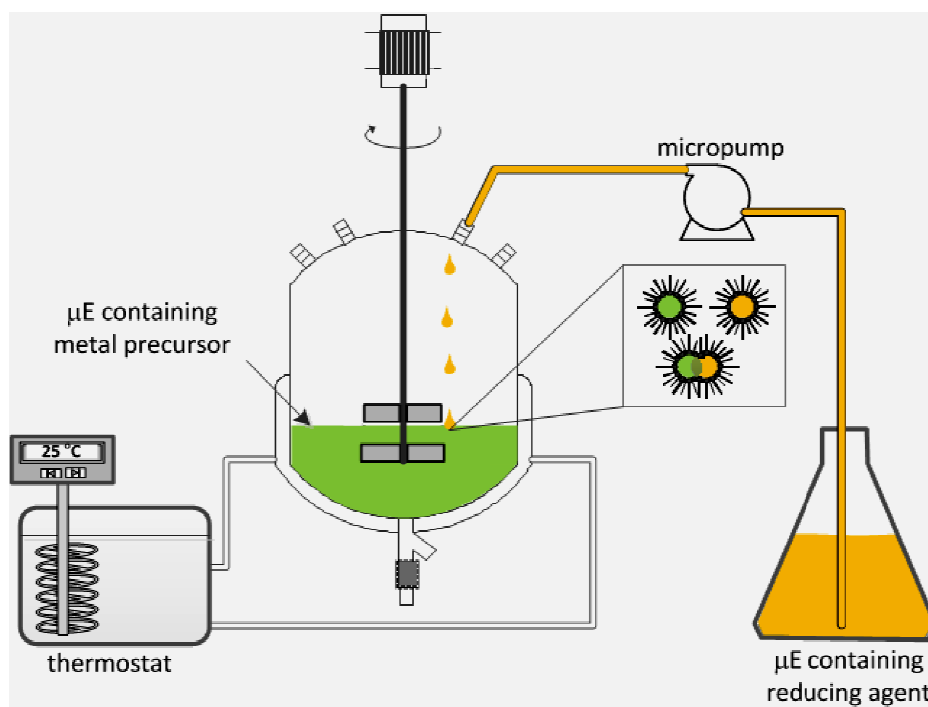
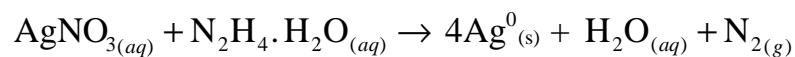
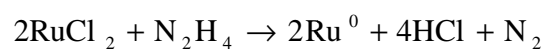
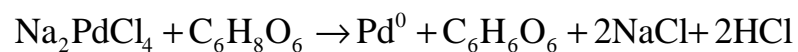
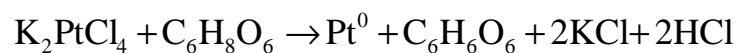
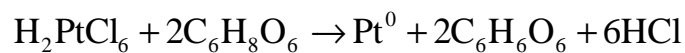
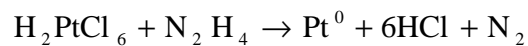


Figure 3.2 The reactor setup for synthesis of supported nanoparticles via thermodestabilization of microemulsions

3.2.3 Catalytic testing

The produced supported metal catalysts were tested in hydrogenation of some substrates as shown in Table 3.2 in order to determine their activity. The reaction is performed in a 200-ml double-walled glass reactor which is equipped with a thermostat, flow controller and computer. The complete setup of hydrogenation reaction system is schematically shown in Figure 3.3.

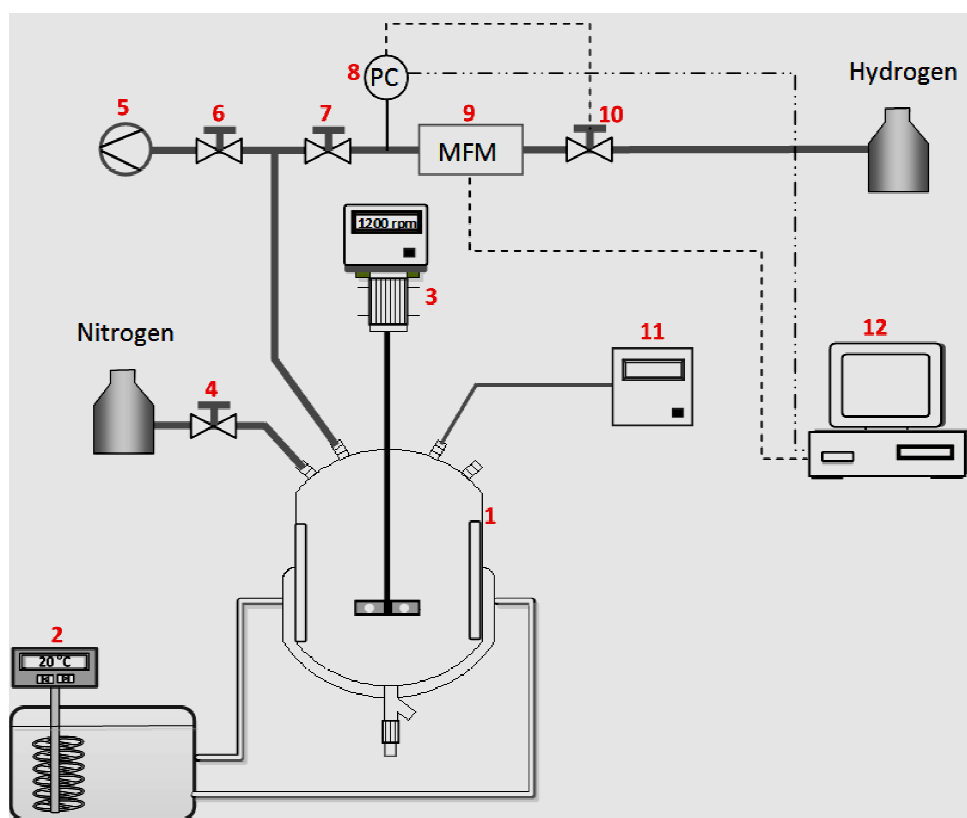


Figure 3.3 The hydrogenation reactor setup for catalytic testing

First of all, all the equipments such as thermostat (2), vacuum pump (5), pressure controller (8 and 10), mass flow meter (9), and computer (12), are turned on. The reactor (1) is cleaned by rinsing it with acetone and then evacuated with vacuum pump by opening the valve (6) until it reaches the lowest pressure, then the valve (6) is closed. During the evacuation, the pressure is checked by observing the pressure indicator (11), to make sure that there is no leakage. The computer programs which connected to the controller (8) and mass flow meter (9) are then activated and the thermostat is regulated at 20 °C. Afterwards, the weighed amount of catalyst is feed into the reactor followed by adding 100 ml methanol (as the solvent) and certain

amount of the substrate subsequently. All the openings of the reactor are closed properly and the mixture is evacuated by opening again valve (6) until the pressure indicator shows 300 mbar. After holding it for 1 minute, valve (4) is opened to fill the reactor with nitrogen until the pressure indicator shows 1100 mbar. This evacuation process is done three times under a slow stirring (with the stirrer 3). Then the stirrer is adjusted to 1200 rpm and then turned off. Figure 3.4 shows the excel program for the hydrogenation reaction. The experimental data such as: the name and amount of catalyst, the name and molar mass of substrate, the temperature and pressure of reaction, are added to the excel sheet (upper left). After that the valve (7) is opened to let hydrogen fill the reactor until the pressure indicator (11) shows 1100 mbar.

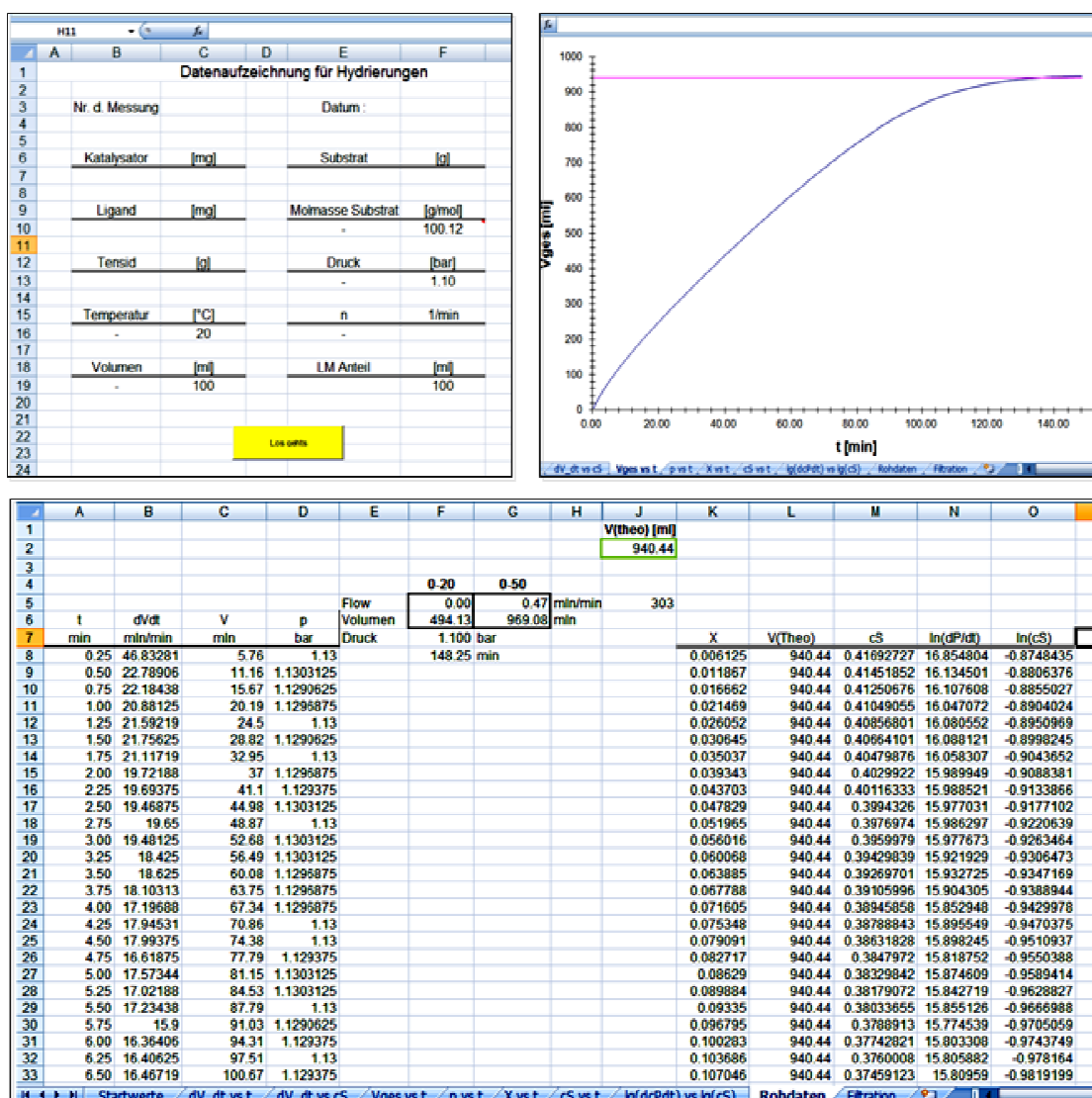


Figure 3.4 The excel program for the hydrogenation reaction.

The reaction is started by pushing the yellow 'Los geht' button on the computer screen (Figure 3.4, upper left). simultaneously with switching on the stirrer. The amount of H₂ flow into the reactor is monitored over time and recorded on the excel sheet (upper right). The hydrogenation is considered complete when no more H₂ is consumed for the reaction (constant value of column C in the bottom of Figure 3.4).

The list of hydrogenation reactions that were used for catalytic testing is shown in Figure 3.5. All the reaction were carried out with the same procedures, except the hydrogenation of levulinic acid, were performed at 70 °C and the H₂ pressure is kept 1,3 bar instead of 1,1 bar.

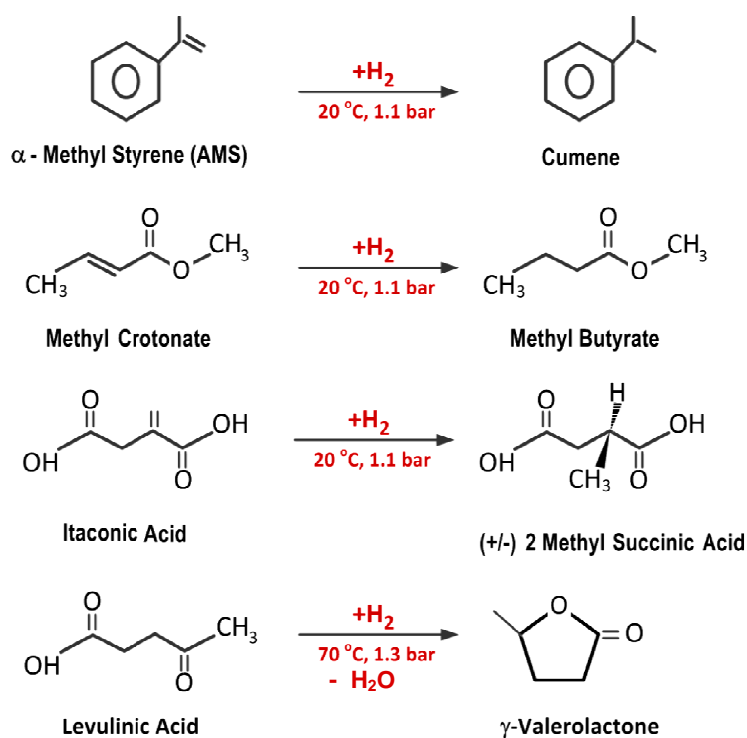


Figure 3.5 List of hydrogenation reactions for catalytic testing

3.3 Catalyst performance

In this work, the catalyst performance is evaluated by activity. The activity of the catalyst is determined by using the initial reaction rate at the very beginning of the

hydrogenation (first five minutes) divided by mass of the metal catalyst used in the reaction.

$$\text{Activity} = \frac{r_0}{m_{\text{Pt}}} \left[\frac{\text{mol}}{\text{s}\cdot\text{g}} \right] \quad (3.1)$$

An example for calculating the activity is available in **Appendix C**. The mass of the metal catalyst is determined by ICP analysis. The sample for ICP is prepared by the following steps. The metal supported catalyst that has been tested with hydrogenation reaction is collected in an Erlenmeyer flask followed by adding 50 ml of King water. The mixture is stirred with a magnetic stirrer overnight to make sure that all the metal has been dissolved in the King water. After the stirrer is turned off, the mixture is filtered with the Whatman filter paper. A portion of 20 ml from the filtrate is taken to be analyzed by ICP.

3.4 Catalyst characterization

The supported metal catalysts usually consist of nanoparticles with different size, shape, and crystal planes which affect their activity. The catalysts produced in this work were characterized with Transmission Electron Microscopy (TEM), Scanning Electron Microscopy (SEM), X-ray Diffraction (XRD), Brunauer-Emmett-Teller (BET) surface area, UV-spectroscopy, Infrared Spectroscopy (IR), Inductively Coupled Plasma Optical Emission Spectroscopy (ICP-OES), and Zeta potential (ζ -potential). In the following sections, these characterization techniques are presented in detail.

3.4.1 Transmission Electron Microscopy (TEM)

Transmission electron microscopy (TEM) is widely used technique for imaging nanoparticles at atomic resolution. The size and the shape of the metal nanoparticles either in the microemulsion or on the support catalyst in this work were investigated by TEM. The sample from the microemulsion was prepared by putting a drop of microemulsion on the carbon grid, and the organic substances were removed by plasma cleaning. The TEM was performed on the microemulsions by dropping small aliquots of the microemulsions onto TEM grids, allowing the solvent evaporates, and then washing the grids with the microemulsion with acetone to remove residual surfactant.

The sample from the supported metal catalyst was prepared by putting the fine fragments of the catalyst on the carbon grid. The sample has to be thin to get a clear image. The sample then subjected to a high voltage beam of electrons. The dark spots on the positive of the detecting film correspond to dense areas in the sample that inhibit electron transmission. These dark spots form the sketch of metal particles or crystallites and thus, their sizes can be determined. The TEM devices used for this study are Philips CM200/FEG high-resolution TEM (HRTEM) operated at 200 kV, FEI Titan 80-300 (sub-Angstrom resolution, able to investigate at atomic scale) and FEI TECNAI G² 20 S-TWIN transmission electron microscope equipped with a GATAN MS794 P charge-coupled device camera. All are equipped with an energy dispersive X-ray detector (EDX).

3.4.2 Scanning Electron Microscope (SEM)

Scanning electron microscope (SEM) is used in this work to analyze the dispersion of the metal nanoparticles on the outer part of the support material. SEM is a type of electron microscope that images a sample by scanning the surface of the sample with a high energy beam of electrons in a raster scan pattern. The interaction between the electrons and the sample produces different signals provides information about the surface of the sample. The spatial resolution of the SEM depends on the spot size of the electron and limited by the size of the interaction volume (the extent to which the material interacts with the electron beam). The spot size and the interaction volume are both large compared to the distances between atoms, so the resolution of the SEM is not high enough to image individual atoms, as is possible in the shorter wavelength (i.e. higher energy) TEM. In this work, the high resolution SEM Hitachi S-4000 was used.

3.4.3 Inductively Coupled Plasma Optical Emission Spectroscopy (ICP-OES)

The amount of metal nanoparticles that are deposited on the support material was analyzed by ICP-OES. ICP is an analytical technique which uses plasma as the atomization and the excitation source. Plasma is an electrically neutral, highly ionized gas that consists of ions, electrons, and atoms. ICP operate with pure argon or helium, which makes perfect combustion. The sample was prepared by following step: 300 mg of supported metal catalyst is put into 50 ml of king water and stirred overnight to dissolve all the metal catalyst from the support material. Afterward the mixture is

filtered and the filtrated solution is collected as a sample to be analyzed with ICP. Argon gas is used to create the plasma in the device. The collision of the sample with electrons and charged ions in the plasma results in it being broken into charged ions and giving off radiation at the characteristic wavelengths of the elements involved. The intensities of the wavelengths are measured and by comparison with the wavelengths of known metal concentration (from standard solutions) give information about the metal content in the sample. The device used in this study is the ICP-OES Element 2 (Varian) at low resolution (sample gas 0,863 l/min; plasma power 1350 W).

3.4.4 BET surface area measurement

The Brunauer-Emmett-Teller (BET) method is commonly used for evaluating the surface area of either the supported metal catalysts or the support material. The concept of the BET theory is an extension of the Langmuir theory. One of the basic assumptions of Langmuir Adsorption Isotherm is that adsorption is monolayer. Langmuir adsorption equation is applicable under the conditions of low pressure. Under these low pressure conditions, gaseous molecules will possess high thermal energy and high escape velocity. As a result, less number of gaseous molecules would be available near the surface of adsorbent. Under the condition of high pressure and low temperature, thermal energy of gaseous molecules decreases and more and more gaseous molecules will be available per unit surface area. Due to this situation, multilayer adsorption will occur. The multilayer formation is explained by BET Theory.

The BET equation describes the relationship between N_2 volume adsorbed at a given partial pressure and the volume adsorbed at monolayer coverage. The BET equation is given as:

$$\frac{P}{V_{\text{total}}(P-P_0)} = \frac{1}{V_{\text{mono}}C} + \frac{c-1}{V_{\text{mono}}C} \left(\frac{P}{P_0} \right) \quad (3.2)$$

Where V_{mono} is the adsorbed volume of gas at high pressure conditions to cover the surface with a monolayer of gaseous molecules, The ratio of K_1/K_L is designated C. K_1

is the equilibrium constant when single molecule adsorbed per vacant site and K_L is the equilibrium constant to the saturated vapor liquid equilibrium.

The specific surface areas of the catalysts were measured by the BET method using N_2 adsorption at liquid N_2 temperature in a Micromeritics Gemini III 237 Volumetric Surface Analyzer. The sample was outgassed at 200 °C for 1 h in order to desorb any impurities or moisture from its surface. The assumptions used to derive the BET isotherm are: molecules behave as ideal gas, nitrogen molecules can be adsorbed to each site, each adsorbed molecule provides a site for the adsorption of the molecule in the layer above it, all sites on the surface are equivalent, no interaction between the adsorbates, an adsorbed molecule is motionless, and nitrogen in the second and higher layers are assumed to be liquid like.

3.4.5 X-Ray Diffraction (XRD)

X-ray scattering technique was used to investigate the crystallite size and the crystallographic structure. X-rays are energetic enough to penetrate into the material and their wavelengths are of the same order of magnitude as inter-atomic distances in solids. Thus, a accumulated beam of X-rays is diffracted by the crystalline phases in the sample according to Bragg's Law :

$$n \lambda = 2d \sin \theta \quad (3.3)$$

Where λ is the wavelength of the X-rays, d is the distance between two atomic planes in the crystalline phase, n is the order of the diffraction, and θ the incoming diffraction angle. The angles of diffraction vary for the different planes within the crystal. Thus, every compound or element has its own unique diffraction pattern. The larger the crystals of a given component, the sharper the peaks on the XRD pattern for each crystal plane will be. The structural characterization of the supported metal catalysts was performed by using a D8 ADVANCE X-ray Diffractometer from Bruker AXS equipped with a position-sensitive LynxEye detector (PSD) and a $CuK\alpha$ source by setting the voltage to 40 kV and the current to 40 mA. The XRD profiles for each catalyst were recorded by using the following scan parameters: 2θ range from 15 to 80°.

3.4.6 Zeta potential (ζ -potential)

Particles can bear either positive or negative charges. In this work, the charge of the particles was measured by Zeta potential to analyze the interaction between the metal nanoparticles and the support material. Zeta potential is defined as the potential difference between the dispersion medium and the stationary layer of fluid attached to the dispersed particle. Positively charged particles are more likely to interact with negatively charged particles and vice versa. Particles with same type of charges repulse each other. Highly charged particles, positive or negative, are therefore less likely to agglomerate due to the electric repulsion. Zeta potential is expressed in millivolts and usually found in the range of -70 mV to +70 mV. When the potential is low, attraction exceeds repulsion and the dispersion will break and flocculate. The effective surface charges (ζ -Potential) on the metal nanoparticles and support materials were measured using zeta-potential Zen 3600 (Malvern Instruments Zetasizer, Worcestershire, UK) equipment, with samples thermostated at 25 °C.

3.4.7. UV-Vis spectrometer

Due to the ability to interact with light, silver (Ag) nanoparticles display strong plasmon resonances tuned to any wavelength in the visible spectrum. In this work, the concentration of Ag nanoparticles in the microemulsions was quantified by UV-Visible spectroscopy method. By this way, the yield of the Ag nanoparticles that are successfully deposited on the metal supports can be measured by measuring the absorbance of the microemulsion (after the solid particles of the support is settled onto the bottom of the cuvette).

Chapter 4

A new method to synthesize very active and stable supported metal Pt catalysts: thermo-destabilization of microemulsions

4.1 Introduction

Efforts to increase the activity of catalytic nanoparticles are no longer focused only on reducing their size. Knowing that nanoparticles of the same size but different shape perform differently, many researchers are trying to control the shapes of the nanoparticles.¹ New strategies have been developed to produce multifaceted crystals. These are very active because the more faces the crystals have, the higher the concentration of atomic steps and edges that are readily available to participate in chemical reactions.

During the last decade, there has been a lot of interest in the synthesis of Platinum nanoparticles of different shapes such as tetrahedral, cubic, nanowire, tetrapods, etc.¹ Although many have successfully been produced with different shapes, they still remain in the colloidal state which can only be stable for a limited time. To create more stable catalysts, nanoparticles need to be deposited on a support material. In general, it is difficult to preserve the size and shape of nanoparticles during the deposition process. Furthermore, one also has to consider the dispersion of nanoparticles on the support because it affects the catalyst performance.

Conventionally supported Pt-catalysts are produced by wet impregnation of a support material.²⁻⁶ However, in some cases agglomeration and low dispersion (number of surface Pt atoms/total number of Pt atoms) was observed.⁷ Another attempt that has been frequently used is synthesizing both Pt-nanoparticles and the support material simultaneously.^{8,9} Unfortunately, this results not only in poor control of metal particle size and dispersion but it is also hard to explain the influence of the preparation parameters on the performance of the catalysts.

Microemulsions (μE) are used as media to synthesize Pt-metal catalysts due to the possible control of the size and shape of the nanoparticles¹⁰⁻¹³ by adjusting parameters such as the water to surfactant ratio (ω), kind of surfactant, kind of precursor, initial concentration of metal salt, etc. The fundamental step for the synthesis of nanoparticles via μE is the collision and exchange of water droplets as depicted in Figure 4.1. When a μE containing the Pt-precursor is mixed with a μE containing the reducing agent, a very fast collision and exchange between the droplets occurs due to the dynamic nature of the water droplets in the μE system.

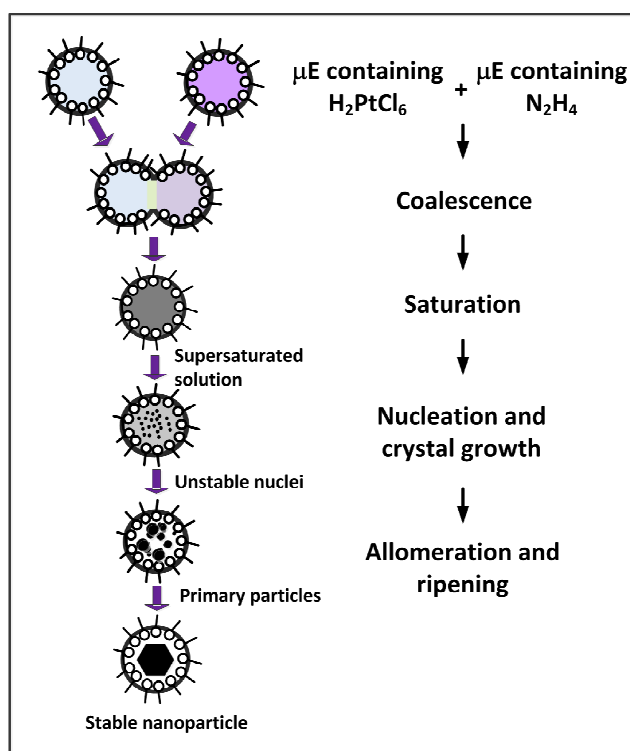


Figure 4.1 Mechanism of Pt nanoparticle formation

The chemical reaction takes place during these processes. Once the solution becomes supersaturated, the nuclei of Platinum nanoparticles are generated and then the growth of the particles takes place inside the water pool until unstable particles are produced. These unstable particles then agglomerate to form bigger particles and after subsequently ripening they become a stable crystal nanoparticle. However as previously mentioned, it is far better to deposit the metal nanoparticles on a support material to increase the thermal and mechanical stability.

Several methods to deposit Pt-nanoparticles from water in oil microemulsions have been reported. For example, one can use an organic solvent to destabilize the microemulsions.¹⁴ The support is added to the nanoparticle suspension and the microemulsion is destabilized by addition of an organic solvent. The catalyst suspension is then stirred, filtered, washed and calcined. By this method, the size of the produced nanoparticles is in the range of 20 – 40 nm with agglomeration. Another method is synthesizing the support simultaneously with the nanoparticles.¹⁵ The drawback of this method is that some of the metal particles become completely embedded in the supporting metal oxide, which reduces the available surface area of the active phase. The size of produced nanoparticles is in the range of 4.7 – 34.5 nm also with agglomeration. A third method is redispersion of nanoparticles in aqueous surfactant solution.¹³ The TEM images from the latter method showed some large Pt nanoparticles (10 – 80 nm) on the support with a high degree of agglomeration.

In this chapter, we introduce a novel and simple method to prepare highly active and stable supported Pt nanoparticles at room temperature, namely thermal-destabilization of microemulsion. The characteristic features of this method are firstly, the ability to design the size and the shape of nanoparticles and secondly, the ability to control the dispersion of designed nanoparticles on the support during the deposition process. The first feature is accomplished by choosing the appropriate surfactant, co-surfactant, reducing agent, and metal precursor with their proper concentrations. The second feature is achieved by adjusting the rate of heating, the choice of support material, and the mixing conditions to create a well mixed system. All substances can be chosen by conducting various test experiments as described in the Section Result and Discussion. Before depositing the nanoparticles on a support, the phase diagram of the microemulsion needs to be studied to determine the temperature range for the deposition (see upper right in Figure 4.2).

The strategy in the deposition process is to utilize the temperature path which changes the phase behavior of the microemulsions from 1-phase to 2-phases (bottom right in Figure 4.2). At the phase boundary (point b), the water droplets start to destabilize (the monolayer of surfactant molecules are broken). The opening of the droplets occurs simultaneously, the nanoparticles are released and directly deposited to the support material without agglomeration.

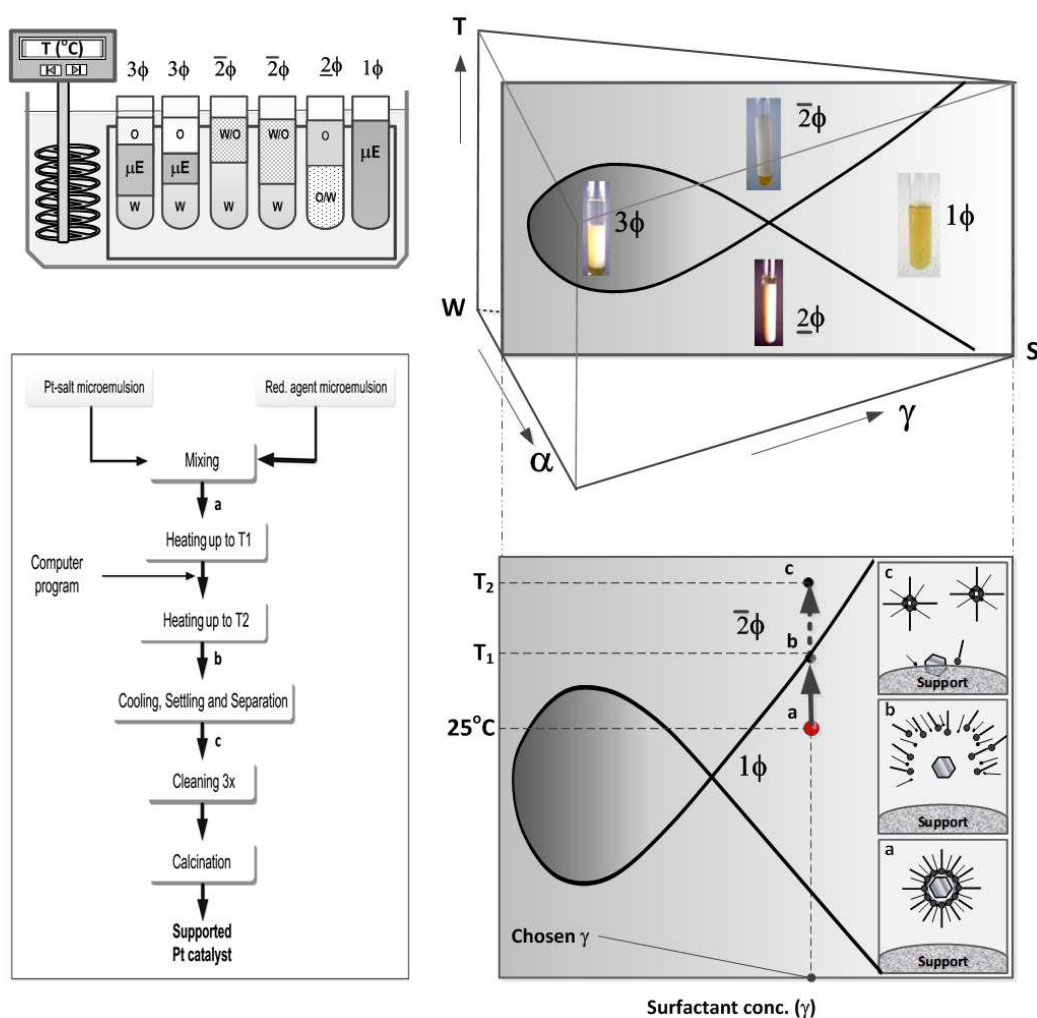


Figure 4.2 Principle of the deposition process for Pt nanoparticles via thermodestabilisation of μE : schematic phase prism (upper right), schematic experimental setup for phase behaviour observation (upper left), flowchart of synthesis (bottom left), and illustration of the deposition process.

This way, Pt particles can be evenly deposited on both the surface and the pores of the support material whilst preserving the size and the shape of the nanoparticles. By this method it is thus possible to produce small, multifaceted nanoparticles well dispersed on to support material (almost) without agglomeration.

The advantages of using this method are the following: (1) it does not need a protecting or capping agent either in producing multifaceted nanoparticles or in depositing them onto the support to prevent agglomeration, which other methods do¹⁶⁻¹⁹; (2) one can overcome the difficulty in controlling and terminating the growth during the initial stages, in order to obtain monodisperse size distribution²⁰, by stopping the reaction and putting the particles directly onto the support; (3) it is possible to reuse the surfactant and organic solvent, thus overcoming the hypothetical drawback that the μ E method employs a large amount of surfactant and organic solvent²¹; (4) by choosing the proper surfactant, the synthesis and deposition process can be carried out at a range from room temperature to an only little higher temperature, thus saving energy costs. To re-emphasize, not only is this synthesis method simple and inexpensive but also allows unrestricted control over the size and shape of nanoparticles as well as the dispersion on the support material.

4.2 Experimental Section

4.2.1 Materials

The chemicals used in the preparation of Pt nanoparticles were the following: Hexachloroplatinic acid hydrate (99.9%, Sigma Aldrich) as Platinum precursor, hydrazine monohydrate (98%, Sigma Aldrich) as reducing agent, Cyclohexane ($\geq 99.5\%$, Carl Roth) as oil phase and 1-pentanol ($\geq 98\%$, Carl Roth) as co-surfactant. The surfactants were the following: (1) non-ionic surfactants: 2-[4-(2,4,4-trimethylpentan-2-yl)phenoxy]ethanol (trade name: Triton X-100, $\sim 100\%$ purity, Sigma-Aldrich) and [2-[(2R,3S,4R)-3,4-dihydroxyoxolan-2-yl]-2-hydroxyethyl] (Z)-octadec-9-enoate (trade name: Span 80, $\sim 70\%$ purity, Sigma Aldrich); (2) anionic surfactant: sodium 1,4-bis(2-ethylhexoxy)-1,4-dioxobutane-2-sulfonate (trade name: AOT, 98% purity, Sigma Aldrich); (3) cationic surfactant: Cetyl trimethylammonium bromide (CTAB, $\sim 99\%$ purity, Sigma Aldrich). All the chemicals above were used without further purification.

Different kinds of support materials were used in deposition of the platinum nanocatalysts: γ -Al₂O₃ (Alfa Aesar and Sigma Aldrich), α -Al₂O₃ (Alfa Aesar), SiO₂ (Sigma Aldrich) and self prepared SBA-15 according to the method reported by Zhao et.al.²² All supports were pre-calcined before use. Acetone ($\geq 99.8\%$ purity, Carl Roth) as washing agent was used as received. The chemicals used for the hydrogenation reactions were methanol ($\geq 99.9\%$ purity, Carl Roth) as solvent and α -methyl styrene (99% purity, Sigma Aldrich) as reactant; both were used as received.

4.2.2 Catalyst Preparation

4.2.2.1 Phase Behaviour of Microemulsion Systems

Prior to synthesis of supported Pt nanoparticles, the phase diagram of the microemulsion needs to be established. In principle, we want to find a composition which can produce a microemulsion with small droplet size at room temperature, and also to select the proper temperature for the destabilization process.

The mass fraction of oil in oil and water mixtures is defined by α . The mass fraction of surfactant is determined by γ . Because we use a co-surfactant to stimulate rapid coalescence¹, surfactant is considered now as a pseudo single phase. Hence, $\gamma = (m_s + m_{co-s}) / (m_w + m_o + m_s + m_{co-s})$. The mass ratio of co-surfactant to surfactant is defined by δ . The molar ratio of water to surfactant indicating the size of water droplet is defined by ω . The complete phase behavior microemulsions is usually depicted by a ternary-phase diagram. It is constructed using the relative amounts the three components of microemulsions i.e. water phase, oil phase and surfactant. At constant pressure, the ternary phase diagram can be represented as a prism with the Gibbs triangle as the bottom part, and temperature (T) as the ordinate as shown in Figure 1 (upper right). The composition variables at each side of the Gibbs triangle are expressed with α and γ . It is rather complex and time consuming to construct such a phase prism diagram. Because we only want to focus on the phase evolution at different temperatures, it is not necessary to determine the entire coexistence region and phase boundaries within the Gibbs triangle. By observing the phase behavior of microemulsions (at fixed value of α and various (γ) at different temperature, a 'fish diagram' can be established, as shown in Figure 4.2 (right side). Experimentally, this diagram is constructed by

conducting an experiment as illustrated in Figure 1 (upper left). Test tubes were filled with microemulsions with different composition of surfactants ($\gamma = 0.025 - 0.85$) at the fixed value of α . The first trial is $\alpha = 0.5$ and the second is $\alpha = 0.92$. The latter α is chosen by rigorously conducted trial and error experiments, because we want to reduce more the water droplet size. The total volume was 7.5 ml. The test tubes were immersed in a thermostated-water glass bath. The phase behavior was observed by increasing the temperature every 5 °C (holding 15 minutes) from 10 °C to 70 °C. This procedure was applied for each different type of surfactant.

4.2.2.2 Synthesis of nanoparticles and deposition process.

The microemulsion system for preparing Pt nanoparticles comprises of the water phase either with hexachloroplatinic(IV) acid (H_2PtCl_6) or hydrazine, Triton X-100 as the surfactant, pentanol as co-surfactant and cyclohexane as the oil phase. The compositions used in the experiments are listed in Table 4.1, except for the experiment where the concentration was varied. The synthesis of the platinum nanoparticles was carried out in a 200 ml double-wall glass reactor equipped with a three parallel two-blade impeller. The hydrazine microemulsion was added slowly to the reactor, which had already been filled with the Pt salt microemulsion, by a micro pump (0.2 ml/s). The mixture was stirred at 700 rpm for 30 minutes at room temperature to form colloidal stabilized Pt nanoparticles.

Table 4.1 The composition of microemulsions used in the experiments

	Microemulsion I	Microemulsion II	%wt	
			$\omega_1 = 13$ ($\alpha_1 = 0.92, \gamma_1 = 0.3$)	$\omega_2 = 15$ ($\alpha_2 = 0.5, \gamma_2 = 0.7$)
Water phase	2.55 mM H_2PtCl_6	18.35 mM Hydrazine	5.6	15
Oil phase	Cyclohexane	Cyclohexane	64.4	15
Co-surfactant	Pentanol	Pentanol	15	35
Surfactant	Triton X-100	Triton X-100	15	35

Then the pre-calcined support (500 °C for 2 hours) was added to the mixture, and the Pt nanoparticles were deposited on the support material by heating up the microemulsion to the destabilization temperature. To reach the destabilization

temperature, different heating rates were used. (The temperature of the reactor system was adjusted by a thermostat, which was connected to computer program to regulate the heating rate). After the deposition process, the mixture was cooled down. After all the supported catalysts precipitated, they were carefully separated from the solution and washed three times with pure acetone and subsequently calcined. The flowchart of this synthesis method is presented in Figure 4.2 (bottom left).

4.2.2.3. Activity testing in hydrogenation reaction

To ensure the accuracy of activity testing, all catalysts were kept away from contact with air. We tested the catalysts in the hydrogenation of α -methyl styrene (AMS) at 20 °C and 1.1 bar. The hydrogenations were performed in a 200 ml double-walled glass reactor equipped with glass baffles and a gas-dispersion stirrer. The scheme of the hydrogenation reactor set-up is presented by Milano et.al.²³ Hydrogen and nitrogen gas lines were attached to the reactor. A vacuum pump was attached to evacuate the reactor. The reactor system was connected to a pressure controller (to keep the pressure constant) and a flow meter (to measure the hydrogen required to replace the amount of hydrogen consumed by the reaction). Both were connected to a computer with a control program.

The supported platinum catalyst was added to the reactor, subsequently with adding 100 ml methanol as solvent and 1 g AMS, respectively. The reactor was closed and sealed followed by the reduction of pressure down to 0.2 bar (and holding it for 5 minutes in order to check for a gas leakage). Having ensured that there was no leakage, the mixture was stirred at 600 rpm and 20 °C for 20 minutes. The reactor was evacuated three times, by reducing the pressure to 180 mbar, and then refilled with nitrogen. Afterward the reactor was evacuated to 180 mbar and filled with hydrogen until it reached a total pressure of 1.1 bar. The computer program was started along with the stirring up the mixture at 1200 rpm. The reaction was stopped when the data acquisition indicated that there was no further hydrogen consumed in the reaction. A representative reaction profile is presented in the Figure 4.3. Based on the fact that one molecule hydrogen is needed per one double bond of AMS ($n_{\text{product}} = n_{\text{H}_2}$), the moles of product can be calculated by the moles of consumed hydrogen. The rate of product formation is calculated from eq. (4.1), based on the ideal gas law, using the rate of hydrogen consumption which was measured by the flow meter.

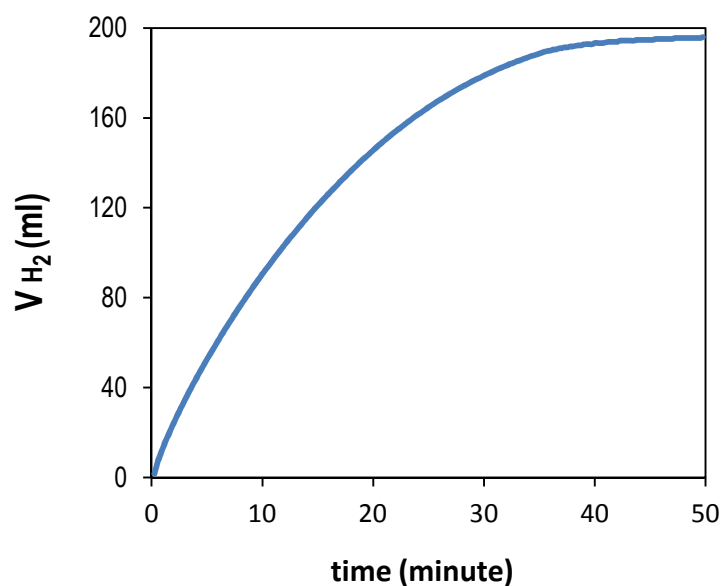


Figure 4.3 A representative profile of α -methyl styrene (AMS) hydrogenation with 0.01 wt% Pt/Al₂O₃ at 20°C and 1 bar

$$\frac{dn_{\text{product}}}{dt} = \frac{P}{RT} \frac{dV(\text{H}_2)}{dt} \quad (4.1)$$

By dividing the value of dn_{product}/dt by the amount of Pt metal on the support (analyzed by ICP), we get the value of activity as shown in eq.(4.2).

$$\text{Activity } (\mu\text{mol} \cdot \text{g}_{\text{Pt}}^{-1} \cdot \text{s}^{-1}) = \frac{dn_{\text{product}}}{dt \cdot m_{\text{Pt}}} \quad (4.2)$$

Therefore, to measure the performance of the catalyst we use Activity instead of TOF because we assume all the metal atoms deposited on the support are surface active. In all of our catalytic testing experiments, the reaction rates were compared at the same reaction conditions. A few repeated experiments show that the reproducibility of the rate was found to be less than 5 % error.

4.2.2.4 Characterization and Analysis Methods

The shape, size, and lattice structure of the Pt nanoparticles were investigated by transmission electron microscope (TEM) at an FEI Titan 80-300 (sub-Angstrom resolution, able to investigate at atomic scale), and also with FEI Tecnai G2 S-Twin TEM and Philips CM200/FEG high-resolution TEM (HRTEM) operated at 200 kV. Both microscopes are equipped with an energy dispersive x-ray detector (EDX). The TEM grids were prepared for imaging by placing a small drop of the specimen solution on a copper grid having an amorphous carbon film less than 20 nm thick and allowing it to dry completely in air at ambient temperature. Pt content of the support catalysts were analyzed by ICP-OES Element 2 (Varian) at low resolution (sample gas 0.863 L/min; plasma power 1350 W).

4.3 Results and discussion

To obtain stable and active supported Pt catalysts, optimal conditions for synthesis and deposition have to be found. In this section, the impact of the most important parameters will be discussed by comparing the catalytic activity in the hydrogenation of AMS. This discussion is supported by a detailed analysis of the catalyst structure by conventional methods.

4.3.1 Choosing the surfactant and co-surfactant

It has been shown by various studies that the choice of surfactant is critical to the size, shape and stability of the prepared particles.²⁴ The rigidity of the surfactant film plays a crucial role in guiding the morphology of the product formed.²⁵ In our work, we consider not only those factors, but also the surfactant's ability to produce a one-phase microemulsion at room temperature and the temperature range of destabilization. The phase diagrams of microemulsions containing different surfactants are shown in Figure 4.4.

By considering that system formulated with ionic surfactants (Figure 4.4 c and d) cannot produce one-phase regions at room temperature and Span 80-containing microemulsions change their phase around room temperature (Figure 4.4 b), we

decided to choose Triton X-100 as surfactant (Figure 4.4 a) for further experiments. To ensure that the shape of nanoparticles is only controlled by the surfactant, the influence of other parameters must be annulled. This is achieved by adding the co-surfactant and choosing a solvent that can promote a fast growth rate of nanoparticles in the water droplets. We decided to use pentanol as a co-surfactant because it not only caused rapid microemulsion formation, but also rapid coalescence.²⁶

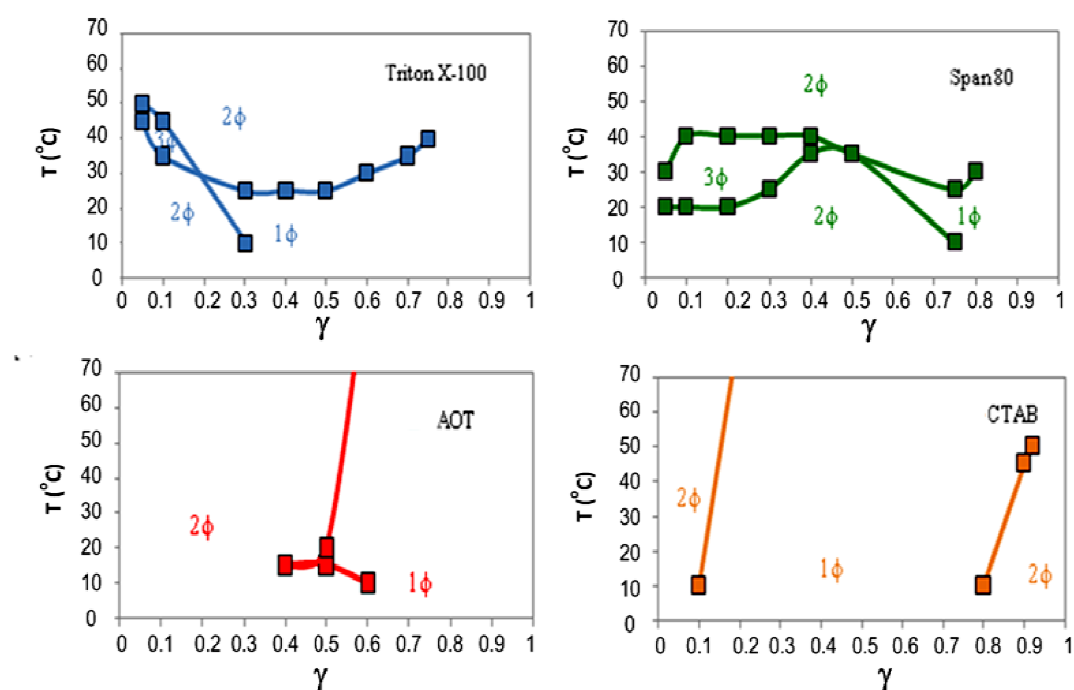


Figure 4.4 Phase diagrams of microemulsions with equal amounts of oil and water ($\alpha = 0.5$) as a function of surfactant concentration (γ) and temperature (T) for four different surfactants.

4.3.2 Choosing the solvent

The solvent can affect the hydrodynamic radius and thickness of the surfactant layer of the micelles. The more bulky the structure of the solvent (larger molecular volume), the more rigid is the surfactant curvature and the slower the droplet exchange will be. In our research, we chose a less bulky solvent cyclohexane, because it is able to penetrate the surfactant tails efficiently during droplet exchange.²⁵ As a result, the growth rate of nanoparticles is faster, thus ensuring that the size and the shape of produced nanoparticles is affected only by the surfactant. In case another hydrocarbon

is selected as solvent, a suitable nonionic surfactant has to be chosen according to the well known relations in the phase behavior of water-oil-surfactant systems.

4.3.3 Choosing the precursor

In this study, we chose a strong reducing agent N_2H_4 to ensure a fast reduction process in the nucleation process so that the shape in the formation of Pt crystal is controlled only by surfactant. However, we had no particular reason in choosing H_2PtCl_6 as the Pt precursor, although in our recent study we found that using K_2PtCl_4 as the Pt precursor results in different shape of Pt particle.

4.3.4 The effect of the heating rate

The critical step of preparing the supported catalyst by thermo-destabilization of μE method is the heating process. The mixing of both microemulsions containing hexachloroplatinic acid and hydrazine was performed at room temperature. The produced nanoparticles were released from the water pools by increasing the temperature of the mixture. In this work, we tested two different ways of heating up the mixture to release the nanoparticles. The first way is to increase the temperature with a constant rate (1, 0.25 or 0.067 °C/min) and the second way is to increase the temperature stepwise (1°C/15 min). The catalyst prepared at the fastest heating rate has the highest activity (Figure 4.5).

The explanation for this event is related to the residence time of unprotected nanoparticles in the microemulsions. The faster the heating rate, the faster is the opening of the droplets and the shorter they stay freely in the destabilized microemulsions. As a result, the tendency of the particles to agglomerate is reduced, thus they are more active. By observing this, we chose the fastest heating rate (according to our thermostat capacity) to destabilize the microemulsions.

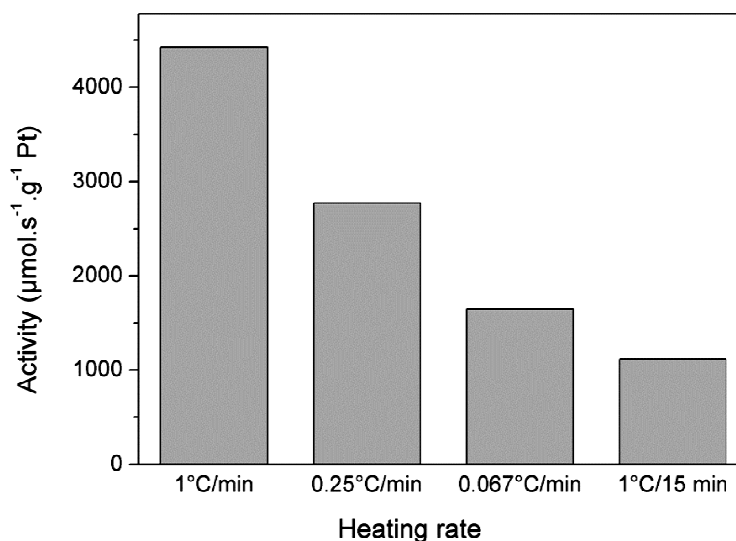


Figure 4.5 The activities of the produced catalysts prepared in different heating rates

4.3.5 Effect of the support feeding prior to deposition process

To optimize the deposition process, we tested the method of feeding the support into the reactor prior to deposition process, i.e. before or after the opening of the water droplets. We observed that the catalyst prepared by feeding the support into the reactor after opening the droplets was less active (Figure 4.6). Undoubtedly, feeding the support into the reactor after opening the droplets allows the particles to agglomerate before their contact with the support. This strongly confirms the result from Figure 4.5 that the nanoparticles tend to agglomerate if they are not immediately deposited and stabilized on the support. In all further experiments we fed the support into the reactor before opening the droplets.

4.3.6 Effect of the growing time

The most interesting part of our method is that we can produce a catalyst according to the desired particle growth by stopping the reaction and immediately putting the particles on the support. This growth interruption may result in nanoparticles with smaller diameter. In this method, this aspect can be further developed because many authors have found that the shape and size of Pt nanoparticles change during the growing time.^{1,25,26,27} The growth mechanism during the course of reaction in microemulsions has been proposed by some groups.^{20,27}

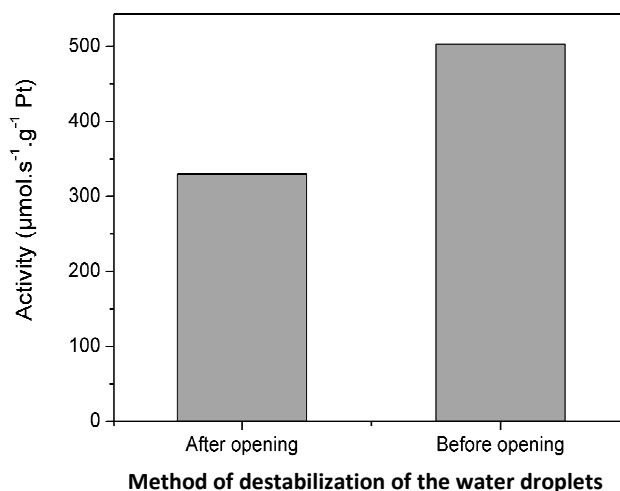
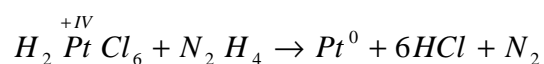


Figure 4.6 The activities of the Pt-catalysts prepared in different support feeding prior to deposition process

The stages of nucleation and growth which are related to controlling the size and shape of Pt nanocrystals has been well illustrated by Tsung et.al.²⁸ It also has been reported that nearly monodisperse size distribution can be obtained at the stage of nucleation and growth either by stopping the reaction or by supplying a reactant source to maintain a saturated condition during the course of the reaction.²⁰ The formation of Pt particles starts when Pt^{+4} ions come in contact with the reducing agent N_2H_4 , through interdroplet exchange or coalescence, according to the following reaction:



We observed that the activity of the catalyst depends on the size of the particles (Figure 4.7). From the TEM image in Figure 4.7a, one can see that there are only few atoms grouped in nanoparticles after 1 minute. The activity of this catalyst is low because few active sites are available to promote the surface reaction. It seems that the status of these particles has passed the nucleation stage and is already in crystal growth (see Figure 4.2). The activity of the catalyst produced in 15 minutes is lower than that produced within 1 minute. Figure 4.7b implies that although many particles are formed, they are probably in the transition process of agglomeration and ripening to form a defined crystal structure. Therefore, in the deposition process, they presumably spread

over the support material but only form two dimensional structure which has less active sites. Compared to the particles obtained after 15 minutes, after 30 minutes, a three dimensional (3D) crystal structure has been formed characterized by a clear 2D hexagonal shape (Figure 4.7c).

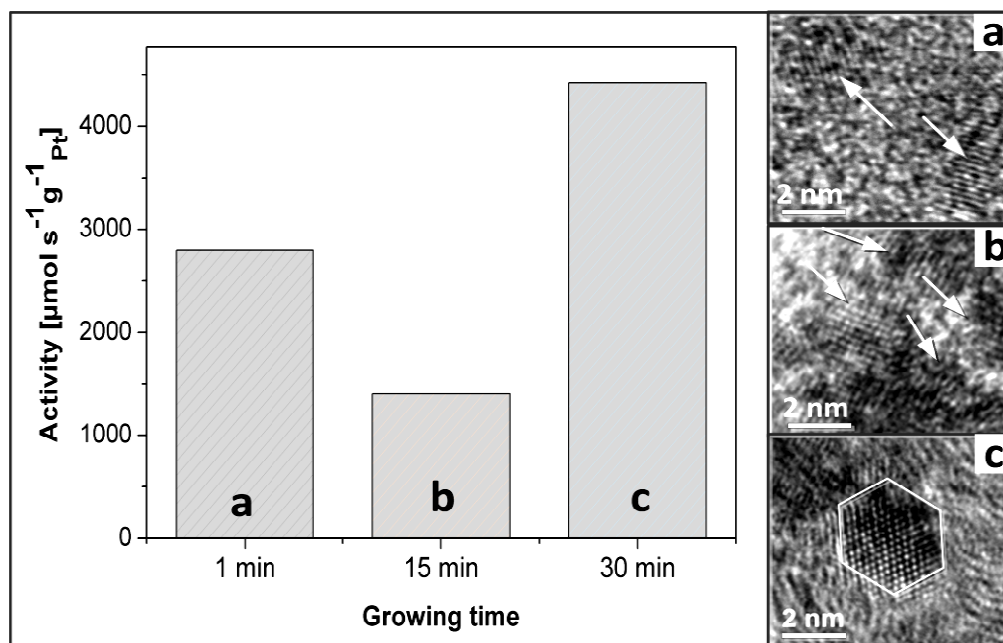
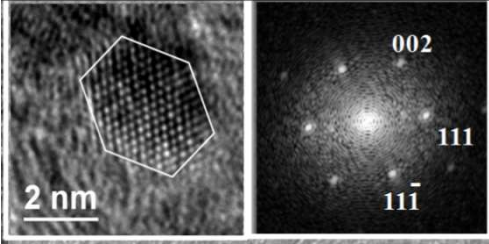
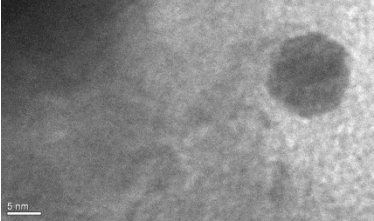
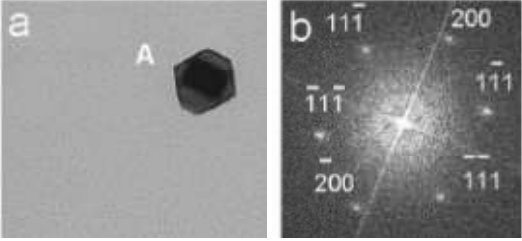
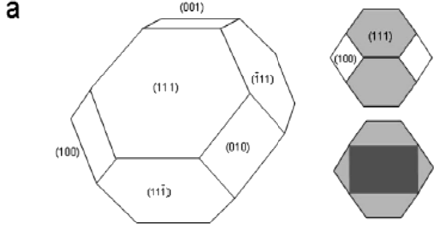
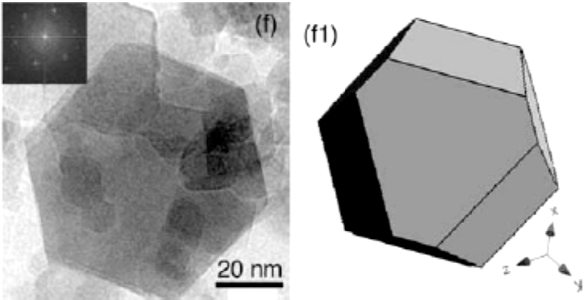


Figure 4.7 The activities of the produced catalysts prepared in different growing times and the corresponding TEM images: a,b,c are the Pt particles after growing 1 min, 15 min and 30 min respectively.

The hexagonal structure can be predicted to a truncated octahedral based on the Wulff construction.²⁹ In the TEM investigations, the Pt nanoparticles in the water phase were moving when they were irradiated by the electron beam in TEM, therefore the high-resolution TEM images are not very clear. But based on the similarity of our TEM images and the Fast Fourier Transform pattern with the results from other publications²⁹⁻³² (Table 4.2) which said it is a truncated octahedral, we would like to conclude that our particle is also truncated octahedral. This multifaceted crystal has atomic steps and terraces which can enhance the activity of catalyst;³¹ hence, the particles which grow for 30 minutes show higher activity.

Table 4.2 Comparison of our TEM images and FFT of other results

Our results	Other results
 	  <p>(Ferreira et.al.)</p>  <p>(Swaminathan et.al)</p>

The nuclei may grow by reducing the Pt^{4+} ions, mainly on the most catalytically active $\{111\}$ surfaces, to form truncated octahedron nanoparticles.³³ This well defined crystal shape has more faces and causes the higher concentration of atomic step edges that are readily available to participate in chemical reactions. It is most likely that after 30 minutes particles have already reached a stable size, wherein they will grow by combining with small unstable nuclei and not by collisions with other stable particles.²⁰

4.3.7 The effect of the initial concentration ratio

In designing the nanoparticles inside of the water droplets, as it has been studied,³⁴ the initial concentrations of the precursor and reducing agent also need to be considered. It has been reported that with increasing the concentration of hydrazine while the concentration of metal salt is kept constant, a decrease in particle size is observed.⁹ In vice versa, increasing the concentration of the metal precursor while the concentration of hydrazine is kept constant can also increase the particle size.³⁵ We observed that the highest activity was achieved by the catalyst produced with an 100 fold excess of reducing agent (Figure 4.8). This indicates that the more complete (without Pt^{4+} left in the solution) and faster the precipitation of nanoparticles facilitated by giving excess reducing agent, the more active is the catalyst. This is in agreement with the results reported by Niesz et.al.³⁶ which show that faster reduction of Pt ions leads to small particles.

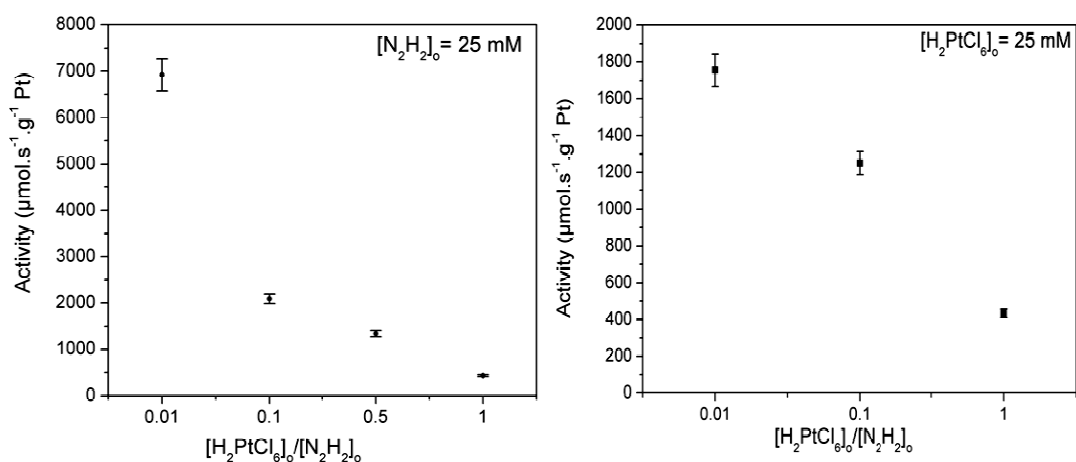


Figure 4.8 Activities of the Pt-catalysts prepared with different ratios of initial concentrations

4.3.8 The deposition process by thermal-destabilization method

The phase diagrams which show the temperature range of particle deposition from microemulsions with $\alpha_1 = 0.5$ and $\alpha_2 = 0.92$ are depicted in Figure 4.9. Decreasing the water content in microemulsions causes a shift of the phase boundary to higher temperatures and thus to a larger range of deposition temperature. It indicates that the bigger size of the water droplets (which is caused by the higher proportion of water), needs a bigger amount of energy to destabilize. By increasing the temperature of the microemulsion system (tracking the arrow in Figure 4.9) the transfer of Pt nanoparticles from inside of the water droplets onto the support was successfully done with almost no agglomeration, which is verified by the results in Figure 4.10.

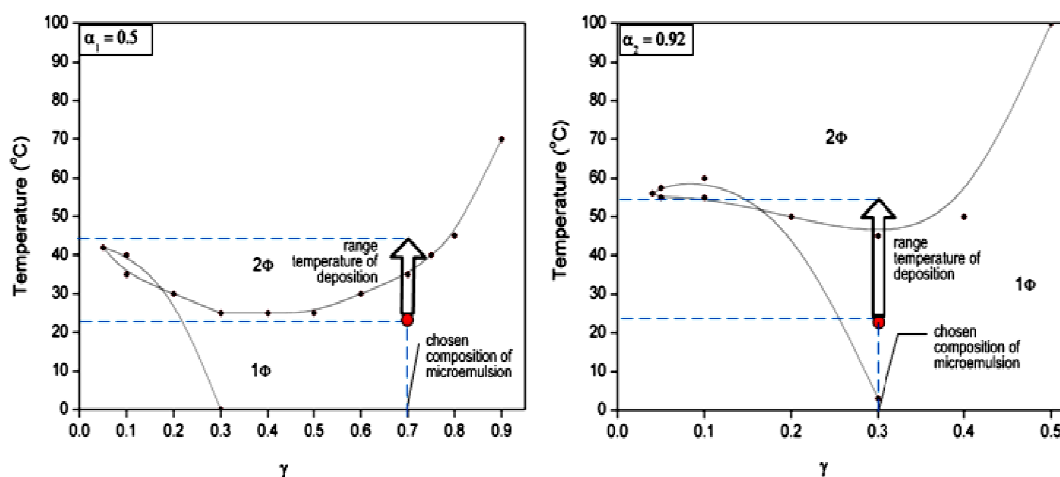


Figure 4.9 Phase diagrams of microemulsions and the ranges of temperature of deposition, $\alpha_1 = 0.5$ (left) and $\alpha_2 = 0.92$ (right).

The droplet size is an important parameter because it controls the size of the produced nanoparticle and thus influences the activity of the catalyst. Experimentally, it is measured by Dynamic Light Scattering (DLS). However, we did not measure it directly because according to several studies it is dominantly characterized by the $[\text{H}_2\text{O}]/[\text{Surfactant}]$ molar ratio, defined as ω .^{24,37} There is no general formulation that correlates ω , size of droplets and size of the nanoparticles, because every microemulsion has its own characteristic. However, it can be generalized that the droplet size is proportional to ω . Major changes of the particle size are obtained at low ω .²⁰ We study the influence of ω on the size of the produced nanoparticles by TEM. The TEM pictures in Figure 4.10 indicate that the size particles produced in $\omega_1 = 13$ is

significantly smaller than in $\omega_2 = 15$. This is in agreement with the results that have been published which show a larger size of the particle for higher values of ω .^{25,38,39} The corresponding histograms in Figure 4.10 show that the size distributions of nanoparticles produced at both ω are rather narrow and exhibit the features of a log-normal distribution. It has been reported that the uniformity of the size distribution is achieved through a short nucleation period and this can be achieved by feeding a reactant continuously to keep saturated conditions during the course of the reaction constant.²⁰ This indicates that in both cases, the amount of reducing agent (8 fold excess) is enough to promote a short nucleation step.

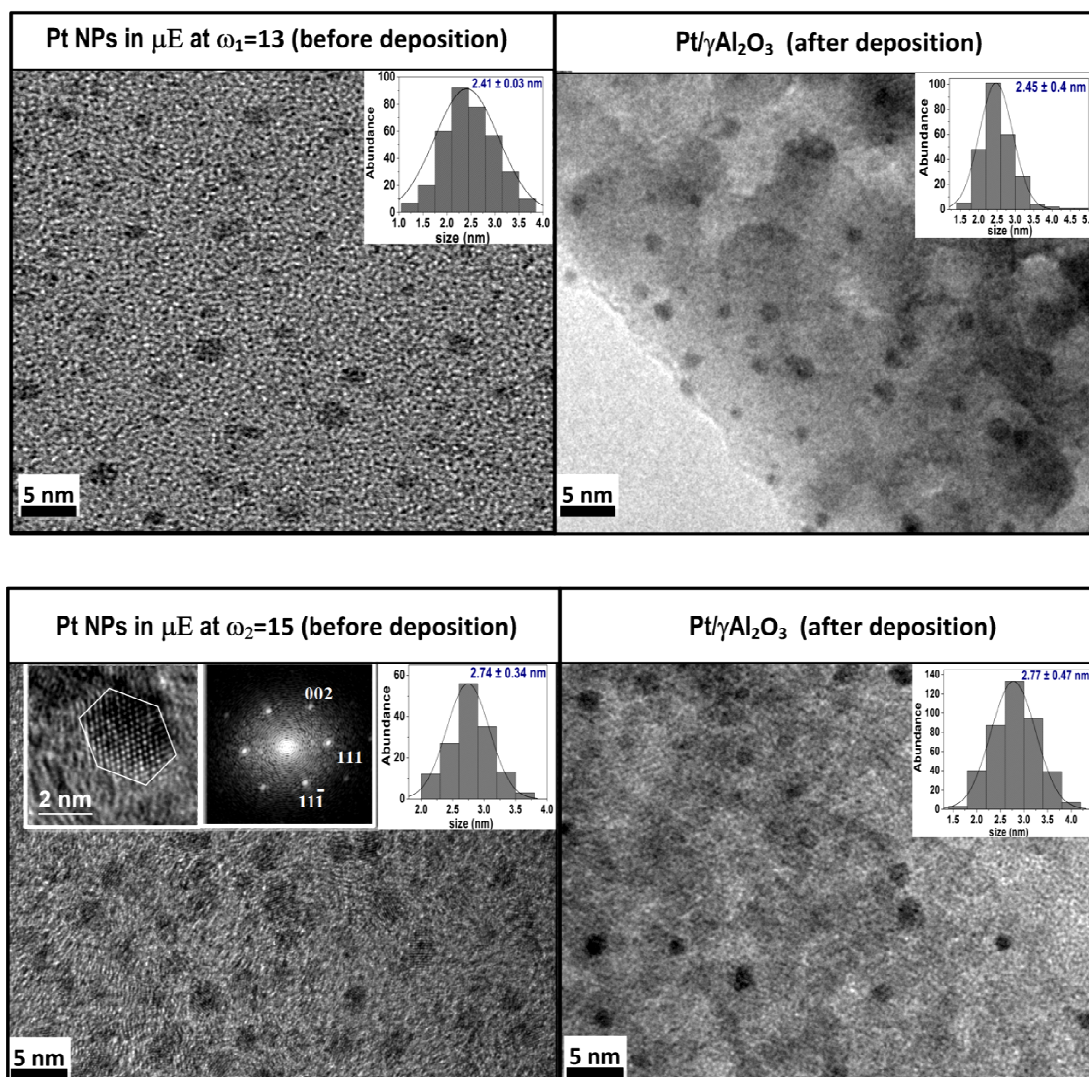


Figure 4.10 TEM images of Pt nanoparticles inside of the microemulsions before and after deposition process at different ω and their corresponding size distributions.

The primary factors for the higher activity of supported Pt catalysts produced from our experiments are the size, the shape and the dispersion. It is most likely that the small size of the Pt particles is caused by the effect of the reducing agent. The reduction process by hydrazine can be completed instantly, in comparison to the use of pure hydrogen which is a much slower process.⁹ As a general rule, a fast nucleation process will result in the production of small particles. The small size can also be contributed to the presence of the co-surfactant, pentanol. It was concluded by Eastoe et.al.²⁴ that the addition of a co-surfactant not only leads to a higher fluidity of the interfacial film, thus increasing the rate of interdroplet exchange, but also leads to a higher curvature of the droplets, so smaller particles are obtained.

The hexagonal shape of the particles (inset A Figure 4.10) is produced primarily because of the head group of the surfactant rather than the reducing agent. As mentioned previously, in synthesis by microemulsions method, the shape of the nanoparticles is strongly influenced by surfactant.²⁵ On the other hand, reducing agent can also affect the shape of the produced nanoparticles. A weak reducing agent effectively isolates the nucleation and growth events allowing control over the size and shape.⁴⁰ In case of using strong reducing agent like hydrazine, the dominant factor will be taken by surfactant. We use a strong reducing agent, hydrazine, with 8 fold excess in our synthesis to ensure a fast growth; hence there is no influence in governing the shape of nanoparticles. It has been reported that the use of Triton X-100 as surfactant to different kind of metal precursor can produce nanoparticles with different shapes such as spherical, nanofibers, nanobelts, rodlike⁴¹ and nanocubes³⁸. Therefore, when using H_2PtCl_6 as a precursor, Triton X-100 is dominantly directing the seed to the equal growth of $\{111\}$ and $\{100\}$ facets which finally form truncated octahedrals which look hexagonal in TEM image⁴² (inset A Figure 4.10). As mentioned above, not only from the Wulff construction do we predict that our nanoparticles are truncated octahedrals, but also from the similarities to other results as shown in Tabel 4.2. This is also supported by the Fourier Transform pattern of the particle (inset B Figure 4.10), which shows the same pattern with what has been reported to be a truncated octahedron.²⁹ The equal or isotropic growth produced by nonionic surfactants like Triton X-100 was also proposed in earlier studies.^{38,41}

It has been stated that nanoparticles are small and not thermodynamically stable against crystal growth. To finally produce stable nanoparticles, these nanoparticles

must be arrested during the reaction by adding surface protective reagents, such as organic ligands or inorganic capping materials.²⁰ Interestingly, by the thermodestabilization of microemulsion we can produce supported Pt particles with a narrow size distribution without a protective or capping agent. Table 4.3 presents different methods to prepare supported Pt particles.

Table 4.3 The comparison between different methods of Pt-nanoparticles preparation

Method	Author	Capping Agent	Insitu-Support+NP preparation	Result/Particle size
Impregnation	El. Shayed. ⁴⁴	Yes	No	Ave. 10 nm
Impregnation	Lee et.al. ⁸	Yes	No	5 – 7 nm
Precipitation	Lee et.al. ⁸	Yes	Yes	Failed/Agglomeration
Sol-gel	Lee et.al. ⁸	Yes	Yes	>50% of the pore structure shrunk
Polyalcohol reduction	Liu et.al. ⁴⁵	Yes	Yes	3.5– 11.5 nm
Hydrolysis in μ E	Ikeda et.al. ¹⁵	Yes	Yes	4.7– 34.5 nm
Rotating cathode	Zhou et.al. ³³	Yes	Yes	6 – 12 nm
Langmuir-Blodgett	Rioux et.al. ⁴⁶	Yes	Yes	9 – 10 nm
Electrophoretic	Teranischi et.al. ⁴⁷	Yes	No	30 – 32.5 nm
Rampino and Nord	Petroski et.al. ⁴⁸	Yes	Yes	Ave. 12 nm
Rampino and Nord	Erikson et.al. ⁹	Yes	Yes	8 – 12 nm
Solvent Destabilization	Boutonnet ⁴⁹	No	No	10 – 35 nm/ Agglomeration
Solvent Destabilization	Yashima et.al. ¹⁴	No	No	20 – 40 nm/ Agglomeration
Solvent Destabilization	Hanna et.al. ¹³	No	No	5 – 100 nm/ Agglomeration
Redispersion	Hanna et.al. ¹³	No	No	10 – 50/ Agglomeration
Insitu hydrolysis and condensation in μ E	Bae et.al. ³⁹	No	No	20 – 42 nm

Some researchers applied different deposition methods of particles from microemulsions such as by solvent destabilization or redispersion (Boutonnet, Yashima, and Hanna et.al.) but still big particles and agglomerates are produced with broad particle size distributions. Many have used capping agents in microemulsion system yet still produced rather big particles and broad particle size distributions such as the results of Liu et.al. and Ikeda et.al. Bigger Pt particles are also produced from other methods such as impregnation, precipitation, sol-gel, rotating cathode, Langmuir-Blodgett, and Rampino and Nord, although they used capping agents.

4.3.9 Effect of the support material and comparison with other catalysts

In our synthesis we observe that the dispersion of particles on the support also depends on the properties of the support. The extreme difference in the obtained activity of catalysts supported on SBA-15 and Al_2O_3 indicates that in the thermo-destabilization method, the properties of the support material are crucial. It determines the responsiveness of the support to the nanoparticles released from the droplets during the deposition process. It is most likely that not only the high surface area of SBA-15 ($800 \text{ m}^2/\text{g}$) which accommodates the releasing of particles, but also the structure of the support are responsible to the activity. The well ordered channel structure of SBA-15 provides a good dispersion of the active phase on the surface; it can hinder Pt nanoparticles from sintering and thus promote the good contact between active sites and reactants. The TEM image in Figure 6A shows that Pt nanoparticles distributed not only on the surface of SBA-15 particles but also inside of the channels (see the inset). To confirm the location of the nanoparticles on the support material, we investigated the cross section of our Pt catalyst with EDX as shown in Figure 4.11. The red line refers to the amount of Pt on the outer surface of the support while the blue line to the inner surface of the support. A little difference in height between blue line and the red line shows that to such an extent Pt also located inside of support. This also indicates that Pt metals are able to penetrate into the pores of the support during the deposition.

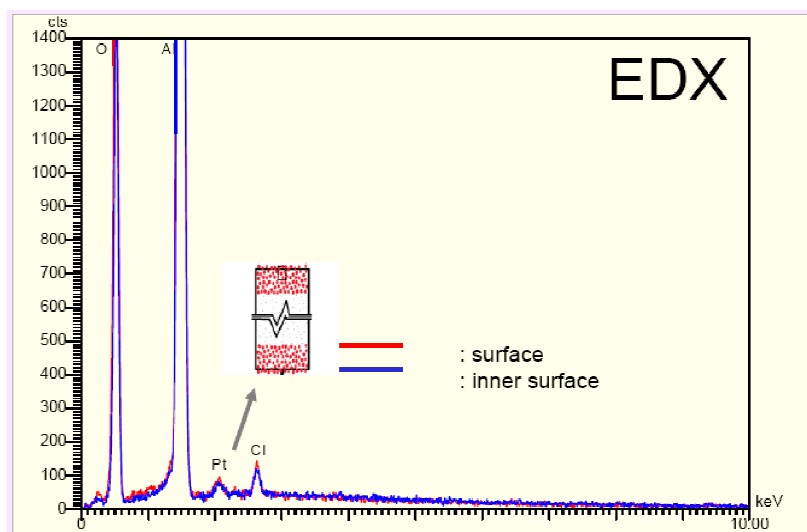


Figure 4.11 EDX analysis of one sample of the produced supported Pt catalysts which shows the location Pt-metal on the surface of the Al_2O_3

We have tried to verify the level of dispersion of our catalysts with the Chemisorptions method. Unfortunately, it was not successful because of the low loading of metal ($\pm 0.07\%$) and the small size of the Pt particles (± 2.5 nm). We did prepare low loadings of the metal purposely (by using a low concentration Pt salt) because we want to produce the small size of NPs and also to keep them from agglomeration during the deposition process. For that reason, we analyzed the dispersion of the catalyst only by observing the TEM pictures which show that our catalysts are well distributed over the support materials. The particle size distributions are also narrow as shown in the Figures 4.10. We also compare our produced catalysts with other Pt catalysts, i.e commercial ones and the one prepared by another method. To make sure that the catalysts are fully reduced, the commercial catalysts were pre-reduced with hydrogen at $300\text{ }^\circ\text{C}$ for 3 hours before being tested. The activities of Pt/SBA-15 and Pt/ Al_2O_3 are 55000 and $7000\text{ }\mu\text{mol}/(\text{g}_{\text{Pt}\cdot\text{s}})$ respectively while the commercial catalysts Pt/ Al_2O_3 and Pt/C are 4000 and $3000\text{ }\mu\text{mol}/(\text{g}_{\text{Pt}\cdot\text{s}})$ as shown in the Figure 4.12.

4.3.10 Effect of calcinations

Calcination of supported catalyst needs to be optimized in order to avoid sintering. Figure 4.13 shows the catalytic activity of catalysts prepared at different calcination temperatures (each temperature was held for two hours). It can be concluded that by

increasing the temperature up to 500 °C, Pt nanoparticles start to sinter on the support indicated by a decreased activity. This can be seen from the corresponding TEM images which show the increasing size of the particles (Figure 4.13 b and c). Our observations are comparable to what has been published: Romero-Pascual et.al⁵⁰ reported that sintering platinum particles on alumina support happened after calcinations at 500 °C for 2 h and at 600 °C for 24 h, and Miller et. al⁵¹ showed that after 300 °C the dispersion of Platinum on the support decreased drastically.

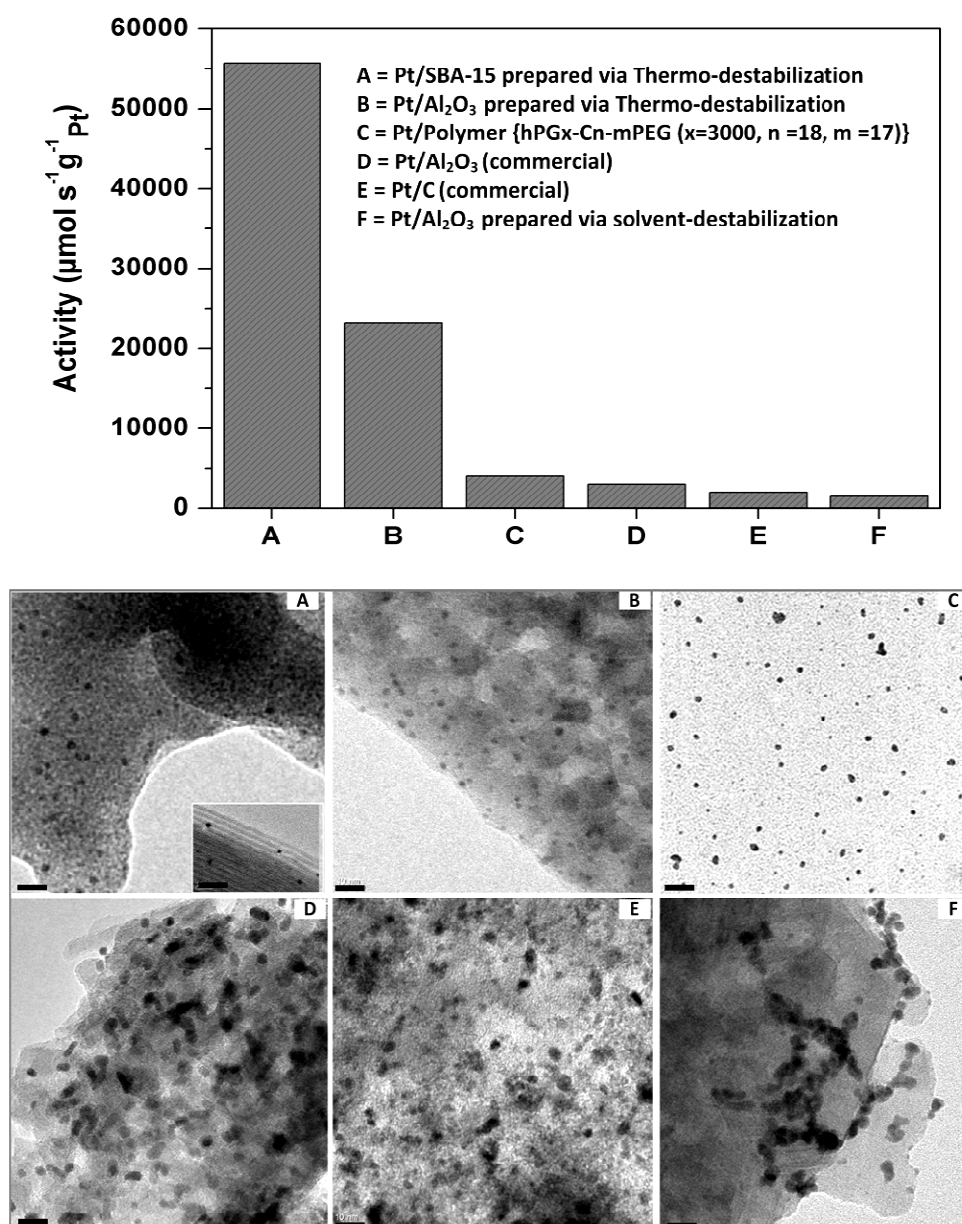


Figure 4.12 The activities of the Pt catalysts (upper) and the corresponding TEM-images (bottom). The scale bars are 10 nm.

Therefore, we conclude that the air calcination at 300 °C for 2 hours was sufficient to ensure the removal of the remaining surfactant from the synthesis process and to strengthen the bond of Pt to the support. This is confirmed by the stability test in Figure 4.13.

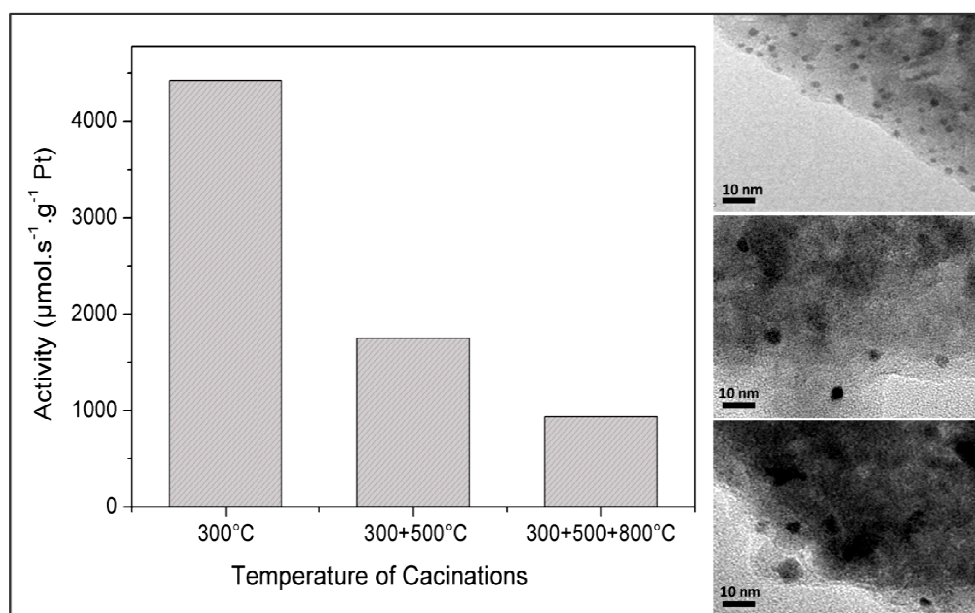


Figure 4.13 The activities of the Pt catalysts prepared in different temperature of calcinations and the corresponding TEM images. Each calcinations temperature was held for 2 h

4.3.11 Other Parameters

We also investigated other parameters such as filling rate of reducing agent into the reactor, stirring rate during synthesis and deposition process, use of baffles in the synthesis reactor, kind of washing agent to clean the catalyst after synthesis, but according to our observations, these variables have minor effects.

4.3.12 Stability test

To test the life time of our catalyst, we employed our Pt/ $\gamma\text{-Al}_2\text{O}_3$ in six consecutive hydrogenation reactions. We note that for the stability testing, we did not use Pt/SBA-15 (the best activity), because we synthesized it long after the stability test of the Pt/ $\gamma\text{-Al}_2\text{O}_3$, which has the highest reaction rate. We assume that the Pt/ $\gamma\text{-Al}_2\text{O}_3$ is

a representative catalyst for showing the ability of our method in producing a stable supported catalyst. Figure 4.14 displays the stability performance of the catalyst in hydrogenation of AMS. By comparing the initial reaction rate (indicating the activity of the catalyst) only a slight decrease (in the range of error) from the first run to the sixth run is observed; therefore, the catalyst is considered to be stable. This could lead to a conclusion that there is no significant change of the size and shape of Pt catalyst during the reactions. The corresponding TEM pictures also confirm that there is no significant change in the size of platinum nanoparticles during the reactions. However, Figure 4.12 indicates that the size and the shape of nanoparticles might change in higher temperature reactions. This could be anticipated by using mesoporous materials and hollow cages to provide restricted microenvironments for supporting the catalyst (An et.al). We would like to conclude that Pt catalyst supported on non-mesoporous Al_2O_3 is more suitable for reaction at low to the middle high temperature ($< 300\text{ }^\circ\text{C}$).

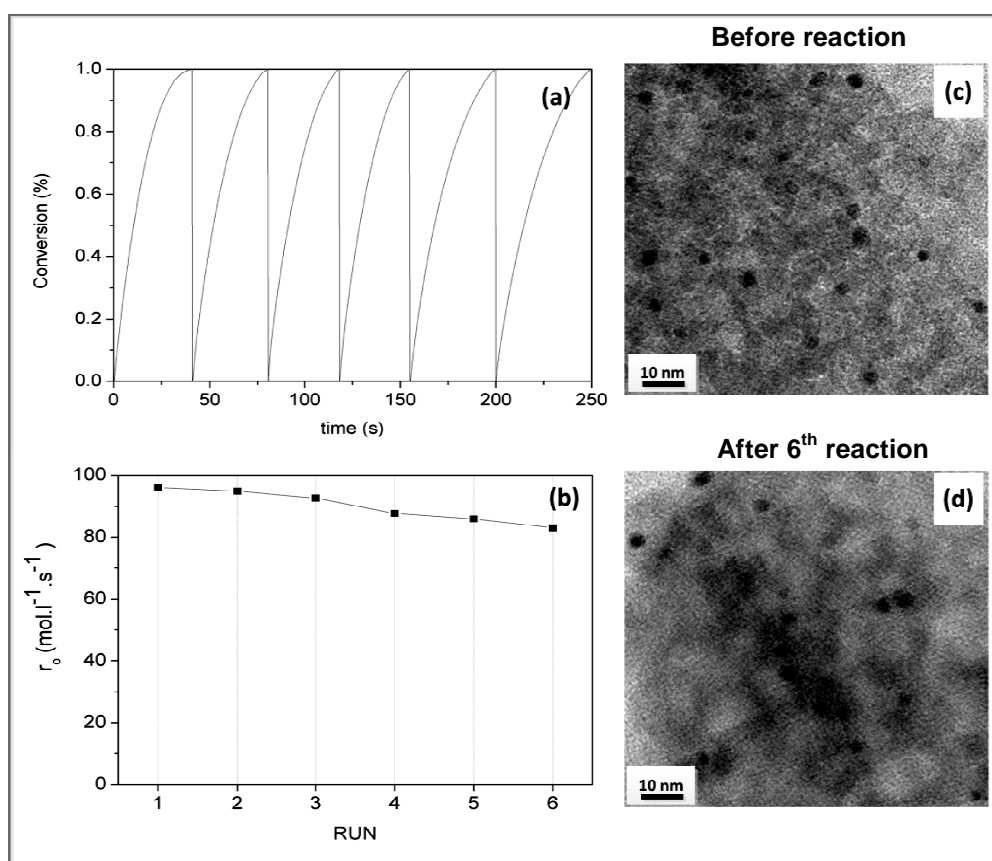


Figure 4.14 Six hydrogenation runs of 1 g of AMS: (a) conversion vs time, (b) initial reaction rate of each hydrogenation run, (c) and (d) TEM images of synthesized 0.1% Pt@ γ - Al_2O_3 before and after the hydrogenation reactions

4.4 Conclusion

We have developed a new, simple yet excellent method to synthesize highly active and stable supported Pt catalysts via the so-called thermo-destabilization of microemulsions. In this study, we fixed the type of surfactant (Triton X-100), co-surfactant (pentanol), solvent (cyclohexane), metal precursor (H_2PtCl_6), and reducing agent (hydrazine). The parameters that significantly influence the activity of the produced catalysts are the heating rate during the thermo-destabilization process, the molar ratio of water to surfactant (ω), the initial molar ratio of metal to reducing agent, the growing time, the type of support material, and the calcination temperature.

The produced catalysts exhibit higher catalytic activities than those prepared via conventional methods. We attribute this to the small size, multifaceted shape, narrow size distribution and good dispersion of the nanoparticles on surfaces of the support material. The insignificant difference of activity ($< 1\%$) of produced catalyst from different batches indicates that this method is adaptable to reproduce. Comparative studies in applying our method to synthesize other supported metals such as Ag, Pd, Ru, on different kinds of material supports is still under way to elucidate if the recipe can be generalized. We found that our method also works well with those metals, and we intend to publish these results later. Although we have found good results, we are still continuing to improve and optimize the performance of the catalyst.

References

- (1) Narayanan, R.; El-Sayed, M. A. *J. Phys. Chem. B* 2005, 109, 12663-12676.
- (2) Gomes, H.; Serp, P.; Kalck, P.; Figueiredo, J.; Faria, J. *Topics in Catal.* 33, 59-68.
- (3) Aksoylu, A. E.; Faria, J. L.; Pereira, M. F. R.; Figueiredo, J. L.; Serp, P.; Hierso, J.-C.; Feurer, R.; Kihn, Y.; Kalck, P. *App. Catal. A: Gen.* 2003, 243, 357-365.
- (4) Vlčko, M.; Cvenegrošová, Z.; Hronec, M. *Collect. Czech. Chem. Commun.* 2008, 73, 1149-1160.
- (5) de Miguel, S. R.; Scelza, O. A.; Román-Martínez, M. C.; Salinas-Martínez de Lecea, C.; Cazorla-Amorós, D.; Linares-Solano, A. *App. Catal. A: Gen.* 1998, 170, 93-103.
- (6) Job, N.; Pereira, M. F. R.; Lambert, S.; Cabiac, A.; Delahay, G.; Colomer, J.-F.; Marien, J.; Figueiredo, J. L.; Pirard, J.-P. *J. Catal.* 2006, 240, 160-171.

- (7) Kim, H. Y.; Lee, S. J.; Jung, N. J. *Solid State Phenomena* 2007, 124-126, 1769-1772.
- (8) Lee, I.; Delbecq, F.; Morales, R.; Albiter, M. A.; Zaera, F. *Nat Mater* 2009, 8, 132-138.
- (9) Eriksson, S.; Nylén, U.; Rojas, S.; Boutonnet, M. *App. Catal. A: Gen.* 2004, 265, 207-219.
- (10) Yadav, O. P.; Palmqvist, A.; Cruise, N.; Holmberg, K. *Colloids and Surfaces A* 2003, 221, 131-134.
- (11) Pal, A.; Shah, S.; Belochapkine, S.; Tanner, D.; Magner, E.; Devi, S. *Colloids and Surfaces A* 2009, 337, 205-207.
- (12) Magno, L. M.; Angelescu, D. G.; Sigle, W.; Stubenrauch, C. *Phys. Chem. Chem. Phys.* 2011, 13, 3048.
- (13) Harelind Ingelsten, H.; Beziat, J.-C.; Bergkvist, K.; Palmqvist, A.; Skoglundh, M.; Qiuhong, H.; Falk, L. K. L.; Holmberg, K. *Langmuir* 2002, 18, 1811-1818.
- (14) Yashima, M.; Falk, L. K. L.; Palmqvist, A. E. C.; Holmberg, K. *J. Colloid Interface Sci.* 2003, 268, 348-356.
- (15) Ikeda, M.; Takeshima, S.; Tago, T.; Kishida, M.; Wakabayashi, K. *Catal. Lett.* 1999, 58, 195-197.
- (16) Ahmadi, T. S.; Wang, Z. L.; Green, T. C.; Henglein, A.; El-Sayed, M. A. *Science* 1996, 272, 1924-1925.
- (17) Ahmadi, T. S.; Wang, Z. L.; Henglein, A.; El-Sayed, M. A. *Chem. Mater.* 1996, 8, 1161-1163.
- (18) Zhu, J.; Kónya, Z.; Puentes, V. F.; Kiricsi, I.; Miao, C. X.; Ager, J. W.; Alivisatos, A. P.; Somorjai, G. A. *Langmuir* 2003, 19, 4396-4401.
- (19) Song, H.; Rioux, R. M.; Hoefelmeyer, J. D.; Komor, R.; Niesz, K.; Grass, M.; Yang, P.; Somorjai, G. A. *J. Am. Chem. Soc.* 2006, 128, 3027-3037.
- (20) Burda, C.; Chen, X.; Narayanan, R.; El-Sayed, M. A. *Chem. Rev.* 2005, 105, 1025-1102.
- (21) Buchold, D. H. M.; Feldmann, C. *Adv. Funct. Mater.* 2008, 18, 1002-1011.
- (22) Zhao, D.; Huo, Q.; Feng, J.; Chmelka, B. F.; Stucky, G. D. *J. Am. Chem. Soc.* 1998, 120, 6024-6036.
- (23) Milano-Brusco, J. S.; Nowothnick, H.; Schwarze, M.; Schomäcker, R. *Ind. Eng. Chem. Res.* 2010, 49, 1098-1104.
- (24) Eastoe, J.; Hollamby, M. J.; Hudson, L. *Adv. Colloid Interface Sci.* 2006, 128-130, 5-15.
- (25) Ganguli, A. K.; Ganguly, A.; Vaidya, S. *Chem. Soc. Rev.* 2010, 39, 474.
- (26) Müller, B. W.; Müller, R. H. *J. Pharm. Sci.* 1984, 73, 919-922.
- (27) Lade, M.; Mays, H.; Schmidt, J.; Willumeit, R.; Schomäcker, R. *Colloids Surf., A* 2000, 163, 3-15.
- (28) Tsung, C.-K.; Kuhn, J. N.; Huang, W.; Aliaga, C.; Hung, L.-I.; Somorjai, G. A.; Yang, P. *J. Am. Chem. Soc.* 2009, 131, 5816-5822.

- (29) P.J. Ferreira; Yang Shao-Horn *Electrochem. Solid-State Lett.* 2007, 10, B60-B63.
- (30) Swaminathan, R.; Willard, M. A.; McHenry, M. E. *Acta Materialia* 2006, 54, 807-816.
- (31) Lee, S. W.; Chen, S.; Sheng, W.; Yabuuchi, N.; Kim, Y.-T.; Mitani, T.; Vescovo, E.; Shao-Horn, Y. *J. Am. Chem. Soc.* 2009, 131, 15669-15677.
- (32) Alayoglu, S.; Aliaga, C.; Sprung, C.; Somorjai, G. A. *Catalysis Letters* 2011, 141, 914-924.
- (33) Zhou, M.; Chen, S.; Ren, H.; Wu, L.; Zhao, S. *Physica E* 2005, 27, 341-350.
- (34) Adityawarman, D.; Voigt, A.; Veit, P.; Sundmacher, K. *Chem. Eng. Sci.* 2005, 60, 3373-3381.
- (35) Zhang, X.; Chan, K.-Y. *Chem. Mater.* 2003, 15, 451-459.
- (36) Niesz, K.; Grass, M.; Somorjai, G. A. *Nano Lett.* 2005, 5, 2238-2240.
- (37) Shen, Q.; Wei, H.; Zhao, Y.; Wang, D.-J.; Zheng, L.-Q.; Xu, D.-F. *Colloids and Surfaces A: Physicochemical and Engineering Aspects* 2004, 251, 87-91.
- (38) Ranjan, R.; Vaidya, S.; Thaplyal, P.; Qamar, M.; Ahmed, J.; Ganguli, A. K. *Langmuir* 2009, 25, 6469-6475.
- (39) Bae, D.-S.; Kyong-Sop Han; James H. Adair *J. Am. Chem. Soc.* 2002, 85, 1321-1323.
- (40) Tao, A. R.; Habas, S.; Yang, P. *Small* 2008, 4, 310-325.
- (41) Vaidya, S.; Rastogi, P.; Agarwal, S.; Gupta, S. K.; Ahmad, T.; Antonelli, A. M.; Ramanujachary, K. V.; Lofland, S. E.; Ganguli, A. K. *J. Phys. Chem. C* 2008, 112, 12610-12615.
- (42) Rahman, M. R.; Saleh, F. S.; Okajima, T.; Ohsaka, T. *Langmuir* 2011, 27, 5126-5135.
- (43) Alayoglu, S.; Aliaga, C.; Sprung, C.; Somorjai, G. A. *Catalysis Letters* 2011, 141, 914-924.
- (44) El-Sayed, M. A.; Yoo, J. W. *Chem. Cat. Chem* 2010, 2, 268-271.
- (45) Liu, Z.; Shamsuzzoha, M.; Ada, E. T.; Reichert, W. M.; Nikles, D. E. *J. Power Sources* 2007, 164, 472-480.
- (46) Rioux, R. M.; Song, H.; Grass, M.; Habas, S.; Niesz, K.; Hoefelmeyer, J. D.; Yang, P.; Somorjai, G. A. *Top Catal* 2006, 39, 167-174.
- (47) Teranishi, T.; Hosoe, M.; Tanaka, T.; Miyake, M. *J. Phys. Chem. B* 1999, 103, 3818-3827.
- (48) Wang, Z. L.; Petroski, J. M.; Green, T. C.; El-Sayed, M. A. *J. Phys. Chem. B* 1998, 102, 6145-6151.
- (49) Boutonnet, M.; Kizling, J.; Touroude, R.; Maire, G.; Stenius, P. *Catal Lett* 1991, 9, 347-354.
- (50) Romero-Pascual, E.; Larrea, A.; Monzón, A.; González, R. D. *J. Solid State Chem.* 2002, 168, 343-353.
- (51) Miller, J. T.; Schreier, M.; Kropf, A. J.; Regalbuto, J. R. *J. Catal.* 2004, 225, 203-212.

Chapter 5

Particle shape optimization by changing from isotropic to anisotropic nanostructure:

Preparation of highly active and stable supported Pt catalysts in microemulsions

5.1. Introduction

In order to improve the catalytic activity of the noble metals, the surface morphology has become an area of investigation over the past decades. Several studies have reported that differently shaped metal catalysts show different catalytic activity and selectivity.¹⁻⁴ Therefore, the shape control of metal particles during synthesis, i.e. to direct the crystallographic planes, coordination of surface atoms and bounding facets of the nanocrystal, is important. These parameters determine the number of atoms located at the edges or corners and accordingly control the surface chemistry which holds the key for improving their catalytic performance. Therefore, in the synthesis of metal nanoparticles, not only the size needs to be controlled and optimized, but also the shape.

Although many scientists have successfully synthesized Pt nanoparticles with different shapes, almost all the shapes end up with low indexes such as {111} and {100}.^{5,3,6,7} These low index planes comprise of densely packed atoms which have a low amount of edges and corners and thus low surface energy. Therefore, the shape that possesses

high-index planes (low-coordinated atoms) is preferable because generally it has high surface energies and thus exhibits high activity. Surface energies corresponding to different crystallographic facets usually increase in the order $\gamma_{\{111\}} < \gamma_{\{100\}} \ll \gamma_{\{110\}} \ll \gamma_{\{hkl\}}$, where $\{hkl\}$ represents high-index facets, with at least one h , k , and l equal to two or greater.⁸ Although the synthesis of nanocrystals with high-index surfaces was achieved by some groups, the size of the crystals is still rather high (20 – 240 nm).^{9,10} More important for catalysis, shape control with precision at a scale smaller than 10 nm effectively engineers the chemical surface of the nanoparticle.⁹ Therefore the formation of small nanoparticles with high index facets remains challenging.

To produce nanoparticles which have high-index planes, the preferred growth direction during synthesis is anisotropic growth. It can be induced by employing surfactants which can bind preferentially to crystal faces of the growing particles.^{10,11} In our previous work, we were able to prepare multifaceted Pt nanoparticles and we concluded that the shape is dominantly influenced by the surfactant.^{11,12} However, this account is appropriate probably only if a strong reducing agent is used. We used a strong reducing agent, hydrazine, to make sure that the reduction process will be faster and thus not contribute in regulating the shape. However, the anisotropic growth can also be promoted by a very slow reduction rate at room temperature and the lowest energy principle.¹³ The slow reduction rate of the metal precursor can be carried out by means of a weak reducing agent. A weak reducing agent effectively isolates the nucleation and growth events allowing control over the size and shape.^{14,15} This statement is also confirmed by some published results which show that some weak reducing agents such as formic acid and ascorbic acid are effective for producing anisotropic platinum nanostructures.^{16,17,13,18} Pillai et al. reported that when NaBH_4 is replaced by HCOOH , nanoflowers comprised of large quantities of nanowires are obtained.⁴ Chen et al. reported that by slowing the reduction rate (extremely low supersaturations) of Pt salts, only highly anisotropic Pt nanostructures were formed. In contrast, if the reduction proceeded too fast (the supersaturation was too high) only isotropic Pt nanoparticles were produced.¹⁹

Despite the high activity of complex anisotropic nanostructures, generally they are still produced in a colloidal state which is thermodynamically unstable.⁹ Moreover, the use of capping agents in colloidal systems in most cases hinders or even prevents catalysis by blocking some of their active sites and also through inducing steric effects.⁴ As a

matter of fact, when our Pt particles in a microemulsion-based suspension were tested catalytically via the hydrogenation of α -methyl styrene, the activity was very poor compared with its supported counterparts. The same observations are also obtained by Boutonnet et al.²⁰ Therefore, it is far better to have a stable state and an unhindered contact between the substrates and active sites of the metal. An alternative approach is to stabilize the metal particles by dispersing them on a support. However, it is often difficult to obtain a good dispersion while preserving the size and shape of nanoparticles during the deposition process.^{12,21} The dispersion of nanoparticles on the support is significant because it affects the catalyst performance. This difficult challenge, however, has been overcome in our method, i.e. the thermo-destabilization of microemulsions.

In our recent study, we presented a new method to synthesize active and stable supported Pt catalysts.¹² There are several major parameters that determine the size, shape and dispersion of metal on the support which influence the catalyst performance such as the concentration of surfactant and oil, concentration of precursors, heating rate during destabilization, kind of support, etc. In order to improve the activity of our Pt catalysts, we decided to modify the shape of the Pt particles by changing the reducing agent and the Pt precursor.

Because the comprehensive study of our synthesis method has been reported in our previous paper, here we are focusing more on optimizing the performance of supported Pt catalyst by improving the surface energy of nanoparticles rather than comparing with other synthesis methods. In this study, we improve the catalytic activity mostly by means of a weak reducing agent (ascorbic acid). Combinations of the use of a weak reducing agent to create an anisotropic nanostructure and the deposition with thermo-destabilization of microemulsions method are potentially promising for increasing the activity of supported metal catalysts.

To elucidate whether this synthesis method is a viable strategy, we also tested the catalytic activity of our supported Pt catalysts in some reactions such as hydrogenation of methyl crotonate, itaconic acid and levulinic acid. However, the results are discussed only briefly in this paper.

5.2. Experimental Section

5.2.1 Materials

The chemicals used in the preparation of Pt nanoparticles were the following: Hexachloroplatinic acid hydrate (99.9%, Sigma-Aldrich) and Potassium tetrachloroplatinate(II) (99.9%, Sigma-Aldrich) as Platinum precursors; hydrazine monohydrate (98%, Sigma-Aldrich) and L-(+)-ascorbic acid (>99%, Alfa Aesar) as reducing agents, Cyclohexane ($\geq 99.5\%$, Carl - Roth) as oil phase, 1-pentanol ($\geq 98\%$, Carl-Roth) as co-surfactant, and Triton X-100 (100%, Sigma-Aldrich) as surfactant. All the chemicals above were used without further purification. The support materials used were (base, neutral and acid)-Al₂O₃ (Sigma-Aldrich), SiO₂ (Sigma-Aldrich), Sipernat 310 (Evonik) and self prepared SBA-15 according to the method reported by Zhao et.al.²² All supports were pre-calcined before use. For the washing of the catalysts after the synthesis, acetone ($\geq 99.8\%$, Carl Roth) was used. The chemicals used for the hydrogenation reactions: methanol ($\geq 99.9\%$, Carl Roth) as solvent; α -methyl styrene (99%, Aldrich), methyl crotonate (99 %, Sigma-Aldrich), itaconic acid (99 %, Sigma-Aldrich) and levulinic acid (98 %, Sigma-Aldrich) as reactants; all were used as received.

5.2.2 Catalyst Preparation

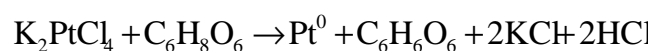
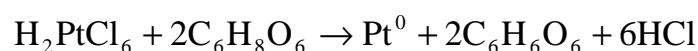
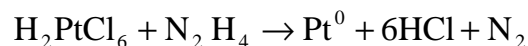
5.2.2.1 Phase Behaviour of Microemulsion Systems

For the determination of the deposition temperature, the phase diagram of a microemulsion needs to be established. The principle and the stepwise preparation of phase diagrams have been described in the previous chapter.¹²

5.2.2.2 Synthesis of nanoparticles and deposition process

The typical synthesis using microemulsion systems for preparing Pt nanoparticles involves the water phase either with metal salts (H₂PtCl₆ and K₂PtCl₄) or reductants (hydrazine and ascorbic acid), Triton X-100 as the surfactant, pentanol as the co-surfactant and cyclohexane as the oil phase. The mass fraction of oil in the microemulsion system is defined by $\alpha = m_o / (m_o + m_w)$, whereas the mass fraction of surfactant and co-surfactant is defined by $\gamma = (m_s + m_{co-s}) / (m_s + m_{co-s} + m_o + m_w)$. The mass ratio of co-surfactant to surfactant is defined by θ . The values of α , γ and θ we

used for this study are 0.75, 0.4 and 1, respectively. The metal salts and reductants are then prepared in different concentrations. The reactions that occur during the mixing of microemulsions (collision of the water droplets) for different synthesis according to the kind of metal salt and the reducing agent are the following:



The microemulsions were mixed according to the calculated values of α , γ and θ . The synthesis of the platinum nanoparticles was carried out at 25 °C in a 200 ml double-wall glass reactor equipped with a double parallel three-blade impeller. The hydrazine microemulsion was added slowly to the reactor, which had already been filled with the Pt salt microemulsion, by a micro pump at the rate of 0.2 ml/s. The mixture was stirred at 700 rpm for 30 minutes (with N_2H_4) or 2 hours (with AA) respectively at room temperature to form colloidal stabilized Pt nanoparticles. Then the pre-calcined support (500 °C for 2 hours) was added to the mixture, and the Pt nanoparticles were deposited on the support material by heating the microemulsion to 46 °C, at the heating rate of 1°C/min. After the deposition process, the mixture was cooled down. After all the supported catalysts precipitated, they were carefully separated from the solution, washed three times with pure acetone. Consistent to prior work, calcination was carried out at 300 °C for 2 hours to avoid the shape modification of metal nanoparticles.

5.2.2.3 Activity testing in hydrogenation reaction.

Hydrogenation of AMS was performed over the Pt/ Al_2O_3 catalysts to expound the effect of particle morphology on the catalytic activity. The activity testing in hydrogenation reaction has been described in the previous chapter.

5.2.2.4 Characterization and Analysis Methods.

The shape, size, and lattice structure of the Pt nanoparticles were investigated by transmission electron microscope (TEM) at an FEI Titan 80-300 (sub-Angstrom resolution, able to investigate at atomic scale), and also with FEI Tecnai G²⁰ S-Twin

TEM and Philips CM200/FEG high-resolution TEM (HRTEM) operated at 200 kV. Both microscopes are equipped with an energy dispersive x-ray detector (EDX). The TEM grids were prepared for imaging by placing a small drop of the specimen solution on a copper grid having an amorphous carbon film less than 20 nm thick and allowing it to dry completely in air at ambient temperature. Pt content of the support catalysts were analyzed by ICP-OES Element 2 (Varian) at low resolution (sample gas 0.863 L/min; plasma power 1350 W). The effective surface charges (ζ -Potential) on the Pt nanoparticles and alumina support material were measured using zeta-potential Zen 3600 (Malvern Instruments Zetasizer, Worcestershire, UK) equipment, with samples thermostated at 25 °C. The specific surface areas of the catalysts were measured via the BET method using N₂ adsorption at liquid N₂ temperature in a Micromeritics Gemini III 237 Volumetric Surface Analyzer. The sample was outgassed at 200 °C for 1 h in order to desorb any impurities or moisture from its surface.

5.3 Results and discussion

5.3.1 Effect of reducing agent on catalytic activity.

As we already mentioned, with our previous result we are able to produce truncated octahedron Pt nanocrystals in the microemulsions system by using hydrazine as the reductant. To see whether the reducing agent affects the morphology of the produced Pt particles, we used ascorbic acid (AA) as the reductant since it should lead to a slower reducing process. The result is illustrated in Figure 5.1. The TEM images show the Pt particle with hexagonal form (upper) after reduction with hydrazine and the dendritic form (bottom) after reduction with ascorbic acid. This confirms what we have previously described, namely that using a weaker reducing agent in the microemulsion-based synthesis, the shape of the nanoparticles is affected by the reducing agent rather than by the surfactant. In fact, Shen et. al. produce dendritic Pt nanostructures while using four different surfactants in sonoelectrochemical method.²³ Wang et. al., without using any surfactant, cannot synthesize nanodendrite Pt nanostructures by using hydrazine or NaBH₄, but they can produce them by using ascorbic acid as the reducing agent.¹⁶ Unfortunately, because they do not use a capping agent, they produce polydisperse Pt nanodendrites (20 – 70 nm). They also reported that a byproduct of Pt reduction by AA, diketo-l-gulonic acid (DGA), serves as a shape-directing agent to

direct the branched growth.¹⁶ The mechanism of the growth of branches seems to involve controlled, epitaxial growth from the surface of a particle.²⁴

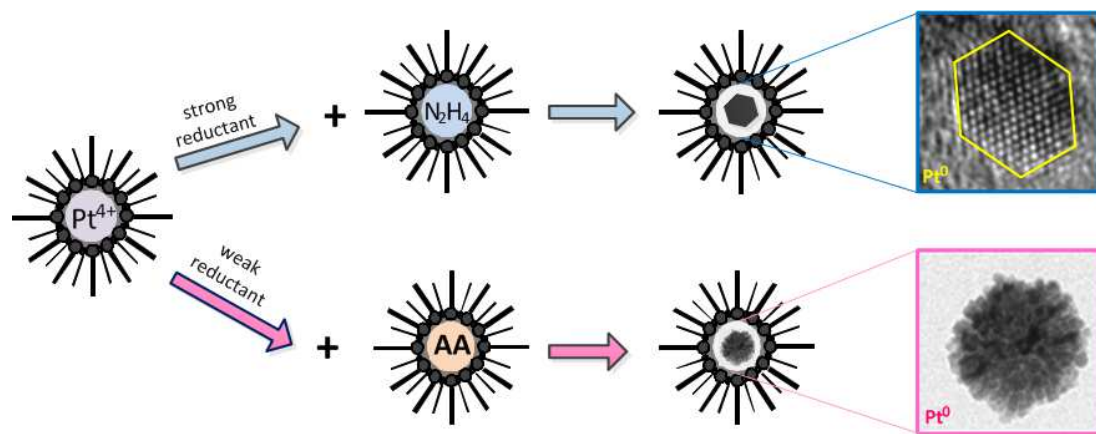


Figure 5.1 Illustration of the role of the reducing agent to produce different shapes of Pt nanoparticles.

Although hydrazine was found to be the best reducing agent because the particle distribution was optimal when compared with the one obtained for metals reduced with NaBH_4 , H_2 or other reducing agents,²⁵ it cannot promote the anisotropic growth. Moreover, it was observed for some cases that the remaining hydrazine behaved as a poison for the catalyst.²⁵ Therefore, it can be concluded that in this case using AA as a reductant is more favorable.

5.3.2 Structure of Pt nanodendrites in water droplets

Figure 5.2 shows the detailed structure of Pt nanodendrites which compose of irregular shaped arms as portrayed in Figure 5.2A and 5.2B. This anisotropic growth is favored by a slow reduction process and relatively low temperature of synthesis ($25\text{ }^\circ\text{C}$).^{24,26} Figure 5.2A and 5.2B show the Pt dendrites produced with surfactant (in the water droplets) and without surfactant, respectively, with the same concentrations of Pt ions and reductant. The Pt dendrite in Figure 5.2A looks smaller than that in Figure 5.2B because the surfactant restricts the growth. Also, due to the relatively low concentration of H_2PtCl_6 inside the reverse micelles, only few branches of Pt nanodendrites can be produced. The branches seem to be not attached to one another because when the sample was exposed to the high voltage electron beams during TEM analysis, they were separated. This might also signify that this structure is not mature

yet. However the branch consists of high index planes as depicted in a detailed structured in HRTEM image (Figure 5.2C) and the corresponding Fast Fourier transform (FFT) of the atomic lattice (Figure 5.2D). The electron diffraction pattern indexed to the $\{111\}$, $\{200\}$, $\{220\}$, $\{311\}$, $\{331\}$ and $\{511\}$ diffractions, respectively.

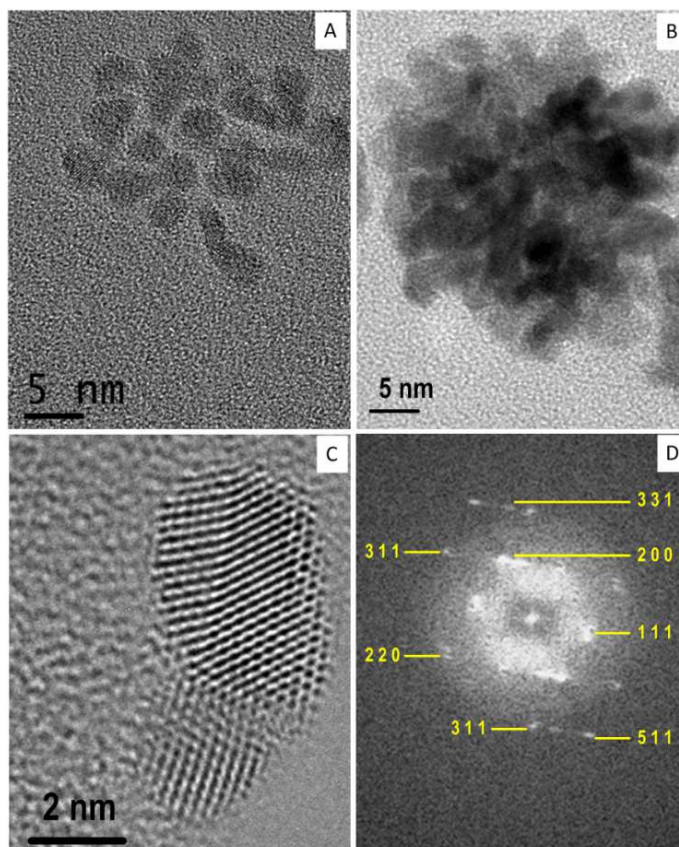


Figure 5.2 Pt clusters produced with ascorbic acid as reductant in the presence of the surfactant (A), in the absence of the surfactant (B), HRTEM of a branch of Pt dendrite (C), and its Fast Fourier transform (FFT) with the lattice indexes (D)

As stated above, the thermodynamic equilibrium shape of Pt particles produced when using hydrazine as the reductant is truncated octahedron. This regular crystallite is composed of the lowest-index crystal planes $\{111\}$ and $\{100\}$, which are known to be the least active. The irregular polycrystalline structure produced with AA, Pt nanodendrite, is our expected result because it is composed of the higher index crystal planes especially $\{311\}$, $\{331\}$ and $\{511\}$. The high index planes exhibit much higher

reactivity because of the low coordination number and high density of atomic steps, ledges and kinks, which usually serve as active sites for breaking chemical bonds.⁴ This is confirmed by Figure 5.3 that shows the higher activity of supported Pt nanodendrites catalysts compared to that of Pt truncated octahedron. Hence, the irregular structure of nanodendrites provides more active sites than the truncated octahedron.

5.3.3 Effect of support acidity on catalytic activity

We also observe that the support acidity affects the activity of the Pt catalyst (Figure 5.3 and Table 1). We note that we used the acidic, neutral and basic Al_2O_3 which are commercially available. The lowest activity of the Pt nanodendrite deposited on basic Al_2O_3 can be explained as follows. For Pt particles which are reduced with ascorbic acid, the microemulsions containing Pt particles are acidic ($\text{pH} \approx 4$). Therefore, they tend to destabilize quickly when they are around the basic Al_2O_3 and Pt particles agglomerate before deposition, whereas on acidic Al_2O_3 the catalyst shows higher activity because the particles are more stable before attaching to the support material. On the contrary, for Pt particles which are reduced with hydrazine, the microemulsions containing Pt nanoparticles are alkaline ($\text{pH} \approx 9$). Consequently, the particles tend to agglomerate before deposition when surrounded by the acidic Al_2O_3 and be more stable when in contact with basic Al_2O_3 .

The TEM images in Figure 5.3 show the clear particle size distributions but they cannot give accurate dispersions because they show the particles at the outer and inner surfaces of the support. For this reason, we confirm them with SEM images which show the dispersion of the particles on the outer surface (the particle is shown in white color). From the TEM images, we can see that there is only little Pt particle agglomeration on acidic alumina compared to the neutral and basic alumina, as pointed out by the small arrows. A dark field image (the inset of Figure 5.3B, middle centre), is presented to clearly show the dispersion of Pt particles on the neutral alumina. The Pt dispersion at acidic and neutral alumina looks similar in the SEM images. Interestingly, in the case of Pt on the basic alumina, the outer particles are quite few and widely scattered. This looks contrary to its TEM image (middle right) which shows that the particles are rather dense. We note that the TEM and SEM images were not taken from the same place. This may indicate that Pt particles on the basic alumina are not

well distributed. Hence, these visual observations are congruent with the catalytic activities because better dispersion leads to higher activity.

To validate the visual observations, we quantify the dispersion by using the Delaunay network method²⁷ based on the TEM images in Figure 5.3. In this case, we do not use SEM images because of their low magnifications, which is normal in a SEM investigation.

Table 5.1 Activities of 0.1%-wt supported Pt catalysts prepared with different molar ratios of Pt to AA

Support Material	ζ -Potential of support (mV)*	Molar Ratio [Pt] : [AA]	ζ -Potential of Pt NPs (mV)	Pt Activity (mol/s.g _{Pt})
acidic- Al ₂ O ₃	+ 45	1 : 25	-24.9	11000
		1 : 50	-25.4	65000
neutral- Al ₂ O ₃	+ 40	1 : 25	-24.9	9000
		1 : 50	-25.4	49000
basic- Al ₂ O ₃	+ 10	1 : 25	-24.9	7000
		1 : 50	-25.4	29000

* experimentally measured at pH = 4, which is the average pH of the prepared microemulsion containing Pt nanodendrites

The details of the Delaunay network method are described in the **Appendix C**. As we can see in Figure 5.3B (upper right), according to this method, the dispersions of Pt particles on the acidic, neutral and basic alumina are in the areas of good, random like and poor, respectively. These quantified results support the visual observations and certainly agree with the catalytic activities.

To verify our observations, we also investigated the interaction between the Pt particles and the support material by measuring their zeta potentials. As we can see in Table 5.1, the zeta potential of the platinum nanodendrites is about -25 mV whereas the zeta potentials of acidic, neutral and basic Al₂O₃ are +45, +40 and +10 mV respectively.

The more positively charged support particles are more likely to interact with the negatively charged metal particles which can result in better dispersion. Therefore, the dispersion of Pt nanodendrites seems to be better on acidic Al_2O_3 followed by neutral Al_2O_3 and basic Al_2O_3 which results in an activity decrease of Pt catalysts with the support material ranking from acidic to basic Al_2O_3 .

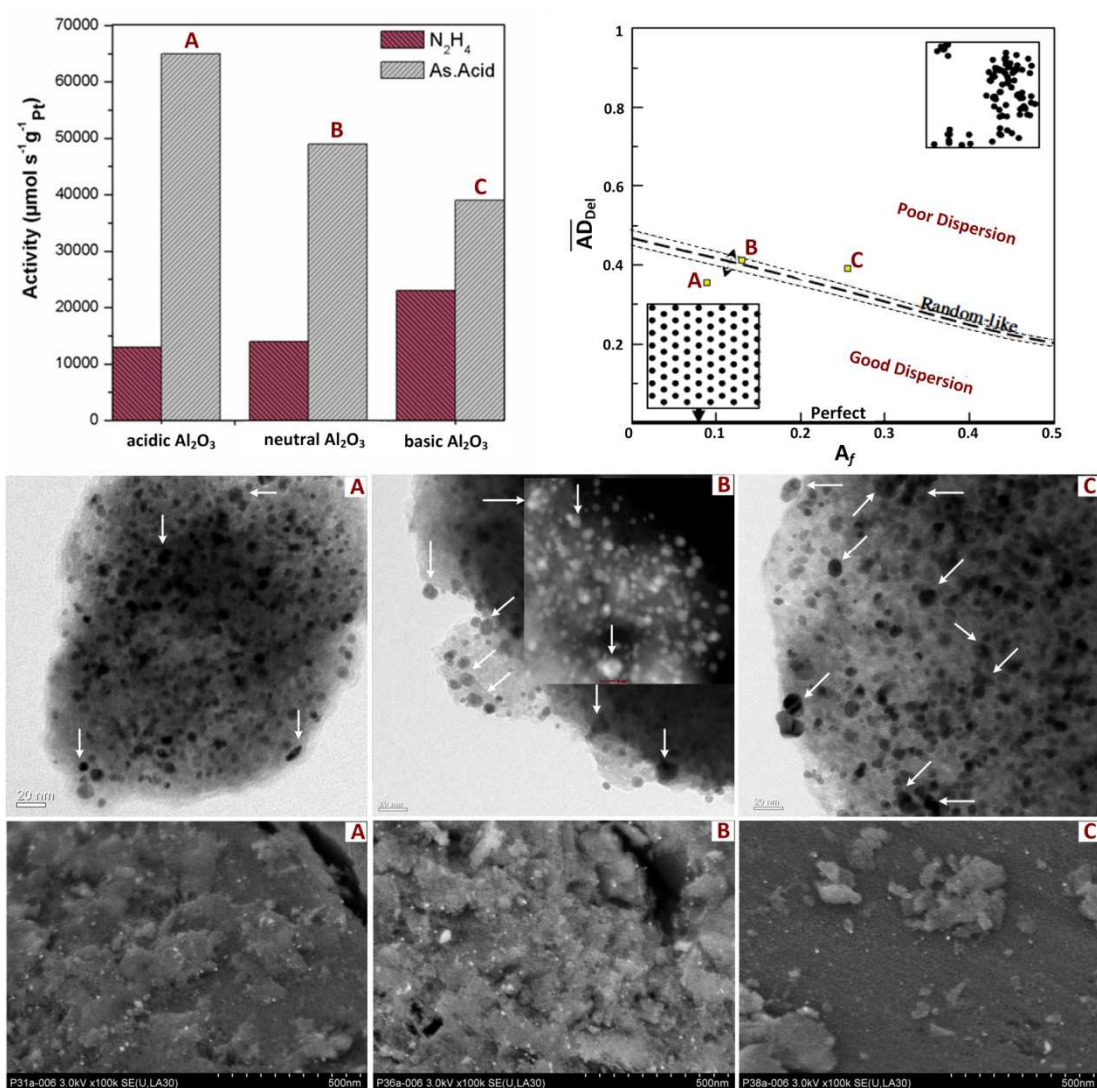


Figure 5.3 Upper left: activities of Pt catalysts reduced with either hydrazine or AA and deposited on acidic (A), neutral (B), basic (C) alumina supports. Upper right: degrees of dispersion of the corresponding catalysts with the Delaunay network method (Modified with permission from Ref 27). Middle and bottom are the TEM and SEM images of the corresponding catalysts respectively.

5.3.4 Effect of pH on the structure of nanodendrites

It is interesting to see that when we double the initial concentration of ascorbic acid, the activity of the Pt catalyst increases (Table 5.1). The increase of catalytic activity can be explained by the following. According to Nernst Equation, the higher the pH, the more negative the redox potential (E_h) will be and the stronger the reducing power.

$$E_h = E_0 - \frac{0.05916}{2} \log \frac{[DHA]}{[AA]} - 0.05916 \text{pH} \quad (5.1)$$

Hence, increasing the concentration of AA (lower pH) will lower the reducing power of AA and therefore slow down the reduction process of Pt. Consequently, this will promote the anisotropic growth of Pt nanodendrites which results in more complex structures (more edge and corner sites), thus leading to the higher activity. On the other hand, slow reduction of Pt will also lead to bigger particle size¹² as confirmed by the TEM image (right) in Figure 5.4 that shows bigger Pt particles produced with more AA (the particle sizes produced with Pt to AA ratios of 1:25 and 1:50 are 4.6 ± 1.2 nm and 7.7 ± 2.6 nm, respectively). However, as we already know, the reduction of Pt takes place inside of the reverse micelles, which, in turn, can limit the growth of the metal cluster. Hence, the effect of the reducing agent might be restricted.

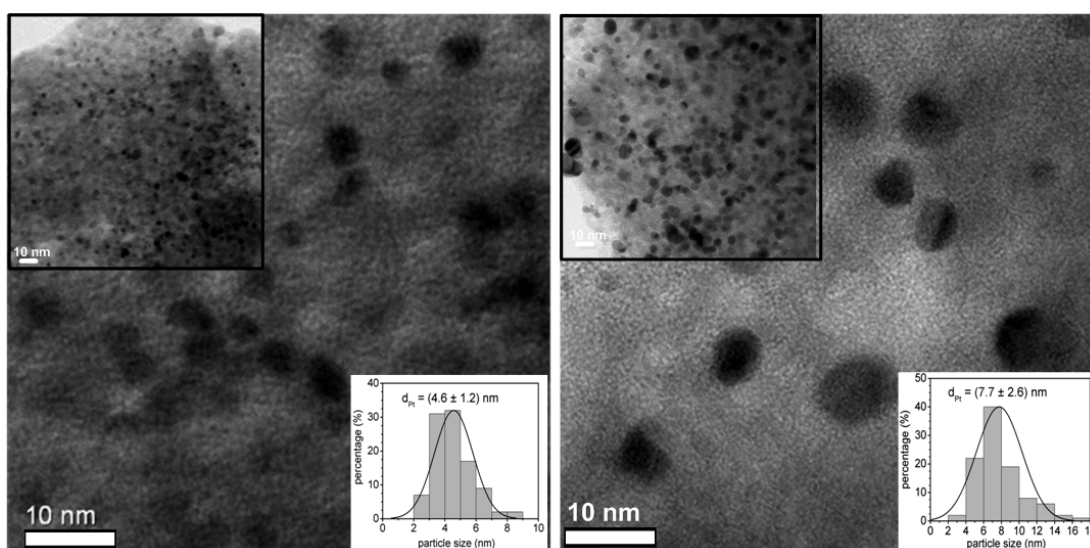


Figure 5.4 Pt nanodendrites supported on acidic Al_2O_3 prepared with different initial molar ratios of Pt to AA, 1:25 (left) and 1: 50 (right). The upper and bottom insets are the corresponding TEM images with low magnification and the particle size distributions (100 particles were counted)

Therefore, this phenomenon indicates that to such an extent, the shape of complex structure Pt nanodendrites seems to have more influence on the activity than the particle size. This phenomenon is also observed in our previously published results which shows that increasing the concentration of hydrazine (higher pH) will increase its reducing power which promotes a fast reduction of Pt ions. Faster reduction of Pt ions will produce smaller particles, thus leading to higher activity of the Pt catalyst.¹² In addition, the influence of pH on the structure of obtained Pt nanoparticles is also reported by Ji et al. and Lee et al.^{28,29}

More interestingly, when we increase the initial molar ratio of Pt to AA and then deposit the produced particles on SBA-15, a different trend is observed (Figure 5.5). The aforementioned results demonstrate that increasing the initial molar ratio of Pt to AA leads to bigger particles. On the other hand, the bigger particles (more than 10 nm) cannot get into the pores of SBA-15. In the case of Pt supported on SBA-15, the particle size produced with $[Pt]:[AA]$ of 1:25 is less than 10 nm whereas with 1:50 is greater than 10 nm (inset in Figure 5.5). This is consistent with previous results which are shown in Figure 5.4. Unfortunately, we have no data of 1:100 but as previously hypothesized, the particles are expected to be bigger.

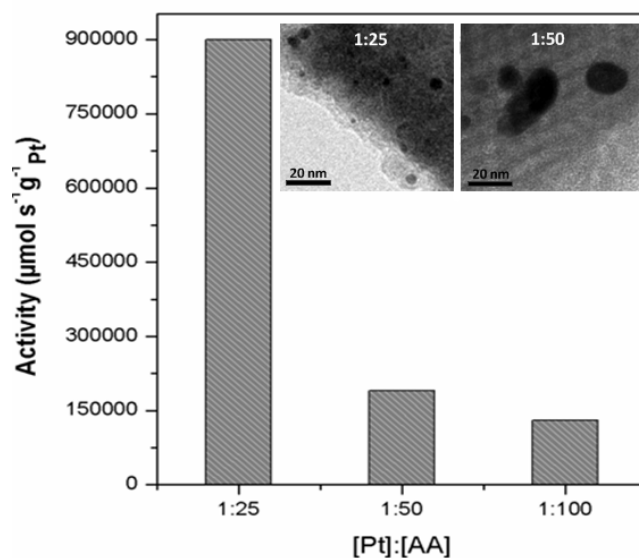


Figure 5.5 Activities of the Pt nanodendrites deposited on SBA-prepared in different molar ratio Pt to AA and the corresponding TEM images (inset).

The decrease of Pt activity shown in Figure 5.5 indicates that the bigger Pt particles produced from initial ratios of Pt to AA of 1:50 and 1:100 are unable to spread well over SBA-15 and penetrate into the pores, and even might have a tendency to agglomerate.

It is observed that the dispersion of Pt particles on the support is significantly more homogeneous with alumina (Figure 5.6 c and d), than with SBA-15 (Figure 5.6 a and b), particularly in the sample containing small particles. We attribute this to the value of the zeta potential of SBA-15 (approx. -20) which is almost the same as Pt nanoparticles (approx. -25). This observation is in good accordance with results published by Barkhuizen et al.²¹ Interestingly, although the Pt particles produced with hydrazine are smaller and better in distribution on the support, their activities are lower than those prepared with AA. To emphasize again, the anisotropic structure of the irregular polycrystalline Pt nanodendrites provides more active sites than the surface of a regular crystalline and therefore is the reason for the higher activities of the catalysts. Hence, as previously discussed in section 3.4, in our case, the shape of the particles is more significant in affecting the activity of the catalyst than the particle size despite bigger size and poor arrangement. This fact shows that the strategy of “making things smaller and smaller” – which is nowadays the strategy followed by many scientists – does not always lead to catalysts with better properties.

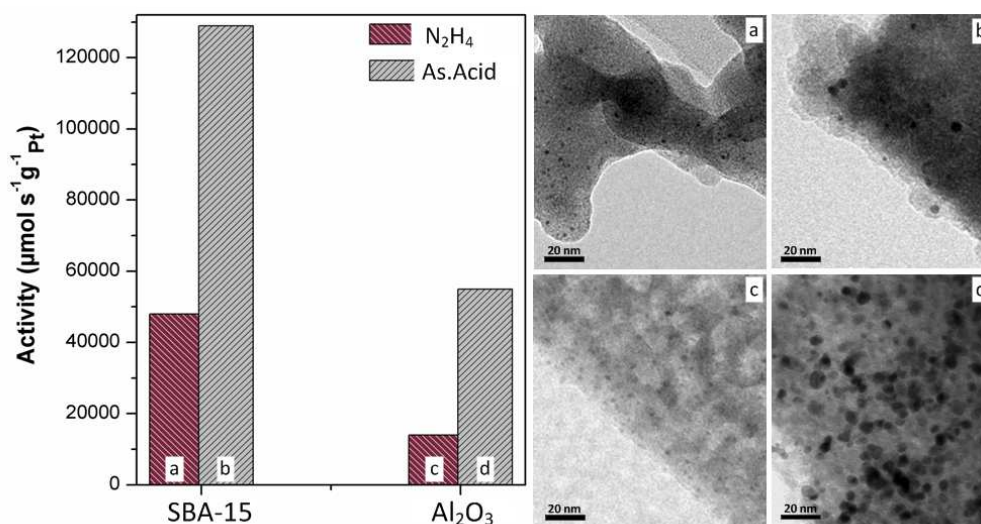


Figure 5.6 Activities of the supported Pt catalysts prepared with hydrazine and ascorbic acid as reductants and the corresponding TEM images.

5.3.5 Effect of metal precursor on catalytic activity

The activity was further optimized, when the metal precursor was replaced by K_2PtCl_4 , and a significant improvement of activity was observed. We attribute this to the fact that it is easier for AA to reduce the Pt^{2+} ion to Pt^0 rather than Pt^{4+} , which leads to more formation of dendritic branches. In addition, Duff et al. reported that the reduction of $PtCl_4^{2-}$ proceeds much faster than of $PtCl_6^{2-}$.³⁰ As a result, the particles that are produced from $PtCl_4^{2-}$ are smaller but higher in number than those from $PtCl_6^{2-}$. This is confirmed by HRTEM images (insets) in the bottom part of Figure 5.7 which show the corresponding Pt dendrites in the water droplets with different magnifications.

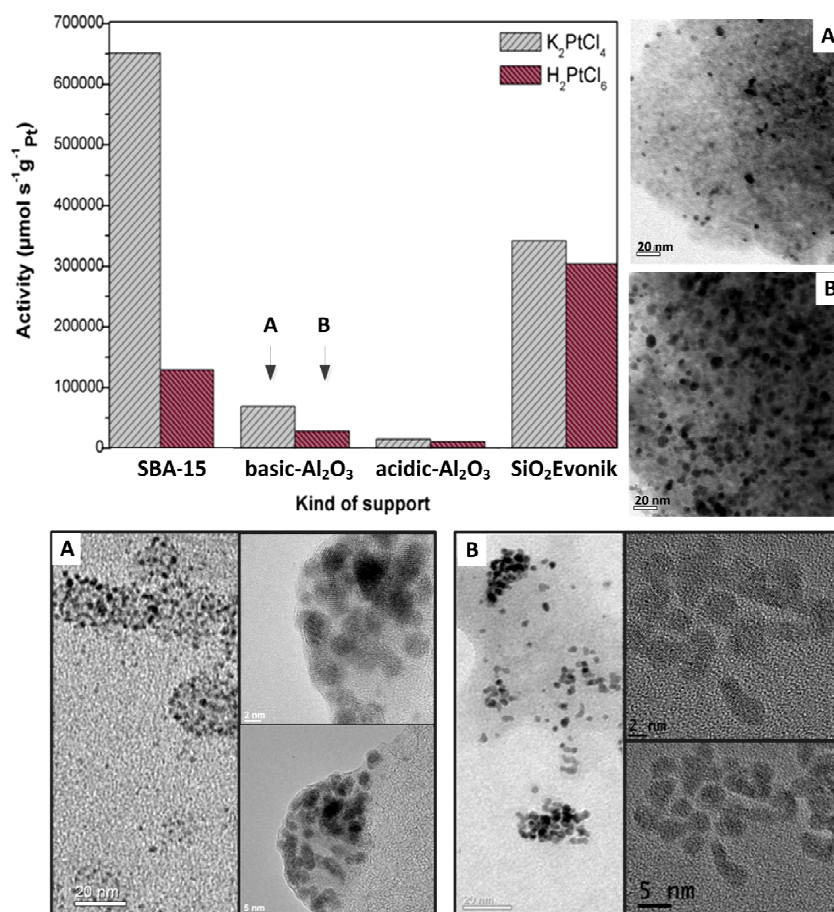


Figure 5.7 Upper: Activities of the supported Pt catalysts produced from different Pt precursors, K_2PtCl_4 (A) and H_2PtCl_6 (B), and the corresponding TEM images for basic Al_2O_3 . Bottom: the corresponding HRTEM images of Pt nanodendrites inside of the water droplets. The branches of Pt dendrites were separated and always moving when they were exposed to high voltage electron beams during the TEM investigation.

According to our observation in TEM investigations, during the transmission, the high voltage electron beams from the TEM filament affected the original structure of the Pt dendrites which caused separation and movement of the branches on the carbon grid. However, we can still see that the branches of Pt dendrites produced by K_2PtCl_4 are smaller than those by H_2PtCl_6 .

Duff et al. also suggested that the chloride ions play a determining role in the shape of Pt particles. In this case, although the greater amount of chloride ions present in the solutions will cause the slower reduction process, they do not promote the anisotropic growth. Instead, they limit the nucleation, hinder the combination of growing clusters, and as a result promote regular growth (isotropic) forms. By this hypothesis, it can be assumed that the increase of Cl^- ions could retard the formation of the anisotropic structures of Pt nanodendrites. Therefore, the shape of Pt nanodendrites produced from K_2PtCl_4 is more irregular than those from H_2PtCl_6 and thus provides more active sites.

5.3.6 Catalytic testing with different substrates

Additionally, as we have already shown in our previous paper, the activities of Pt catalysts prepared with our method and using hydrazine as the reductant are at least 4 times higher for AMS hydrogenation than those of the commercial Pt catalysts. If we compare now the Pt catalysts prepared by this optimized procedure with the commercial Pt catalysts, their activities are obviously much higher. Therefore, to verify the activity of our catalysts, we used our Pt/Al_2O_3 as a representative catalyst to hydrogenate some other substrates such as methyl crotonate, itaconic acid and levulinic acid and then compared its performance to that of the commercial one. The results show that our Pt catalyst performs better with all substrates than the commercial one as depicted in Figure 5.8.

5.3.7 Stability testing

The aforementioned results show that the structure of Pt nanodendrites is irregular and low-coordinated atoms tend to be unstable.¹⁴ Because the stability is also an important parameter in the application of a catalyst, the stability of the supported Pt nanodendrites was tested. We took our Pt/Al_2O_3 as a representative catalyst and used

it over 6 runs (Figure 5.9) of AMS hydrogenation. From the observed catalytic activities and BET surface areas, we found that the catalyst is very stable.

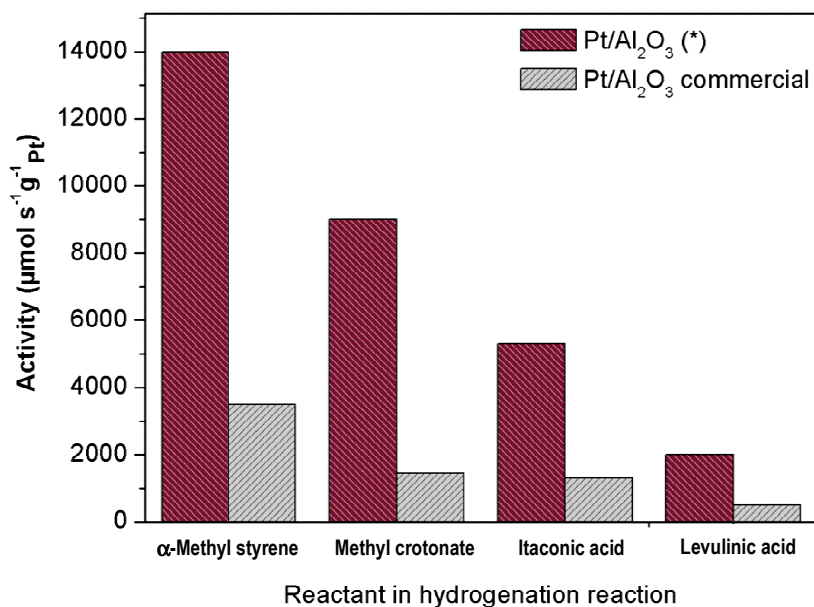


Figure 5.8 Activity testing of Pt/Al₂O₃ prepared via the thermo-destabilization method (*) compared to commercial Pt/Al₂O₃ for the hydrogenation reaction. All reactions were performed at 20°C and 1.1 bar, except levulinic acid hydrogenation: 70 °C and 1.3 bar.

This high durability indicates that the size and shape of Pt particles are considerably unchanged during reaction. This also implies that the interaction of the Pt particles with the alumina support is strong. Platinum catalysts which we prepared with hydrazine as reductant¹² also show excellent stability. However, we need to emphasize that our Pt/Al₂O₃ catalyst, as we already mentioned in the previous paper, is more suitable for mild temperature reactions.

RUN	1	2	3	4	5	6
BET (m^2/g)	147	147	148	148	152	146
Activity ($\mu\text{mol}\cdot\text{s}^{-1}\cdot\text{g}^{-1}$)	67000	69000	67000	68000	61000	65000

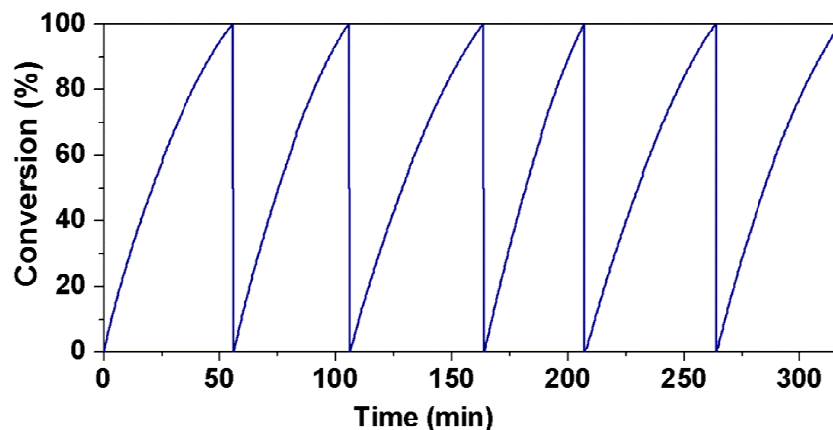


Figure 5.9 Stability test of Pt/ Al_2O_3 catalyst that produced with ascorbic acid

5.4. Conclusion

Here, we have demonstrated an optimized synthesis of supported Pt catalysts with thermo-destabilization of microemulsions by using AA as reducing agent and K_2PtCl_4 as metal precursor. As a weak reducing agent, ascorbic acid promotes a slow reduction of Pt ions and induces anisotropic growth which results in dendritic shape. This remarkable nanostructure is indeed highly attractive for catalytic applications because it has more edges and kinks. The intriguing aspect of the dendrite Pt nanoparticles discussed here is that the shape of nanoparticles is a key factor to the high activity in spite of the bigger size. Accordingly, the lower catalytic activity of the smaller isotropic particles which is described in this work shows that the strategy of making smaller and smaller particles does not always lead to a better catalyst. In addition, the support material is also an important factor to improve the activity of the catalyst. We suggest that the interaction between the particles and the support material which depends on the value of the zeta potential, influences or even controls the dispersion.

Although the test reactions given here refer to double bond hydrogenations, similar catalytic performance can be expected with other important reactions under mild conditions.

References

1. R. Narayanan and M. A. El-Sayed, *Nano Lett.*, 2004, **4**, 1343–1348.
2. V. Komanicky, H. Iddir, K.-C. Chang, A. Menzel, G. Karapetrov, D. Hennessy, P. Zapol, and H. You, *J. Am. Chem. Soc.*, 2009, **131**, 5732–5733.
3. K. M. Bratlie, H. Lee, K. Komvopoulos, P. Yang, and G. A. Somorjai, *Nano Lett.*, 2007, **7**, 3097–3101.
4. M. Subhramannia and V. K. Pillai, *J. Mater. Chem.*, 2008, **18**, 5858.
5. R. Narayanan and M. A. El-Sayed, *J. Phys. Chem. B*, 2005, **109**, 12663–12676.
6. H. Song, F. Kim, S. Connor, G. A. Somorjai, and P. Yang, *J. Phys. Chem. B*, 2005, **109**, 188–193.
7. N. V. Long, N. D. Chien, T. Hayakawa, H. Hirata, G. Lakshminarayana, and M. Nogami, *Nanotechnol.*, 2010, **21**, 035605.
8. Y. Xiong, B. J. Wiley, and Y. Xia, *Angew. Chem., Int. Ed.*, 2007, **46**, 7157–7159.
9. T. S. Ahmadi, Z. L. Wang, T. C. Green, A. Henglein, and M. A. El-Sayed, *Science*, 1996, **272**, 1924–1925.
10. C. de M. Donegá, *Chem. Soc. Rev.* 2011, **40**, 1512.
11. J. Xiao and L. Qi, *Nanoscale*, 2011, **3**, 1383.
12. R. Y. Parapat, V. Parwoto, M. Schwarze, B. Zhang, D. S. Su, and R. Schomäcker, *J. Mater. Chem.*, 2012, **23**, 11605–11614.
13. F. Si, L. Ma, C. Liu, X. Zhang, and W. Xing, *RSC Advances*, 2012, **2**, 401.
14. A. R. Tao, S. Habas, and P. Yang, *Small*, 2008, **4**, 310–325.
15. T. Yao, S. Liu, Z. Sun, Y. Li, S. He, H. Cheng, Y. Xie, Q. Liu, Y. Jiang, Z. Wu, Z. Pan, W. Yan, and S. Wei, *J. Am. Chem. Soc.*, 2012, **134**, 9410–9416.
16. L. Wang, C. Hu, Y. Nemoto, Y. Tateyama, and Y. Yamauchi, *Cryst. Growth & Design*, 2010, **10**, 3454–3460.
17. L. Wang, H. Wang, Y. Nemoto, and Y. Yamauchi, *Chem. Mater.*, 2010, **22**, 2835–2841.
18. Y. Song, Y. Yang, C. J. Medforth, E. Pereira, A. K. Singh, H. Xu, Y. Jiang, C. J. Brinker, F. van Swol, and J. A. Shelnutt, *J. Am. Chem. Soc.*, 2004, **126**, 635–645.
19. J. Chen, T. Herricks, and Y. Xia, *Angew. Chem., Int. Ed.*, 2005, **44**, 2589–2592.
20. M. Boutonnet, J. Kizling, V. Mintsä-Eya, A. Choplin, R. Touroude, G. Maire, and P. Stenius, *J. Catal.*, 1987, **103**, 95–104.
21. D. Barkhuizen, I. Mabaso, E. Viljoen, C. Welker, M. Claeys, E. Van Steen, and J. C. Q. Fletcher, *Adv. Mater.*, 2006, **78**, 1759–1769.
22. D. Zhao, Q. Huo, J. Feng, B. F. Chmelka, and G. D. Stucky, *J. Am. Chem. Soc.*

- 1998, **120**, 6024–6036.
23. Q. Shen, L. Jiang, H. Zhang, Q. Min, W. Hou, and J.-J. Zhu, *J. Phys. Chem. C*, 2008, **112**, 16385–16392.
 24. J. D. Hoefelmeyer, K. Niesz, G. A. Somorjai, and T. D. Tilley, *Nano Lett.*, 2005, **5**, 435–438.
 25. J. J. Spivey, G. W. Roberts, S. Rojas, S. Eriksson, and M. Boutonnet, *Catalysis*, Royal Society of Chemistry, **17**, 256–292, 2004.
 26. A. Nerowski, M. Poetschke, M. Bobeth, J. Opitz, and G. Cuniberti, *Langmuir*, 2012, **28**, 7498–7504.
 27. D. J. Bray, S. G. Gilmour, F. J. Guild, T. H. Hsieh, K. Masania, and A. C. Taylor, *J. Mater. Sci.*, 2011, **46**, 6437–6452.
 28. X. Ji, X. Song, J. Li, Y. Bai, W. Yang, and X. Peng, *J. Am. Chem. Soc.*, 2007, **129**, 13939–13948.
 29. H. Lee, S. E. Habas, S. Kweskin, D. Butcher, G. A. Somorjai, and P. Yang, *Angew. Chem., Int. Ed.*, 2006, **45**, 7824–7828.
 30. D. G. Duff, P. P. Edwards, and B. F. G. Johnson, *J. Phys. Chem.*, 1995, **99**, 15934–15944.
 31. Ciacchi, L.C, Pompe, W, and De Vita, A, *J. Am. Chem. Soc.*, 2001, **123**, 7371–7380.
 32. A. Henglein and M. Giersig, *J. Phys. Chem. B*, 2000, **104**, 6767–6772.
 33. A. Siani, *Synthesis of Supported Nanoparticles for Catalytic Applications*, ProQuest, 2007.
 34. W. A. Spieker, J. Liu, J. T. Miller, A. J. Kropf, and J. R. Regalbuto, *App. Catal. A: General*, 2002, **232**, 219–235.
 35. R. Ayala, E. S. Marcos, S. Díaz-Moreno, V. A. Solé, and A. Muñoz-Páez, *J. Phys. Chem. B*, 2001, **105**, 7588–7593.

Chapter 6

Preparation of Pd, Ru and Ag supported metal catalysts

Each metal has different chemical and physical properties which depend sensitively on particle size and shape. Therefore, it can be expected that the synthesis of supported metal catalysts, although the same synthesis procedure is applied to different metals, leads to catalysts which have different features. For example, as it has been described in the previous chapter, the zeta potential of a metal nanoparticle plays an important role in the metal dispersion on the support. As a result, because each metal has a different value of the zeta potential, the dispersions of obtained supported metal will be different from one to another. Based on this fact, the approach should be to elucidate whether the thermo-destabilization of microemulsions can be used for the preparation of different supported metal catalysts.

Aside from catalysts preparation, different metal catalysts also show different activities in a chemical reaction at the same conditions. Chapters four and five have presented in detail the preparation of supported Pt catalysts and their performance. In this chapter, the preparation of supported Pd, Ru and Ag catalysts via the thermo-destabilization of microemulsions will be discussed including their performance (Pd and Ru) in hydrogenation of α -methyl styrene, methyl crotonate and levulinic acid.

6.1 Microemulsion composition for the synthesis of metal nanoparticles

As already mentioned in Chapter 3, the reaction temperature was considered to determine the microemulsion composition in the synthesis of nanoparticles. At the beginning of this work, we intended to find the microemulsion composition which can produce small nanoparticles (less than 5 nm) at room temperature. Because the nanoparticle size is proportional to the value of ω (molar ratio of water to surfactant), two values of ω were taken for comparison, i.e. $\omega = 13$ and $\omega = 15$ (see Figure 6.1 upper and middle). The corresponding TEM images of both ω confirm that if the value of ω increases, the size of nanoparticles will increase. These two kinds of Pt nanoparticles (produced with $\omega = 13$ and $\omega = 15$) were synthesized with using hydrazine as the reductant.

Although the activities of the Pt particles produced by $\omega = 13$ and $\omega = 15$ are higher than the commercial ones, the structure of the particles is still isotropic which is composed of mostly lower index planes such as $\{111\}$ or $\{100\}$. Based on the literature¹⁻⁴, the activity can be more increased by changing the particle shape to an irregular or anisotropic structure because it provides high index planes. This can be done by a slow reduction process which can be promoted by a weak reducing agent and low reduction temperature. In order to produce a more irregular structure which may provide more defect structures, a bigger size is favorable. Therefore, a bigger value of $\omega = 26$ was chosen to provide bigger droplets. Expectedly, the size of the Pt particles is bigger than those of $\omega = 13$ and $\omega = 15$ as displayed in Figure 6.1. In this case, ascorbic acid is used as the reductant. Another advantage of having bigger nanoparticles is that the TEM instrument can clearly show the anisotropic structure. Therefore, the value of $\omega = 26$ (that is with $\alpha = 0.75$ and $\gamma = 0.4$) is chosen in the synthesis the Ag, Pd, and Ru nanoparticles for the comparison.

It is very interesting to identify that not only does the reaction temperature play an important role for the size, but also for the final shape of the nanoparticles.⁵ Ren and Tilley demonstrated that the morphology of platinum nanocrystals is highly dependent on the reduction temperature. When the temperature is increased, the number of branches in the Pt nanocrystals increases, producing tripods, octapods, or multipods.⁶

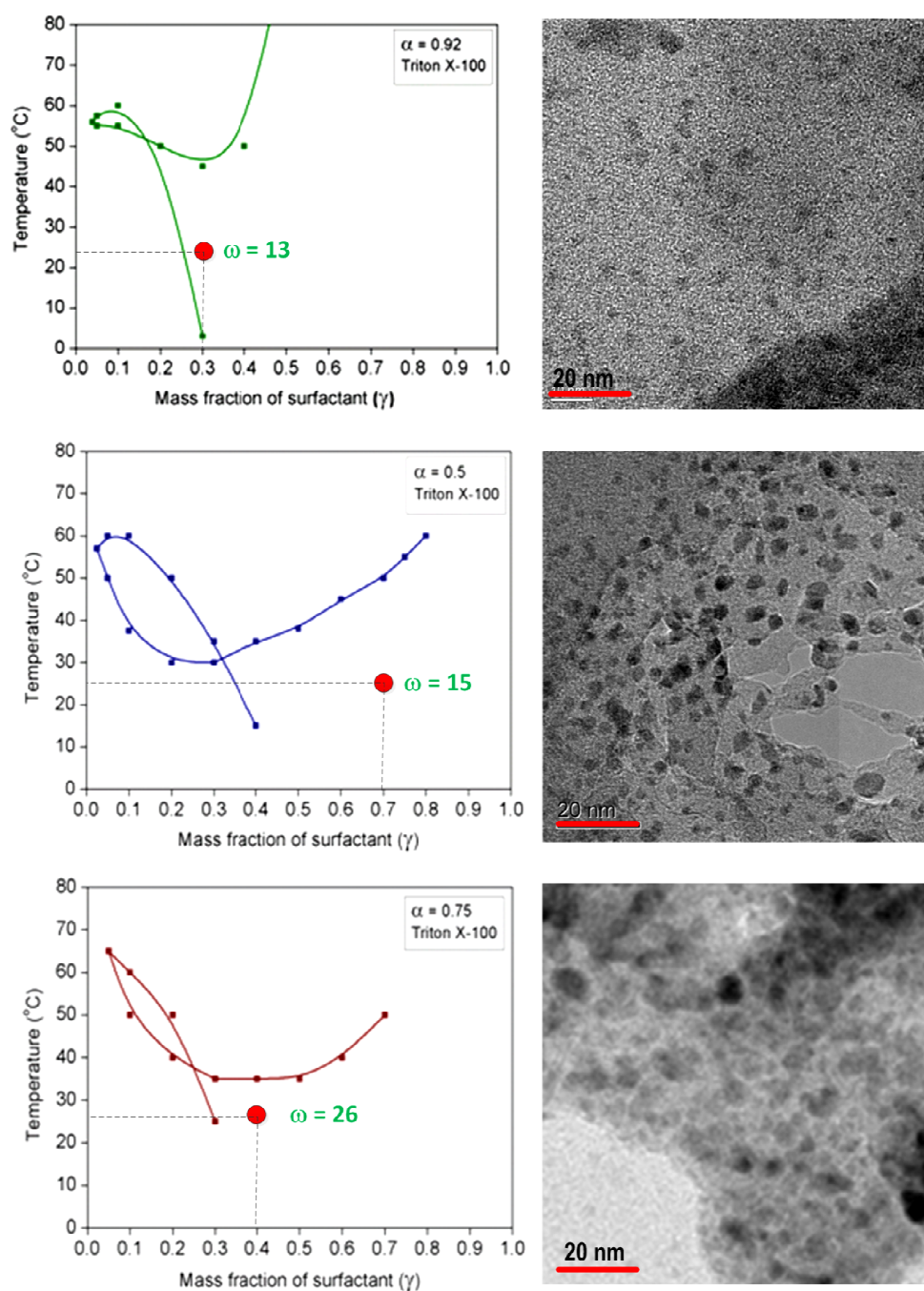


Figure 6.1 Left: Phase behaviour ‘fish diagrams’ of microemulsions (water-cyclohexane-pentanol-Triton X-100) at different oil compositions (α). Right: TEM images of the Pt nanoparticles in the w/o microemulsion prepared according to the value of the corresponding ω (molar ratio of water to surfactant) that is shown in the fish diagrams.

Therefore, as a deposition method to produce supported metal catalysts, thermostabilization of microemulsions is very suitable to promote the production of highly faceted nanocrystals, because the key element of the method is increasing the temperature. Therefore, when the temperature of microemulsions containing the metal particles is increased during the deposition, the shape renovation of particles to the anisotropic structure is induced.

6.2 Effect of growth time

In the microemulsion system, the nucleation and growth of particles are restricted within the water droplets. The advantage of this method is the ability to control the particle size and morphology by adjusting the corresponding parameters such as the concentration and type of surfactant, the concentration of precursors, molar ratio of water to surfactant, etc. In addition, it is also possible to tailor the size and structure of the final product by suitably controlling the reactions such as adjusting the growth time of the particle.

To study the growth mechanism of the nanoparticles inside the microemulsions, silver was taken as the metal because it is particularly efficient at absorbing and scattering light and shows different colors that indicate the size and the shape of the particle. To produce silver nanoparticles, the microemulsion containing silver nitrate was mixed with microemulsion containing hydrazine hydrate as a reducing agent. The formation of the silver nanoparticles was monitored using UV-Vis absorption spectroscopy. The UV-Vis spectroscopy revealed the formation of silver nanoparticles by exhibiting the typical surface plasmon absorption at 418-420 nm from the UV-Vis spectrum.

Three kinds of concentrations of Ag precursor were prepared to observe the growth profiles. As can be seen in Figure 6.2 (left), the growth profiles of Ag nanoparticles produced by each Ag concentration look quite similar and seem to follow the profile of the La Mer growth (right). It is interesting to see that in this case, all the Ag growth profiles have the same peak at about 15 minutes and a plateau at about 30 minutes. This may indicate that in the case of Ag nanoparticles, the self-nucleation ends at about 30 minutes and afterward the particles start to grow. Although the growth profile given

here refers to Ag nanoparticle formation, similar profiles might also be expected with other metals such as Pt, Pd, and Ru.

It is not by chance that Figure 6.3 shows a similar profile for the Ag growth profile although the catalytic activities of Pd and Ru catalysts prepared with different growth time are plotted. However, from this figure at least one can conclude that after 4 hr, the Pd and Ru nanoparticles are in the equilibrium stage of the size and shape.

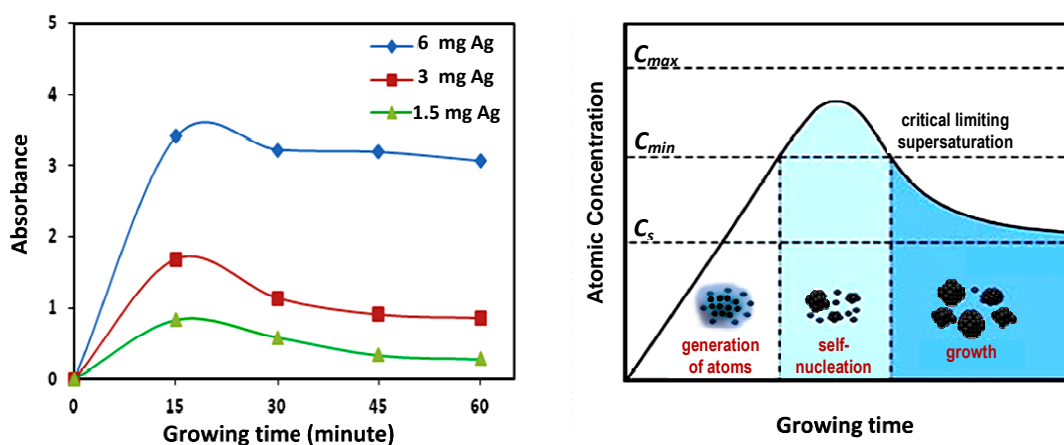


Figure 6.2 The growth profiles of Ag nanoparticles with different amounts of metal precursor in the microemulsion (left), which look like the profile of the La Mer model for nucleation and growth of particle in colloidal synthesis (right).

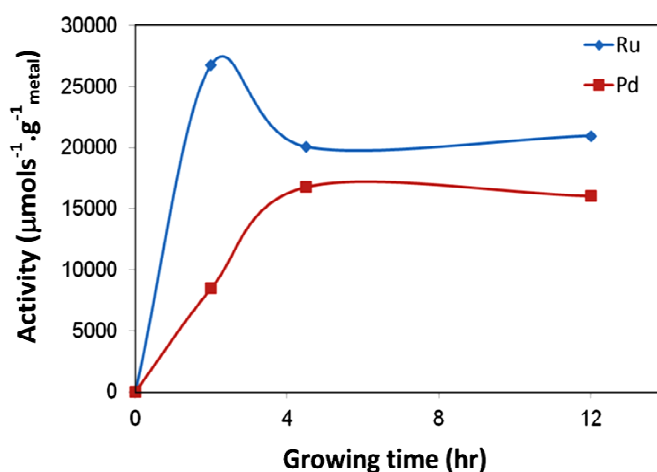


Figure 6.3 Activities of 0.1%-wt Pd/ Al_2O_3 and 0.04%-wt Ru/ Al_2O_3 prepared with different growing time. Both catalysts were tested in hydrogenation of methyl crotonate at 20 °C and 1.1 bar.

6.3 Effect of feeding rate

As already mentioned in Chapters two and five, the reducing rate may affect the activity of the produced catalyst. Song et al.⁷ reported that the addition rate of the precursor is important to control the size of metal nanocrystals. The reducing rate can also be slowed down by adding the metal precursor over a long period of time rather than dissolving all the precursors at the initial stage. Yang et al. obtained larger and more multifaceted Ag nanocrystals in the final stage by adding a mixture of Ag precursor over long time.⁸ Song et al.⁷ found that if the microemulsion containing the reducing agent was added all at once, small and irregular Pt particles were generated with the average size less than 4 nm. On the other hand, slow addition of the reducing agent over a period of 30 min led to polycrystalline particles larger than 13 nm. These experiments indicate that the particle size can be adjusted by controlling the concentration of seeds formed at the early stages of the reaction.

Figure 6.4 shows the effect of feeding rate of microemulsion containing reductant to the microemulsion containing metal precursor, i.e. by adding all at once (direct feeding) and slow feeding (0.2 ml/s), on the activity of the produced catalysts (Pd/SBA-15 and Pd/Al₂O₃). It is noted here that both catalysts were prepared with ascorbic acid as the reductant. Although both catalysts were tested with different hydrogenation reactions, they show the same tendency. The higher activity of Pt and Pd catalysts prepared by slow feeding rate of reductant indicates that the structures (size and shape) of the produced nanoparticles have more active sites than those of the direct feeding.

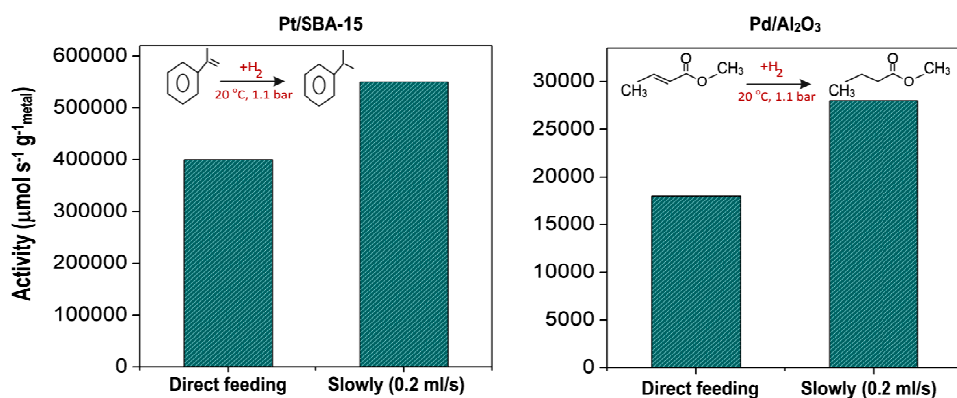


Figure 6.4 Differences in catalytic activity of Pt and Pd catalysts for the hydrogenation reactions of α methyl styrene (left) and methyl crotonate (right) caused by different feeding methods. Both catalysts were prepared with ascorbic acid as the reductant.

According to the classical nucleation theory, adding the reductant all at once will increase the formation rate of nuclei more significantly than the growth rate of the nanocrystals. As a result, large numbers of tiny nanoparticles with high surface area are formed in a short time. On the contrary, a lower supersaturation produced by longer feeding time leads to a smaller number of nuclei and a bigger particle size. Additionally, slow feeding of reductant causes the reaction conditions to be as if the metal precursor always has high concentration. A large number of metal nanoparticles will be formed at a higher concentration of metal precursor. As a result, the collision frequency increases significantly, which results in bigger particles

As already mentioned, from the literature and from the results shown in Chapter five, the structure of nanoparticles produced with ascorbic acid is anisotropic dendrite structure. Thus, the result shown here may also indicate that although the size of particles produced with slow feeding is bigger than those of direct feeding, their activities are still higher. To reemphasize again, in the case of anisotropic structure, the shape, up to a point, affects the activity more than the size of nanoparticles.

6.4 Effect of initial concentration of metal precursor

The effect of the initial concentration of metal precursor on the activity of the produced catalyst is also investigated. Chen et al.⁹ reported that the size of the produced metal nanoparticles is influenced by the initial concentration of metal precursor. Supported Pd and Ru metal catalysts were prepared with different concentrations of metal precursor in two and twelve hours of reducing time. The activity of the produced catalysts were then tested in hydrogenation of methyl crotonate as shown in Figure 6.5. The result shows that the activities of both catalysts decrease by increasing the metal precursor concentrations, which is in agreement with the results from Chen et al. In the case of Ag nanoparticles, Zhang et al.¹⁰ reported that at a higher concentration, if the concentration of AgNO₃ increases, the mean diameter of Ag nanoparticles also increases because the silver nanoparticles begin to aggregate and form into large particles.

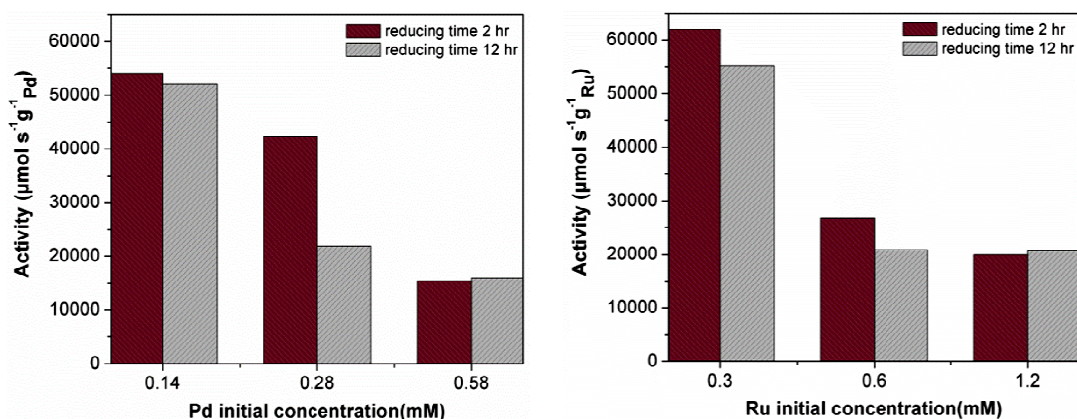


Figure 6.5 Activities of supported metal catalysts prepared with different initial metal concentrations and with slow feeding rate of reductant. Left : Pd/Al₂O₃ prepared with AA as reductant. Right : Ru/Al₂O₃ prepared with hydrazine as reductant. Both catalysts were tested in hydrogenation of methyl crotonate at 20 °C and 1.1 bar.

The concentrations of the metal precursor affect the reduction rate. The rates of both nucleation and growth are determined mainly by the probabilities of the collisions between two atoms, between one atom and a nucleus, and between two nuclei. Therefore, when the metal precursor concentration is low, the formation rate of metal nuclei is higher than the growth rate of metal nanocrystals. There are amounts of small nanoparticles formed with high surface area in a short time. These smaller particles can absorb surfactant molecules onto their surfaces to prevent them from aggregation, so it is thus favorable to form fine nanoparticles. On the contrary, when the metal concentration is high, the reduction rate of metal ions increases and a large number of nanocrystals are thus formed. As a result, the collision frequency among them increases significantly. The small nanoparticles tend to aggregate to form larger particles.

It is interesting to see that, as described in subchapter 6.3 the bigger particles resulting from a slow feeding rate have higher activities. In the case of the bigger particles formed due to higher concentration, lower activities are observed. This indicates that, in the former case, the slow feeding promotes slow reduction rate thus induces primarily the (anisotropic) structure, whereas in the later case, the higher concentration induces the collision between particles which results in bigger particles but more isotropic structure.

6.5 Effect of the zeta potential to the deposition yield and the activity

As is generally known, a charged particle will attract ions of opposite charge. The metal nanoparticles that are produced by growth of the nuclei have a certain charge on the surface. The metal nanoparticles form a strongly bound layer close to the surface. The ions which are further away from the core metal particle make up a diffuse layer, more loosely bound to the particle (Figure 6.6). Within this diffuse layer is a theoretical boundary, in which the particle and its associated ions act as a single entity, diffusing through the dispersion together. The plane at this boundary is known as the surface of hydrodynamic shear, or the slipping plane. The potential at this boundary is known as the zeta potential.

Not only the metal nanoparticles, but also the support material that is used in the deposition process has a zeta potential. Therefore it is important to observe the effect of the zeta potential of both materials in the deposition yield and the activity of the produced catalysts. Table 6.1 presents the experimentally measured zeta potential of the support materials and metal nanoparticles that are used in this work.

Table 6.1 Zeta potentials of the support materials and metal nanoparticles

Support Material	ζ -Potential (mV)	Metal nanoparticle	ζ -Potential (mV)
acidic- Al_2O_3	+ 45	Ag	-50
neutral- Al_2O_3	+ 20	Pt	-24
basic- Al_2O_3	+ 10	Pd	+25
SBA-15	-20	Ru	+57

The zeta potential may have played a role in determining the successful deposition of the silver (Ag) nanoparticles. Figure 6.6 illustrates the deposition of Ag nanoparticles on acidic alumina. Experimentally measured, the zeta potential of the Ag nanoparticles is around -50 mV. From the three aluminium oxide supports, the acid one has the most positive zeta potential of around +45 mV. This value is followed by the neutral Al_2O_3 at

around +40 mV and lastly by the base support at around +10 mV. From the illustration in Figure 6.6, one can predict that the particle with the most negative zeta potential is adsorbed the strongest at the support with the most positive zeta potential. As the zeta potential value of the acidic Al_2O_3 is the most positive, the Ag nanoparticles are naturally attracted to the positive surface potential of the support. As a result, the yield percentage of the Ag on acidic Al_2O_3 is the highest in comparison to the other aluminium oxide supports (see right-hand side of Figure 6.7), although only a slight difference with regards to the yield percentage of the three supports is observed. This may indicate that the high negative charge of Ag nanoparticles is still attractive to the positively charged material even for the mildly charged one such as basic alumina. Therefore, it can be concluded that aluminum oxide is a very suitable catalyst support for Ag nanoparticles, especially the acidic Al_2O_3 .

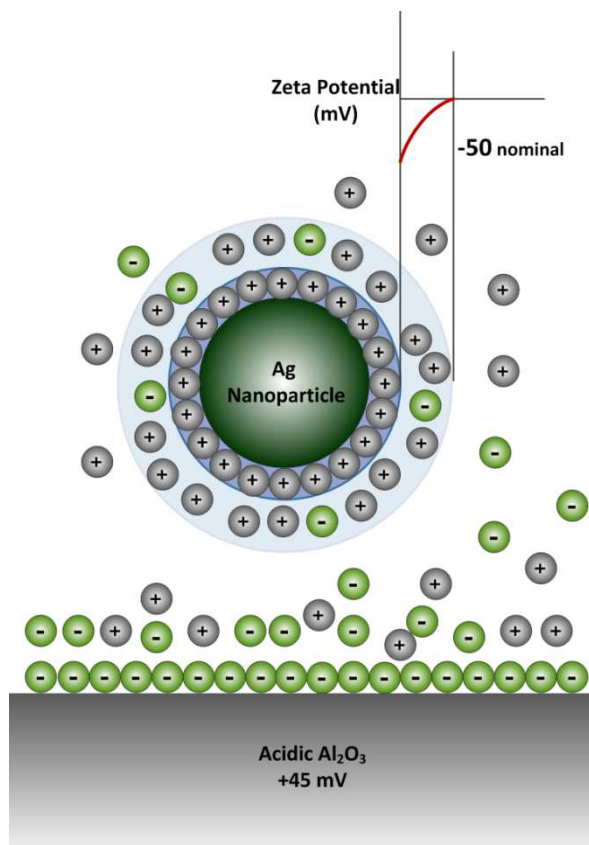


Figure 6.6 Schematic illustration of Ag nanoparticle deposition onto acidic alumina. Ions adsorb onto the surface of the Ag nanoparticles creating an electrical double layer. The potential in the second layer is called zeta potential.

In order to increase the % loading of the metal on the support material, the amount of the metal in the microemulsions is increased while the amount of the support is fixed. Figure 6.8 shows the profiles of % loading of Ag, Pd, Ru and Pt on 2000 mg of basic alumina versus the amount of metal in the microemulsions. Among other metals, Ag nanoparticles show the highest slope (upper left) followed by Pd, Ru and Pt, respectively. The slope indicates the driving force or affinity which can be related to the value of the zeta potential. As can be seen in Table 6.1, the zeta potential of basic alumina is +10 mV, whereas Ag, Pd, Ru, Pt are -50, -25, +57 and +24, respectively.

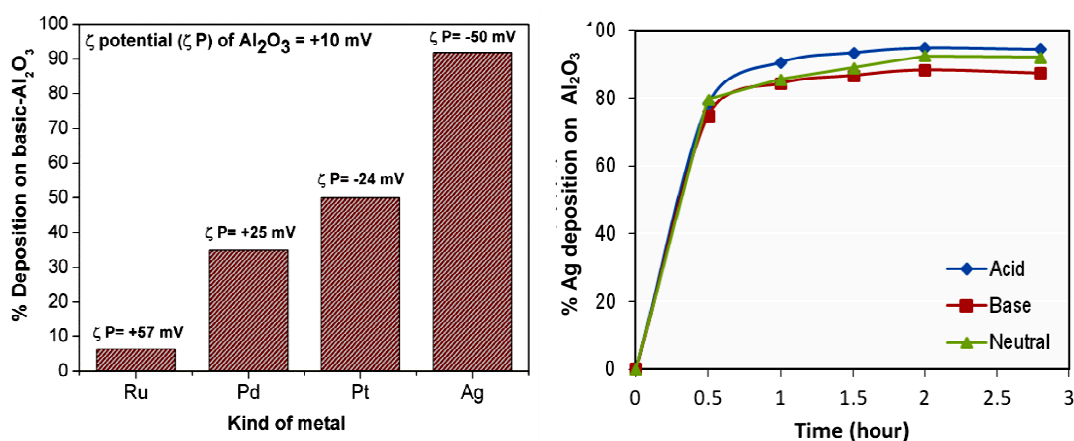


Figure 6.7 Left: Deposition percentage of different metals on basic Al₂O₃ with thermo-destabilization method. The amount of metal precursor prepared in each microemulsion system is 6 mg. Right: The yield of Ag deposition on acidic, basic and neutral alumina. The high deposition yield of Ag to all the supports is because of the big difference of the zeta potentials between Ag (-50 mV) and acidic, neutral and basic alumina (+45, +40, +10 mV, respectively).

It is observed that the zeta potential indirectly affects the activity of the produced catalyst, as shown in Figure 6.9. It is interesting to see that although Pd and Ru have the same charge like the supporting alumina, a deposition still can take place. This can be attributed to the van der Waals interaction. The activities of supported Ru catalysts are higher than Pd catalysts (Figure 6.9) most probably because Ru catalysts have a better dispersion than Pd catalysts. Ru is more positively charged (+57 mV) than Pd (+25 mV), whereas the zeta potential of acidic, neutral and basic Al₂O₃ are +45, +40 and +10 mV, respectively. The more positively charged support particles are more likely to interact with the less positively charged metal particles which can result in

better dispersion. Therefore, in this case, the dispersion of Ru is better on basic Al_2O_3 followed by neutral Al_2O_3 and acid Al_2O_3 . This result is opposite to the activity of Pt particles in hydrogenation of α -methyl styrene (see the inset). Because Pt has a zeta potential of -24 mV, this results in an activity decrease of Pt catalysts with the support material ranking from acidic to basic Al_2O_3 .

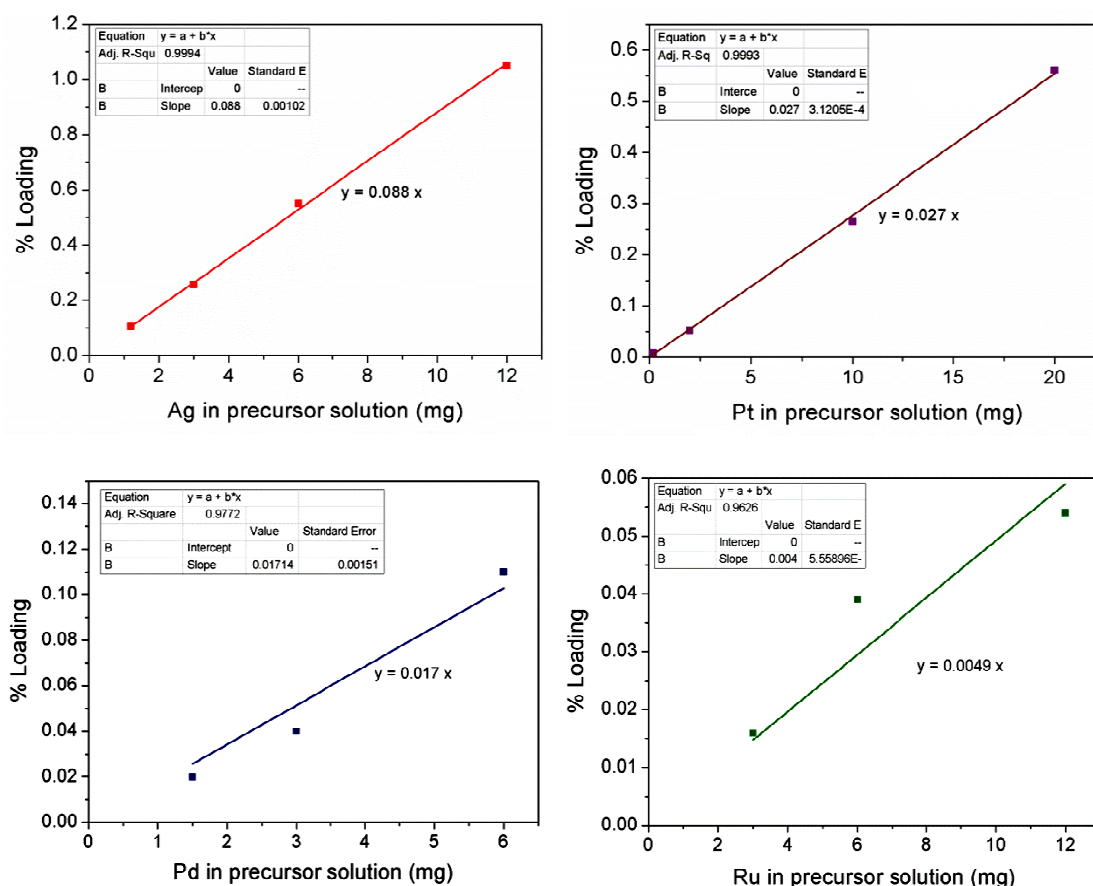


Figure 6.8 Loading of different metal catalysts on basic alumina as a function of the amount (mg) of corresponding metal in the precursor solutions. The slope shown in each profile indicates the affinity of metal particles to the support material.

6.6 Effect of the support type on the activity

To confirm the results that have been presented in Chapters four and five concerning the effect of the support type on the activity of supported Pt catalysts, here this matter related to supported Pd and Ru catalysts will be discussed. As we can see in Figure

6.10, the activities of Pd and Ru catalysts in methyl crotonate hydrogenation are higher when supported on MCM-41 followed by SBA-15 and Al_2O_3 . The most probable reason for this account is the structure of the support. Figure 6.11 and 6.12 show clearly the structure of the supported Pd and Ru catalysts by the SEM images. The structure of MCM-41 seems to promote better dispersion of both Pd and Ru catalysts compared to SBA-15 and Al_2O_3 . Not only the support structure, if we now compare the zeta potentials of MCM-41, SBA-15 and Al_2O_3 which are -20, -25 and +20 mV, respectively (on average), whereas the zeta potentials of Pd and Ru are +25 and +57 mV, we can conclude that both metals are not well dispersed on alumina.

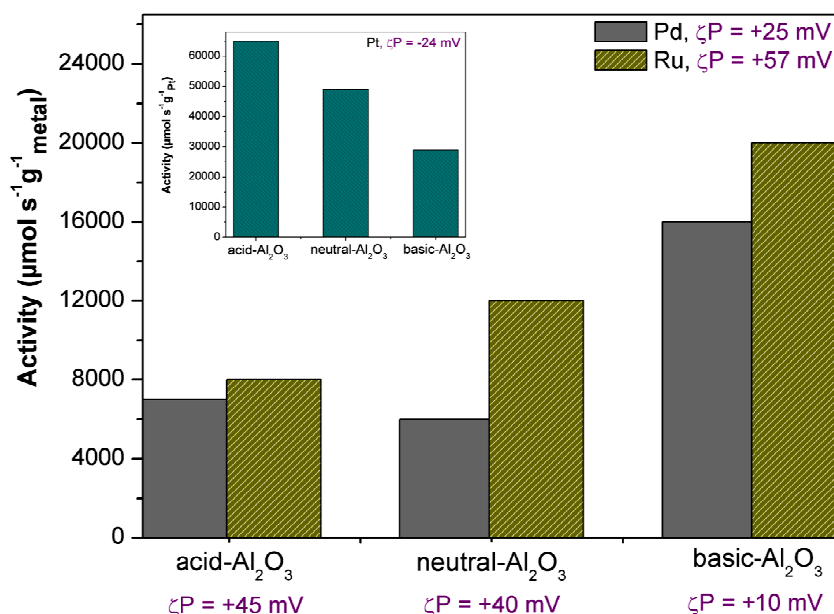


Figure 6.9 Activities of Pd and Ru catalysts supported on different acidity of Al_2O_3 in hydrogenation of methyl crotonate. The inset is activities of Pt catalyst supported on different acidity of Al_2O_3 in hydrogenation of α -methyl styrene. The opposite trend of activities between Pt catalyst and Pd and Ru catalysts is because of the the different value of zeta potential.

6.7 Effect of pre-calcination of the support

Another possible method to improve the deposition yield and activity is to preheat the support material (pre-calcinations). The support was preheated at 500 °C for 2 hr with the intention of removing any gas or moisture inside of the support pores so that the

particles can get into the pores without barrier. Here, Pt and Pd nanoparticles were synthesized using ascorbic acid as the reductant and deposited on basic- Al_2O_3 , either with or without pre-calcinations. Interestingly, as we can see in Table 6.2, there is no significant difference on yield of deposition of both metals on the support, with and without pre-calcinations. However, in the case of activity, only the supported Pt catalysts show substantial difference, with and without pre-calcinations of the support. This might be attributed to the metal dispersion on the support with the correlation to the value of the zeta potential of the involved materials.

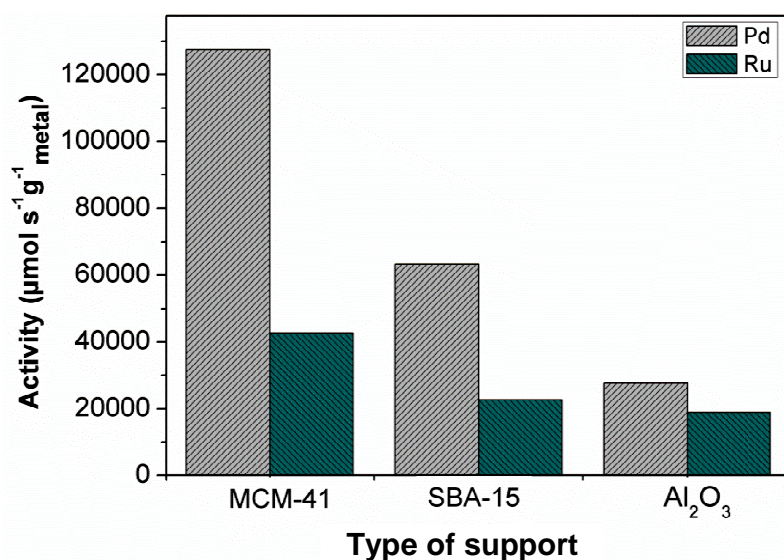


Figure 6.10 Activities of Pd and Ru catalysts supported on different supports in hydrogenation of methyl crotonate at 20 °C and 1.1 bar.

Because the value of the ζ -potential of Pd nanoparticles ($= +25$ mV) is not so much different to the basic- Al_2O_3 ($= +10$ mV), the pre-calcination has no significant effect on the dispersion of nanoparticles on the support. In fact, they both are positively charged materials. On the contrary, considering the contrast value of the ζ -potential of Pt nanoparticles ($= -24$ mV) with the basic- Al_2O_3 , the pre-calcination gives considerable effect to the dispersion of nanoparticles on the support.

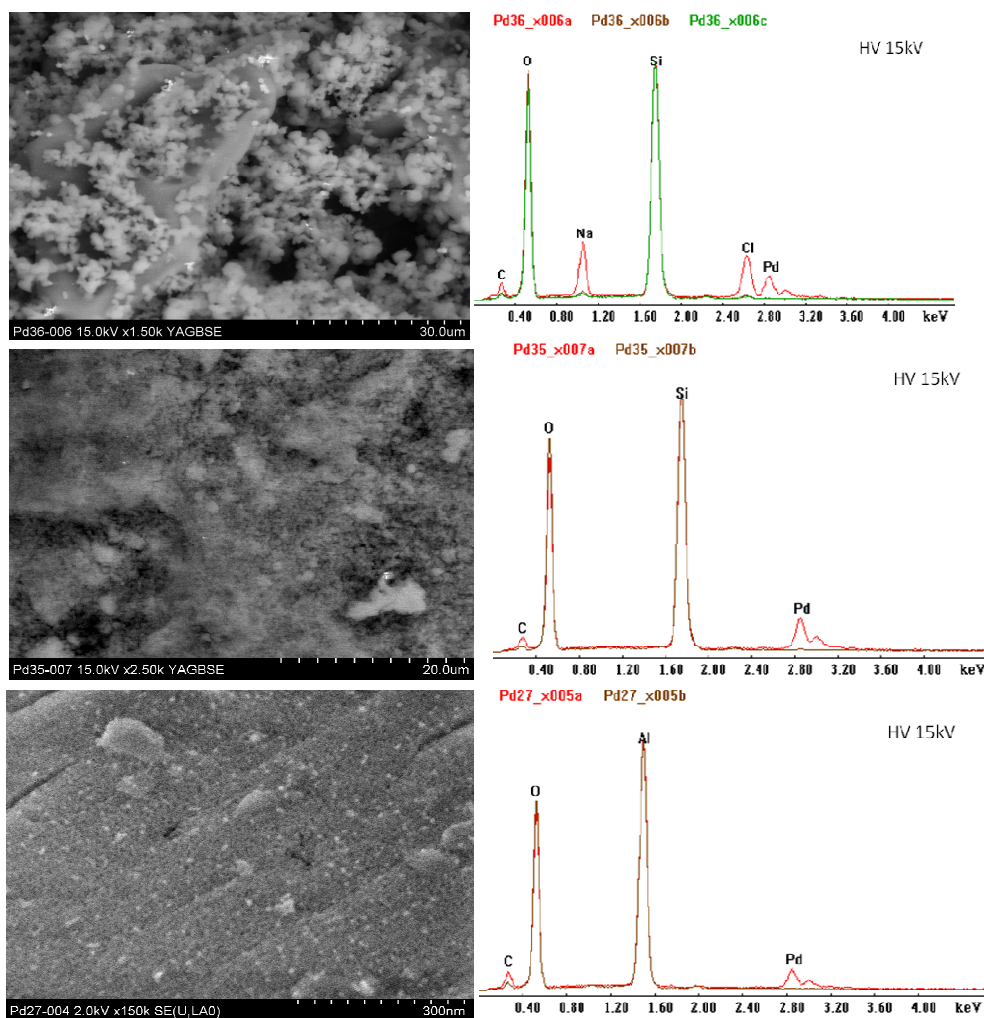


Figure 6.11 SEM images of supported Pd catalysts (left) and the corresponding EDX (right): Pd/MCM-41 (top), Pd/SBA-15 (middle), Pd/Al₂O₃ (bottom).

This may also indicate that the pre-calcination process causes the Al₂O₃ to lose its –OH group to such an extent that it becomes more acidic. Miller et al. reported that increasing the alumina pre-calcination temperature results in a decrease in the intensity of the hydroxyl bands, although a significant number of hydroxyl bands remain even after calcination at 700°C. They found that in the alumina catalysts, the number of surface hydroxyl groups was varied by changing the support precalcination temperature. As the calcinations temperature increased, the number of hydroxyl groups decreased as evidenced by infrared spectroscopy.¹¹

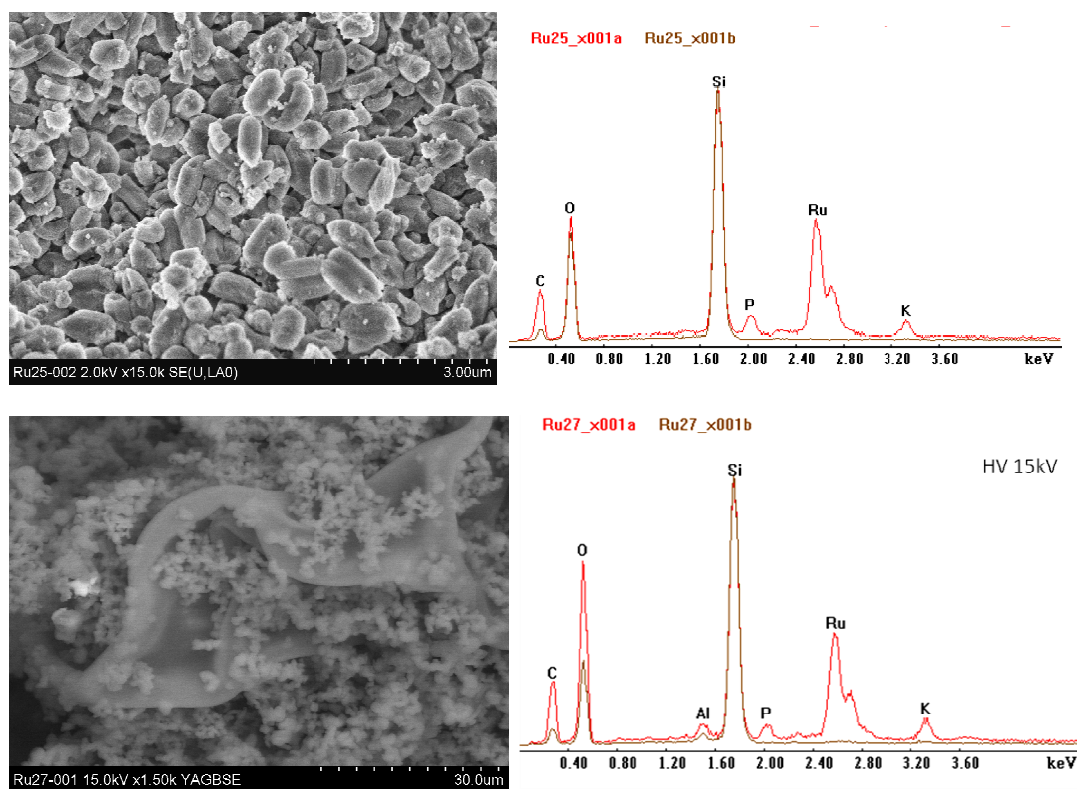


Figure 6.12 SEM images of supported Ru catalysts (left) and the corresponding EDX (right): Ru/MCM-41 (top) and Ru/SBA-15 (bottom).

The acidic Pt nanoparticles (ζ -potential = -24 mV) are more stable before attaching to the acidic support which results in less agglomeration on the support, thus leading to higher activity. In the case of supported Pd catalysts, although there is not so much difference in the activity (Table 6.2), the alkalinity of Pd nanoparticles (ζ -potential = +25 mV) causes them to be less stable before attaching to the more acidic support. As a result, it produces Pd agglomeration on the support, thus leading to the lower activity. As can be seen in Figure 6.13, the dispersion of the Pd particles on basic alumina without precalcination is better than those on the precalcinated one. The few particles on the precalcinated support indicate that the dispersion is not uniform.

The same percentage of deposition for with and without precalcination (Table 6.2) may lead to the conclusion that the loss of some OH groups of the support does not influence the adsorption of particles, but rather the changing of pH, which in turn,

affects the dispersion. Therefore, this is not the same with phenomena that happen in the impregnation technique which generally show the effect of OH groups on either the deposition yield or the dispersion.

Table 6.2 Effect of pre-calcination of the support on the yield of deposition and activity. Both supported Pt and Pd catalysts were prepared with ascorbic acid as the reductant.

Pretreatment of support (basic-Al ₂ O ₃) ¹⁾	Pd/ basic-Al ₂ O ₃ ²⁾		Pt/basic-Al ₂ O ₃ ³⁾	
	Deposition yield (%)	Activity ⁴⁾ (μmol.s ⁻¹ .g _{Pd} ⁻¹)	Deposition yield (%)	Activity ⁵⁾ (μmol.s ⁻¹ .g _{Pt} ⁻¹)
Without pre-calcination	35.3	13000	36.8	6000
Pre-calcination (500 °C, 2 hr)	35.7	9000	33.9	29000

¹⁾ ζ-potential of basic Al₂O₃ = +10 mV

²⁾ ζ-potential of Pd nanoparticles = +25 mV

³⁾ ζ-potential of Pt nanoparticles = -24 mV

⁴⁾ tested in α-methyl styrene hydrogenation

⁵⁾ tested in methyl crotonate hydrogenation

6.8 The activity of supported metal catalysts in hydrogenation of AMS

α-Methyl styrene (AMS) hydrogenation is a typical industrial process that involves hydrogenation of liquids of low volatility. It proceeds with a considerable rate even at low temperature and hydrogen pressure. This is the reason that it is frequently used to investigate mass transfer limitations in three-phase catalytic reactors.¹²⁻¹⁴ The reaction is mildly exothermic ($\Delta H = -109 \text{ kJ.mol}^{-1}$).¹⁵

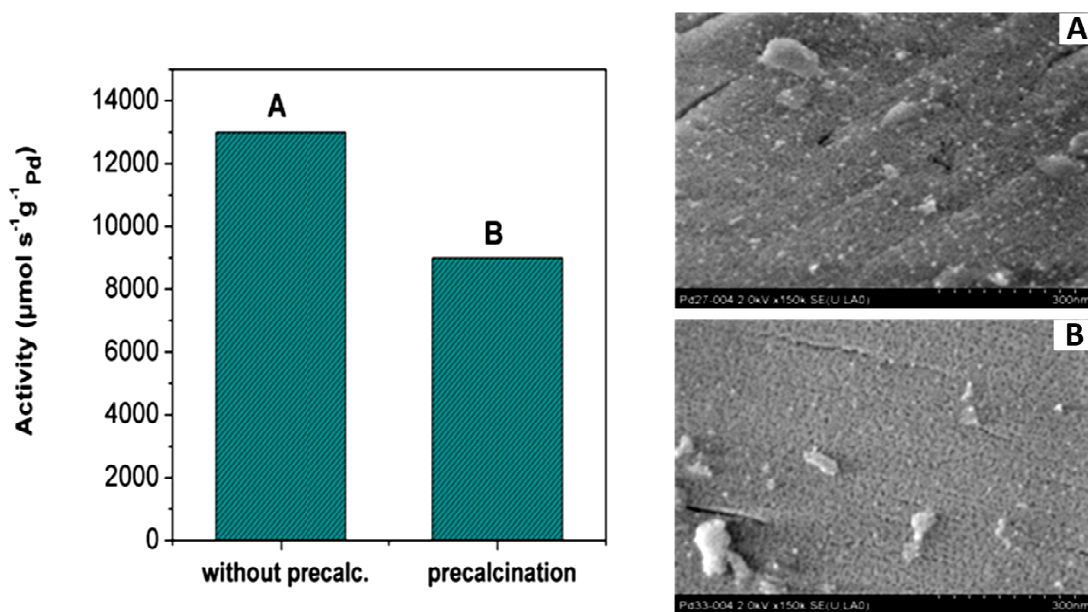


Figure 6.13 Effect of precalcinations on the catalytic activity of Pd particles supported on basic alumina and the corresponding SEM images.

In this work, supported catalysts with different metals have been prepared with thermo-destabilization of microemulsions. Among all the produced catalysts, the best performing in hydrogenation of AMS from each kind of supported metal was taken, in order to compare their activity in that reaction. The result shows that supported Pd catalyst is more active than other supported metal catalysts as shown in Figure 6.13. In case of Pd and Pt catalysts, the result is in agreement with Schwarze et.al¹⁶ who showed that Pd catalyst is more active than Pt catalyst. In our case, both supported Pd and Pt catalysts were prepared with ascorbic acid as the reductant, therefore it is expected that the structure of both metal catalysts are anisotropic. Although both catalysts are anisotropic, their morphologies are somewhat different as shown by TEM images in Figure 6.15. The images of both metals are taken in the absence of surfactant, thus it can be said that they are in the equilibrium state (no more change). From the images shown we can see that the Pt particles have more branches than Pd particles, however the activity is still lower. Therefore, it can be concluded that in this case the type of metal used as the catalyst has a stronger influence than the structure of the metal catalyst.

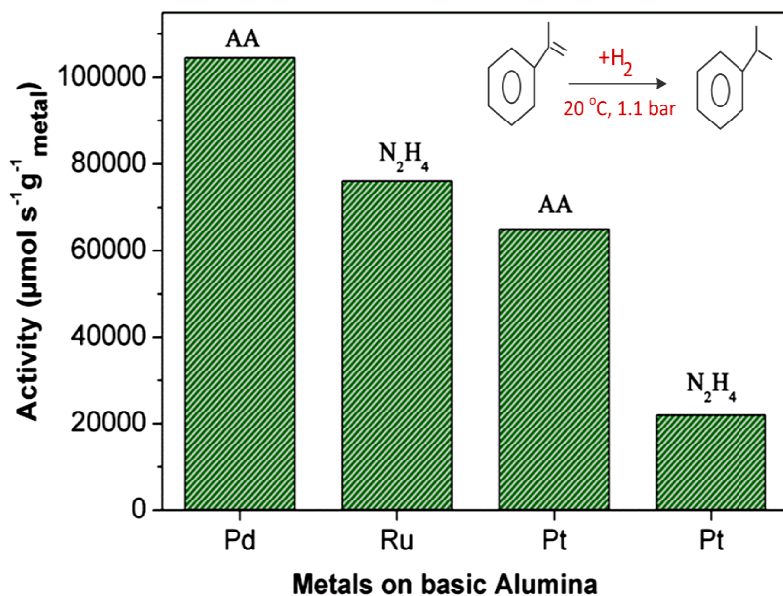


Figure 6.14 Activities of different supported metal catalysts prepared with different reducing agents (N_2H_4 and AA), in hydrogenation of α -methyl styrene.

6.9 The activities of supported metal catalysts in hydrogenation of Levulinic Acid

One of the challenging reactions related to the renewable platform chemicals is the hydrogenation of levulinic acid (LA). The selective reduction of levulinic acid to γ -Valerolactone (GVL) is a very interesting and substantial reaction because GVL can be used as renewable fuel, solvent, and feedstock for the production of alkenes and transportation fuels, especially when considering that in the future crude oil and natural gas resources will be depleted.¹⁷

Thus far, LA hydrogenation has been carried out at relatively high reaction temperature under high pressure, generally with Ruthenium-based catalysts. For example Upare et al.¹⁸ produced GVL (100% selectivity) at 100% LA conversion up to 240 h (10 days) at 265 °C and pressure up to 25 bar using 5 wt.% Ru@C. Tukacs et al. conducted the LA hydrogenation to GVL at 140°C and 100 bar.¹⁷ Bozell et al.¹⁹ produced 95% conversion of LA to GVL at 200°C and 40 bar with 1% Pt@TiO₂. In the

literature, many have reported that in LA hydrogenation, Ru catalysts are more active than other metal catalysts.^{17,18,20,21}

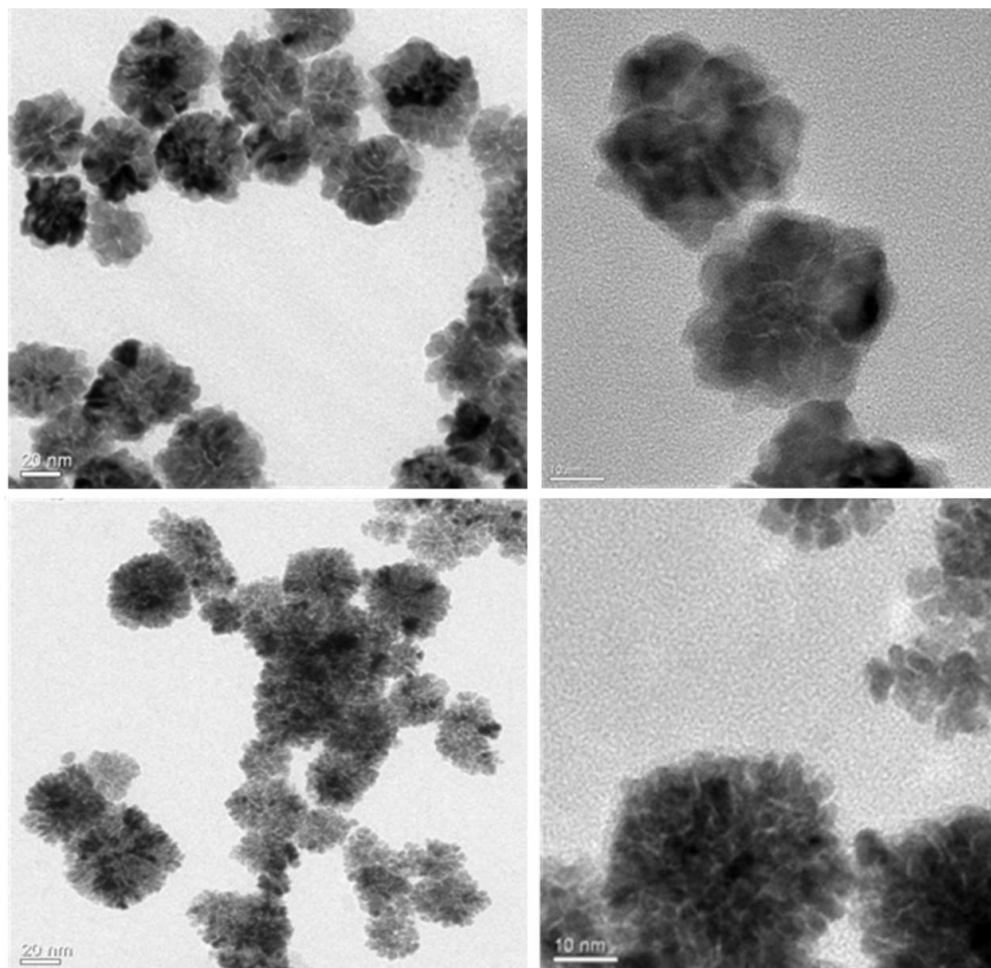


Figure 6.15 Morphology of Pd (upper) and Pt (bottom) nanoparticles produced using ascorbic acid as the reductant in the absence of surfactant.

In this work, one of the produced Ru catalysts reaches LA conversion of 74% in 18 hr while the Pt catalyst reaches 78% in 46 hr (both are tested at 70 °C and 1,3 bar). As a comparison, especially in matter of the reaction conditions, the Ru catalyst produced by Tukacs et al. reaches LA conversion of 15% in 110 min at 140 °C and 5 bar, whereas the Ru and Pt catalyst from this work, in 110 min can reach 19% and 11% respectively at 70 °C and 1,3 bar. We note that the synthesized catalysts are not yet optimized. Therefore, we would conclude that the method that is used in this work has potential to produce very active metal catalysts for LA hydrogenation.

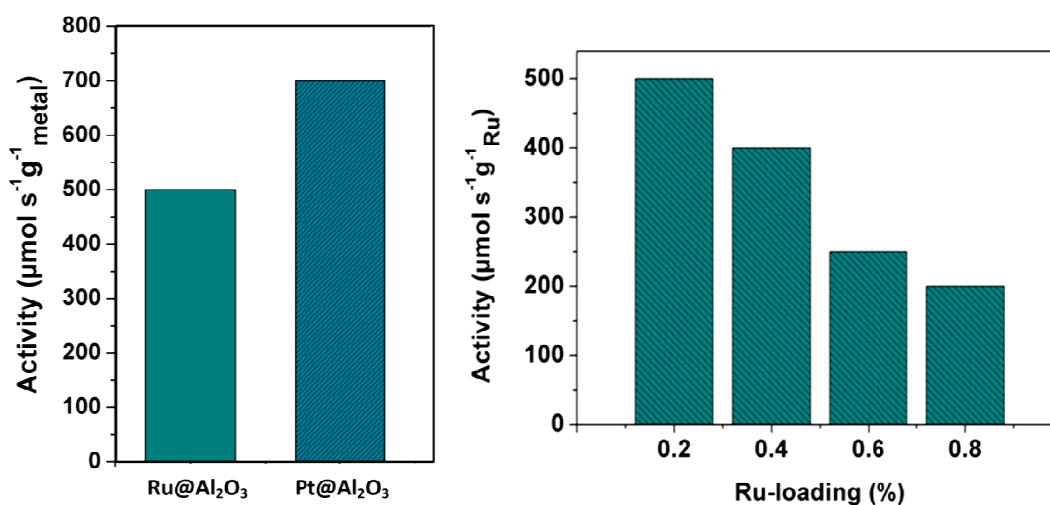


Figure 6.16 Left: Activities of 0.2% Ru@Al₂O₃ and 0.1 % Pt@Al₂O₃ catalysts (in LA hydrogenation) prepared with N₂H₄ and AA as reductants respectively. Right: Activities of different loadings of Ru/Al₂O₃ in LA hydrogenation. The reaction was conducted at 70 °C and 1.3 bar.

It is interesting to see in Figure 6.16 that the activity of 0.1% Pt@Al₂O₃ is more active in LA hydrogenation than 0.2% Ru@Al₂O₃. This can be attributed to either the crystal structures or the dispersions of the catalysts on the support. Unfortunately, there is no evidence such as TEM images to prove the first argument. However, if we see the result in Figure 6.15 (right), increasing the loadings of the Ru catalysts leads to the decreasing of the activities. This may signify that the dispersion of the catalyst with the lower loadings is better than the higher loadings. Nonetheless, further and more comprehensive studies need to be done because those catalysts have not yet been optimized.

6.9 Conclusion

The supported Ag, Pd and Ru catalysts have been prepared via thermo-destabilization of microemulsions. Therefore, this method can be used to prepare not only supported Pt catalysts (Chapters 5 and 6) but also different supported metal catalysts. Although they were prepared with the same procedure, their features are different from one to another. For example, because Ag nanoparticles have the most negative surface charge (-50 mV) compared to the three others, they can be deposited easily to the acidic,

neutral and basic alumina supports which have positive surface charges (+45, +40, +10 mV, respectively).

For each supported metal catalyst, the effect of growing time of the nanoparticles on the catalytic activity has different profile from one to another. However, the effect of the feeding rate of the microemulsion containing the reductant to the microemulsion containing the metal precursor on the activity of the resulting supported catalyst seems to have the same tendency for each type of metal, as well as the effect of initial concentration of metal precursor. The type of support material as well as its zeta potential and its acidity also influence the activity of the resulting supported metal catalyst.

The supported Pt, Ag, Pd and Ru catalysts which are presented in this chapter and in the previous chapters have not yet been optimized. Even so, the performance of the supported Pt and Ru catalysts in challenging reactions such as levulinic acid hydrogenation is better than that of catalysts prepared by other methods and show potential for further improvement.

References

1. R. Libanori, R. O. da Silva, C. Ribeiro, P. Ari-Gur, and E. R. Leite, *J Nanosci Nanotechnol*, 2012, **12**, 4678–4684.
2. R. Y. Parapat, M. Wijaya, M. Schwarze, S. Selve, M. Willinger, and R. Schomäcker, *Nanoscale*, 2012, **5**, 796–805.
3. T. Premkumar, K. Lee, and K. E. Geckeler, *Nanoscale Research Letters*, 2011, **6**, 547.
4. F. Si, L. Ma, C. Liu, X. Zhang, and W. Xing, *RSC Adv.*, 2011, **2**, 401–403.
5. H. Lee, C. Kim, S. Yang, J. W. Han, and J. Kim, *Catal Surv Asia*, 2012, **16**, 14–27.
6. J. Ren and R. D. Tilley, *J. Am. Chem. Soc.*, 2007, **129**, 3287–3291.
7. H. Song, F. Kim, S. Connor, G. A. Somorjai, and P. Yang, *The Journal of Physical Chemistry B*, 2005, **109**, 188–193.
8. T. Yao, S. Liu, Z. Sun, Y. Li, S. He, H. Cheng, Y. Xie, Q. Liu, Y. Jiang, Z. Wu, Z. Pan, W. Yan, and S. Wei, *J. Am. Chem. Soc.*, 2012, **134**, 9410–9416.
9. D.-H. Chen and C.-J. Chen, *J. Mater. Chem.*, 2002, **12**, 1557–1562.

10. W. Zhang, X. Qiao, and J. Chen, *Materials Science and Engineering: B*, 2007, **142**, 1–15.
11. J. T. Miller, M. Schreier, A. J. Kropf, and J. R. Regalbuto, *J. Catal.*, 2004, **225**, 203–212.
12. D. L. Johnson, H. Saito, J. D. Polejes, and O. A. Hougen, *AIChE Journal*, 1957, **3**, 411–417.
13. V. Meille, C. de Bellefon, and D. Schweich, *Ind. Eng. Chem. Res.*, 2002, **41**, 1711–1715.
14. C. N. Satterfield, A. A. Pelossof, and T. K. Sherwood, *AIChE Journal*, 1969, **15**, 226–234.
15. P. C. Watson and M. P. Harold, *AIChE Journal*, 1993, **39**, 989–1006.
16. M. Schwarze, J. Keilitz, S. Nowag, R. Y. Parapat, R. Haag, and R. Schomäcker, *Langmuir*, 2011, **27**, 6511–6518.
17. J. M. Tukacs, D. Király, A. Strádi, G. Novodarszki, Z. Eke, G. Dibó, T. Kégl, and L. T. Mika, *Green Chem.*, 2012, **14**, 2057–2065.
18. P. P. Upare, J.-M. Lee, D. W. Hwang, S. B. Halligudi, Y. K. Hwang, and J.-S. Chang, *Journal of Industrial and Engineering Chemistry*, 2011, **17**, 287–292.
19. J. J. Bozell, *Science*, 2010, **329**, 522–523.
20. J. J. Bozell, L. Moens, D. . Elliott, Y. Wang, G. . Neuenschwander, S. . Fitzpatrick, R. . Bilski, and J. . Jarnefeld, *Resources, Conservation and Recycling*, 2000, **28**, 227–239.
21. M. Chalid, H. J. Heeres, and A. A. Broekhuis, *Procedia Chemistry*, 2012, **4**, 260–267.

Chapter 7

Conclusion

A new method to synthesize supported metal catalysts with controlled size and shape has been developed, namely the thermo-destabilization of microemulsions. The method appears to be promising for the preparation of highly active and stable supported-metal catalysts. It involves very simple operations, low preparation temperature, and can produce well-dispersed metal particles (with narrow particle size distribution) on the support material.

In controlling the size and shape of the (platinum) nanoparticles, both, surfactant and reducing agent play an important role. Using a strong reducing agent such as hydrazine causes small particle sizes because of the fast growth, and the shape is governed by the head group of the surfactant (Triton X-100). When using a weak reducing agent like ascorbic acid, the size is bigger because of the slow growth and the shape is no longer directed by the surfactant but by the reducing agent. In this case, anisotropic growth occurs which results in irregular structures.

Changing to the anisotropic structure of the nanoparticles can substantially enhance the catalytic activity. The thermodynamic equilibrium shape of Pt particles produced when using hydrazine as the reductant is a truncated octahedron composed of the lowest-index crystal planes $\{111\}$ and $\{100\}$, which are known to be the least active. The irregular polycrystalline structure produced with ascorbic acid, Pt nanodendrite, is composed of the higher index crystal planes especially $\{311\}$, $\{331\}$ and $\{511\}$. The

high index planes exhibit much higher reactivity because of the low coordination number and high density of atomic steps, edges and kinks, which usually serve as active sites for breaking chemical bonds.

After testing with the hydrogenation of α -methyl styrene (AMS), the isotropic Pt-catalyst (2.5 nm) showed higher activity (6 times higher) than commercial ones. The performance of the catalyst is optimized by keeping the small size but changing the shape to anisotropically structured Pt nanocrystals. The catalytic activity of the anisotropic structure is found to be more active (3-4 times) than those of isotropic ones although the size is bigger (approx. 5 nm bigger). Therefore, the strategy of making smaller and smaller particles does not always lead to a better catalyst.

Other primary factors that affect the size of nanoparticles prepared via the microemulsions are the molar ratio of water to surfactant that adjust the size of the water droplets, initial molar ratio of metal and reducing agent, growing time, the kind of metal (salt) precursor and the feeding rate.

The dispersion of nanoparticles on the support is also responsible for their activity. The most important factor that influences the particle dispersion is the zeta potential of particle and support material. Choosing the support material with a suitable zeta potential is very important, otherwise the designing work of nanoparticles become ineffective. A support material which can provide a good particle dispersion and interaction is one that has an opposite charge compared to the particles. Other parameters that influence the interaction of the support with the nanoparticles released from the water droplets during the deposition process are the structure (well ordered or not) and the surface area.

Alumina is very suitable to support Ag and Pt nanoparticles because it has an opposite zeta potential ($> +10$ mV) to Ag particles (-50 mV) and Pt particles (-25 mV). In the case of SBA-15, although it has a high surface area (800 m²/g) and well ordered structure, it is difficult to support the Pt particles because the zeta potential of SBA-15 is similar (-20 mV) to the Pt particle, even more when the particles are bigger than the support pore size.

Another factor that influences the dispersion of particles is preheating of the support material (pre-calcinations). The support was preheated at 500 °C for 2 hr with the intention of removing any gas or moisture inside of the support pores so that the particles could get into the pores without barrier. Pre-calcination causes the support material to lose its –OH group to such an extent that it becomes more acidic. The loss of some OH groups of the support influence the pH, which in turn, affects the dispersion.

A parameter that can influence the size and the shape of the final supported metal catalyst is the calcination temperature. The optimum calcination temperature for the materials studied in this work is 300 °C which is sufficient to ensure the removal of the remaining surfactant from the synthesis process without causing sintering of the nanoparticles.

Preparations of other supported metal nanoparticles such as Pd, Ru and Ag catalysts were also studied to elucidate the versatility of the recipe. Pd nanodendrite with highly branched structure was produced as well by means of AA as the reducing agent. Although the Pt and Pd nanodendrites were prepared with the same synthesis procedure and under the same conditions, their structures are somewhat different. Metal nanoparticles with a lower degree of agglomeration during the deposition process have been produced under the experimental conditions optimized in this study. Most of the particles are deposited on the outer surface of the support. Engineering aspects for better control during the deposition process would be advantageous for further improvement. The insignificant difference of activity (< 1%) of produced catalyst from different batches indicates that this method is well adaptable and reproducible.

In most cases for the catalytic testing with the hydrogenation of either AMS or methyl crotonate, Pd nanodendrites exhibit higher activity than Pt nanodendrites. Testing the produced Ru and Pt catalysts with a more challenging reaction such as hydrogenation of levulinic acid shows that their performances are better (approx. 20% higher conversion) than those prepared by other researchers, even at milder reaction conditions. The performance of the Ru and Pt catalysts in hydrogenation of levulinic acid still shows potential to be increased and deserves to be further investigated.

Appendix

Appendix A

Physical and Chemical Properties

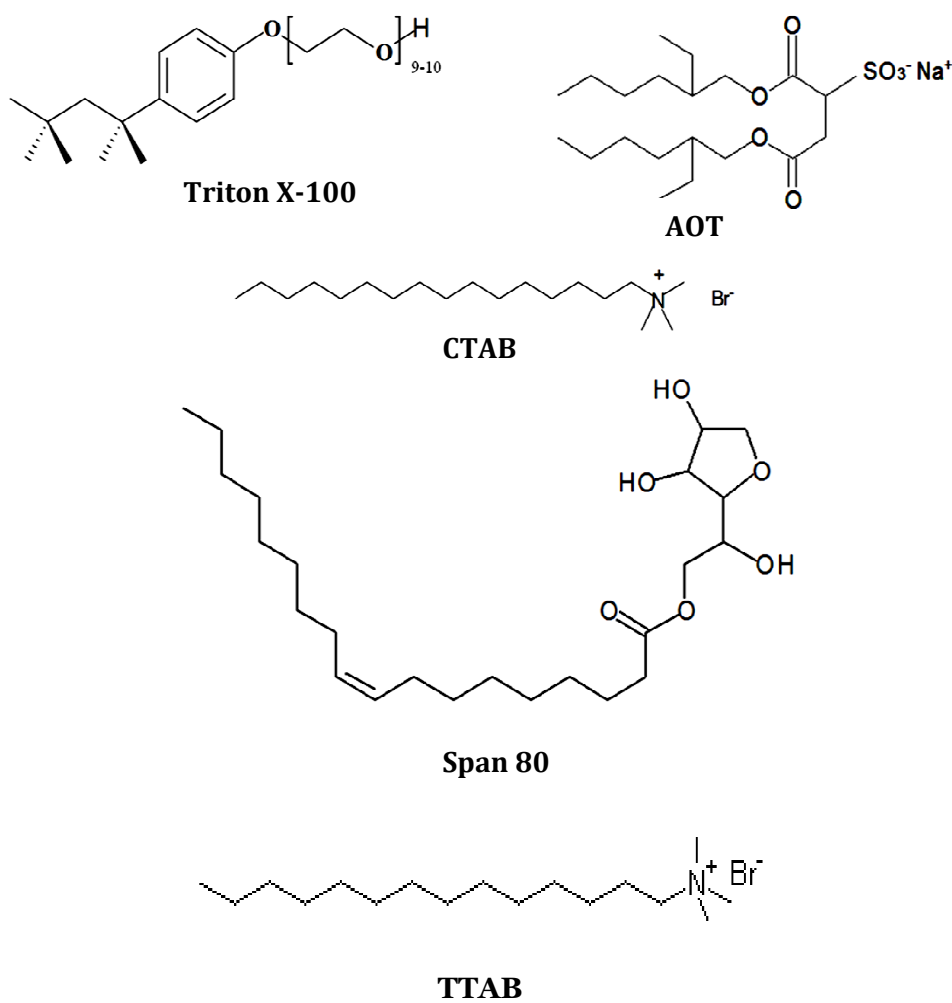


Figure A.1 Structure of the surfactants that are used in the experiments

Table A.1 Properties of support materials that are used in the experiments

Name	Particle size (μm)	Surface area [m^2/g]
$\gamma\text{-Al}_2\text{O}_3$ (neutral)	~ 200	155-200
$\gamma\text{-Al}_2\text{O}_3$ (base)	~ 200	155-200
$\gamma\text{-Al}_2\text{O}_3$ (acid)	~ 200	155-200
$\alpha\text{-Al}_2\text{O}_3$	~ 200	0.1-2.95
SiO_2 pellets	250	>30
SiO_2 Evonik Sipernat	75	700
MCM-41	~ 1	900
SBA-15	25	850

Appendix B

Experimental Data

B.1 Experiment data of phase behaviour

Table B1.1 Experimental data of the phase diagram of microemulsion system (water, cyclohexan, Triton X-100 and 1-pentanol) for $\alpha = 0.5$

Mass (g)				α	γ	Phase at temperature													
Water	Cyclohex	Triton	Pentanol			10 °C	15 °C	20 °C	25 °C	30 °C	35 °C	40 °C	45 °C	50 °C	55 °C	60 °C	65 °C	70 °C	
4.75	4.75	0.25	0.25	0.5	0.05	2	2	2	2	2	2	2	3	2	2	2	2	2	
4.5	4.5	0.5	0.5	0.5	0.1	2	2	2	2	2	3	3	2	2	2	2	2	2	
4	4	1	1	0.5	0.2	2	2	2	2	2	2	2	2	2	2	2	2	2	
3.5	3.5	1.5	1.5	0.5	0.3	1	1	1	2	2	2	2	2	2	2	2	2	2	
3	3	2	2	0.5	0.4	1	1	1	2	2	2	2	2	2	2	2	2	2	
2.5	2.5	2.5	2.5	0.5	0.5	1	1	1	2	2	2	2	2	2	2	2	2	2	
2	2	3	3	0.5	0.6	1	1	1	1	2	2	2	2	2	2	2	2	2	
1.5	1.5	3.5	3.5	0.5	0.7	1	1	1	1	1	2	2	2	2	2	2	2	2	
1.33	1.33	4	4	0.5	0.75	1	1	1	1	1	1	2	2	2	2	2	2	2	
1.13	1.13	4.5	4.5	0.5	0.8	1	1	1	1	1	1	1	1	1	1	1	1	1	
0.88	0.88	5	5	0.5	0.85	1	1	1	1	1	1	1	1	1	1	1	1	1	
0.61	0.61	5.5	5.5	0.5	0.9	1	1	1	1	1	1	1	1	1	1	1	1	1	

Table B1.2 Experimental data of the phase diagram of microemulsion system (water, cyclohexan, Span-80 and 1-pentanol) for $\alpha = 0.5$

Mass (g)				α	γ	Phase at temperature													
Water	Cyclohex	Span80	Pentanol			10 °C	15 °C	20 °C	25 °C	30 °C	35 °C	40 °C	45 °C	50 °C	55 °C	60 °C	65 °C	70 °C	
4.75	4.75	0.25	0.25	0.50	0.05	2	2	3	3	2	2	2	2	2	2	2	2	2	
4.5	4.5	0.5	0.5	0.50	0.10	2	2	3	3	3	3	2	2	2	2	2	2	2	
4	4	1	1	0.50	0.20	2	2	3	3	3	3	2	2	2	2	2	2	2	
3.5	3.5	1.5	1.5	0.50	0.30	2	2	2	3	3	3	2	2	2	2	2	2	2	
3	3	2	2	0.50	0.40	2	2	2	2	2	3	2	2	2	2	2	2	2	
2.5	2.5	2.5	2.5	0.50	0.50	2	2	2	2	2	3	2	2	2	2	2	2	2	
2	2	3	3	0.50	0.60	2	2	2	2	2	2	2	2	2	2	2	2	2	
1.5	1.5	3.5	3.5	0.50	0.70	2	2	2	2	2	2	2	2	2	2	2	2	2	
1.33	1.33	4	4	0.50	0.75	1	1	1	1	2	2	2	2	2	2	2	2	2	
1.13	1.13	4.5	4.5	0.50	0.80	1	1	1	1	2	2	2	2	2	2	2	2	2	
0.52	0.52	6	6	0.50	0.92	1	1	1	1	1	1	1	1	1	1	1	1	1	

Table B1.5 Experimental data of the phase diagram of microemulsion system (water, cyclohexan, Triton X-100 and 1-pentanol) for $\gamma=0.5$

Mass (g)				α	γ	Phase at temperature													
Water	Cyclohex	Triton	Pentanol			5 °C	10 °C	15 °C	20 °C	25 °C	30 °C	35 °C	40 °C	45 °C	50 °C	55 °C	60 °C	65 °C	70 °C
2.7	0.3	1.5	1.5	0.1	0.5	2	2	2	2	2	2	2	2	2	2	2	2	2	
2.4	0.6	1.5	1.5	0.2	0.5	2	2	2	2	2	2	2	2	2	2	2	2	2	
2.1	0.9	1.5	1.5	0.3	0.5	2	2	2	2	2	2	2	2	2	2	2	2	2	
1.8	1.2	1.5	1.5	0.4	0.5	1	1	1	2	2	2	2	2	2	2	2	2	2	
1.5	1.5	1.5	1.5	0.5	0.5	1	1	1	1	2	2	2	2	2	2	2	2	2	
1.2	1.8	1.5	1.5	0.6	0.5	1	1	1	1	1	2	2	2	2	2	2	2	2	
0.9	2.1	1.5	1.5	0.7	0.5	1	1	1	1	1	1	2	2	2	2	2	2	2	
0.6	2.4	1.5	1.5	0.8	0.5	1	1	1	1	1	1	1	2	2	2	2	2	2	
0.3	2.7	1.5	1.5	0.9	0.5	1	1	1	1	1	1	1	1	2	2	2	2	2	
0.27	2.73	1.5	1.5	0.91	0.5	1	1	1	1	1	1	1	1	1	1	1	1	1	
0.24	2.76	1.5	1.5	0.92	0.5	1	1	1	1	1	1	1	1	1	1	1	1	1	
0.21	2.79	1.5	1.5	0.93	0.5	1	1	1	1	1	1	1	1	1	1	1	1	1	
0.18	2.82	1.5	1.5	0.94	0.5	1	1	1	1	1	1	1	1	1	1	1	1	1	
0.15	2.85	1.5	1.5	0.95	0.5	1	1	1	1	1	1	1	1	1	1	1	1	1	
0.12	2.88	1.5	1.5	0.96	0.5	1	1	1	1	1	1	1	1	1	1	1	1	1	
0.09	2.91	1.5	1.5	0.97	0.5	1	1	1	1	1	1	1	1	1	1	1	1	1	
0.06	2.94	1.5	1.5	0.98	0.5	1	1	1	1	1	1	1	1	1	1	1	1	1	
0.03	2.97	1.5	1.5	0.99	0.5	1	1	1	1	1	1	1	1	1	1	1	1	1	

Table B1.5 Experimental data of the phase diagram of microemulsion system (water, cyclohexan, Triton X-100 and 1-pentanol) for $\alpha=0.92$

Mass (g)				α	γ	Phase at temperature													
Water	Cyclohex	Triton	Pentanol			10 °C	15 °C	20 °C	25 °C	30 °C	35 °C	40 °C	45 °C	50 °C	55 °C	60 °C	65 °C	70 °C	
0.76	8.74	0.25	0.25	0.92	0.05	2	2	2	2	2	2	2	2	2	3	3	2	2	
0.72	8.28	0.5	0.5	0.92	0.1	2	2	2	2	2	2	2	2	2	3	3	2	2	
0.64	7.36	1	1	0.92	0.2	1	1	1	1	1	1	1	2	2	2	2	2	2	
0.56	6.44	1.5	1.5	0.92	0.3	1	1	1	1	1	1	2	2	2	2	2	2	2	
0.48	5.52	2	2	0.92	0.4	1	1	1	1	1	1	1	2	2	2	2	2	2	
0.4	4.6	2.5	2.5	0.92	0.5	1	1	1	1	1	1	1	1	1	1	1	1	1	
0.32	3.68	3	3	0.92	0.6	1	1	1	1	1	1	1	1	1	1	1	1	1	
0.24	2.76	3.5	3.5	0.92	0.7	1	1	1	1	1	1	1	1	1	1	1	1	1	
0.21	2.45	4	4	0.92	0.75	1	1	1	1	1	1	1	1	1	1	1	1	1	
0.18	2.07	4.5	4.5	0.92	0.8	1	1	1	1	1	1	1	1	1	1	1	1	1	
0.14	1.62	5	5	0.92	0.85	1	1	1	1	1	1	1	1	1	1	1	1	1	
0.1	1.12	5.5	5.5	0.92	0.9	1	1	1	1	1	1	1	1	1	1	1	1	1	

B2. Analysis Results

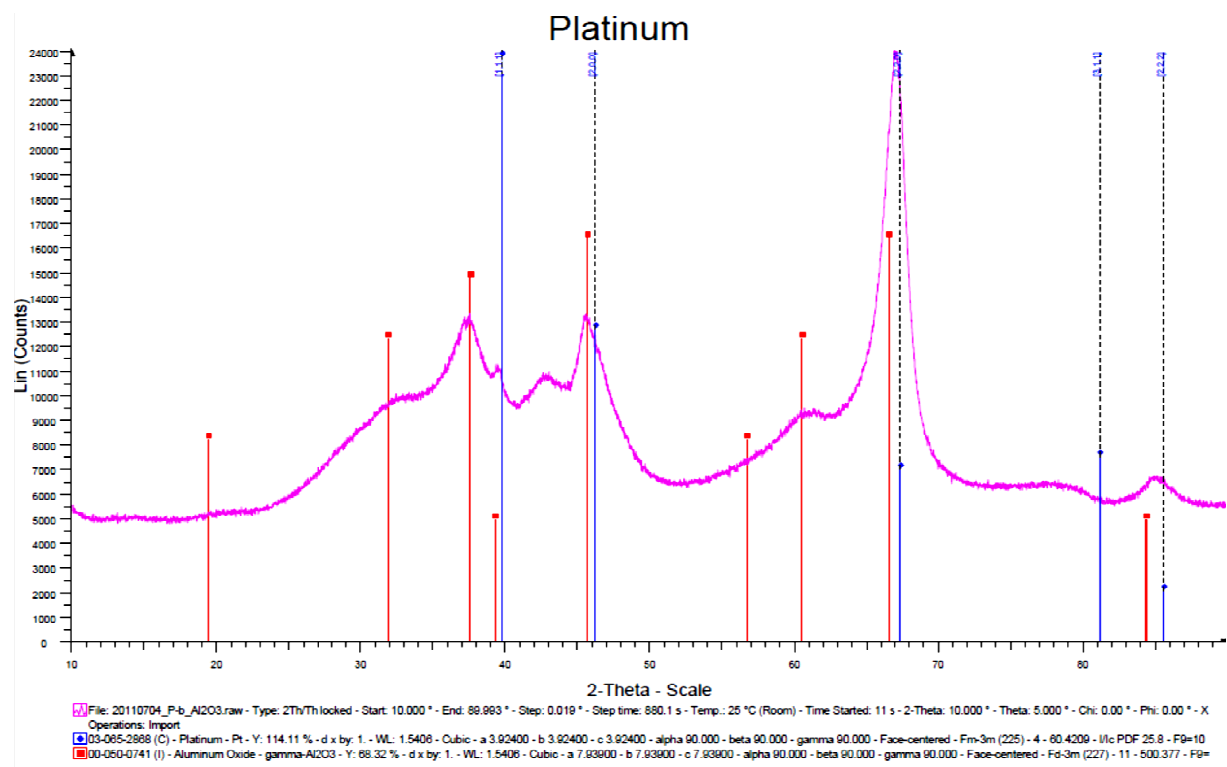


Figure B2.1 XRD diffractions of Pt nanodendrites deposited on the alumina supports

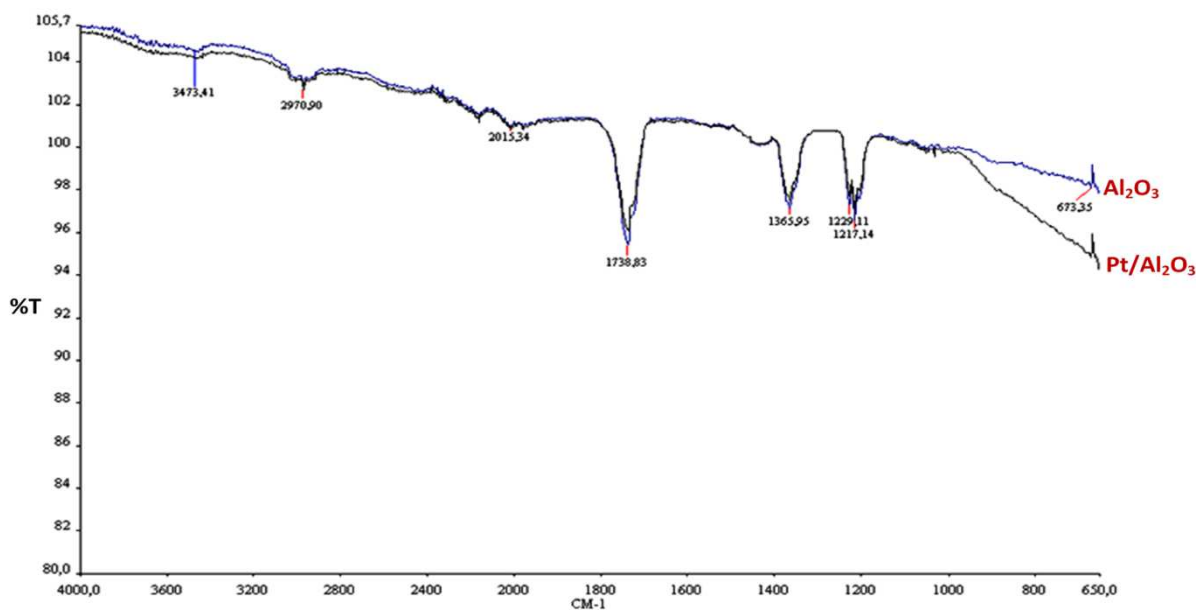


Figure B2.1 Infrared transmission of support Al_2O_3 and Pt/ Al_2O_3

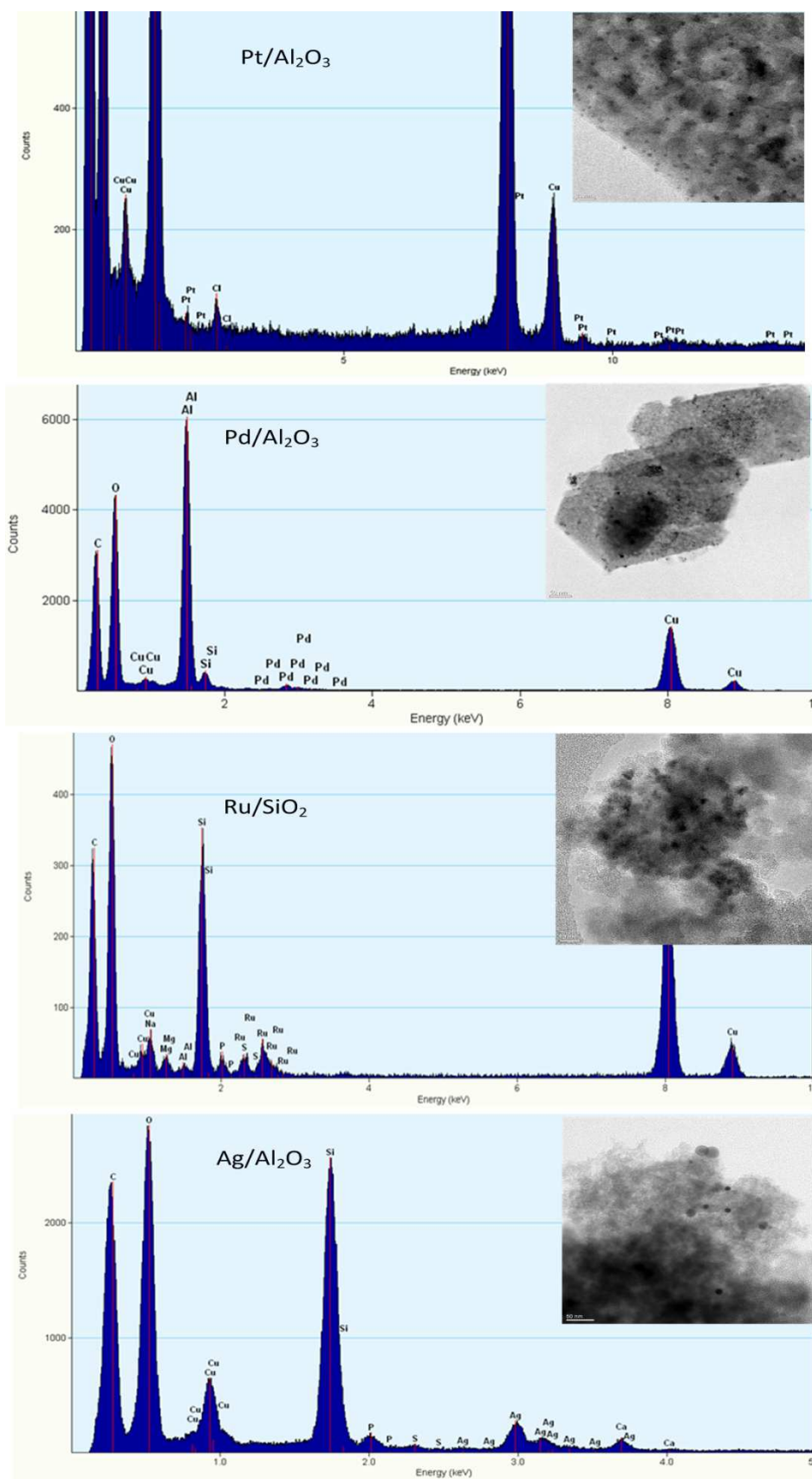


Figure B.2.2 EDX of corresponds supported metal catalysts shown with the TEM images in the insets indicates that the metals are attached on the support.

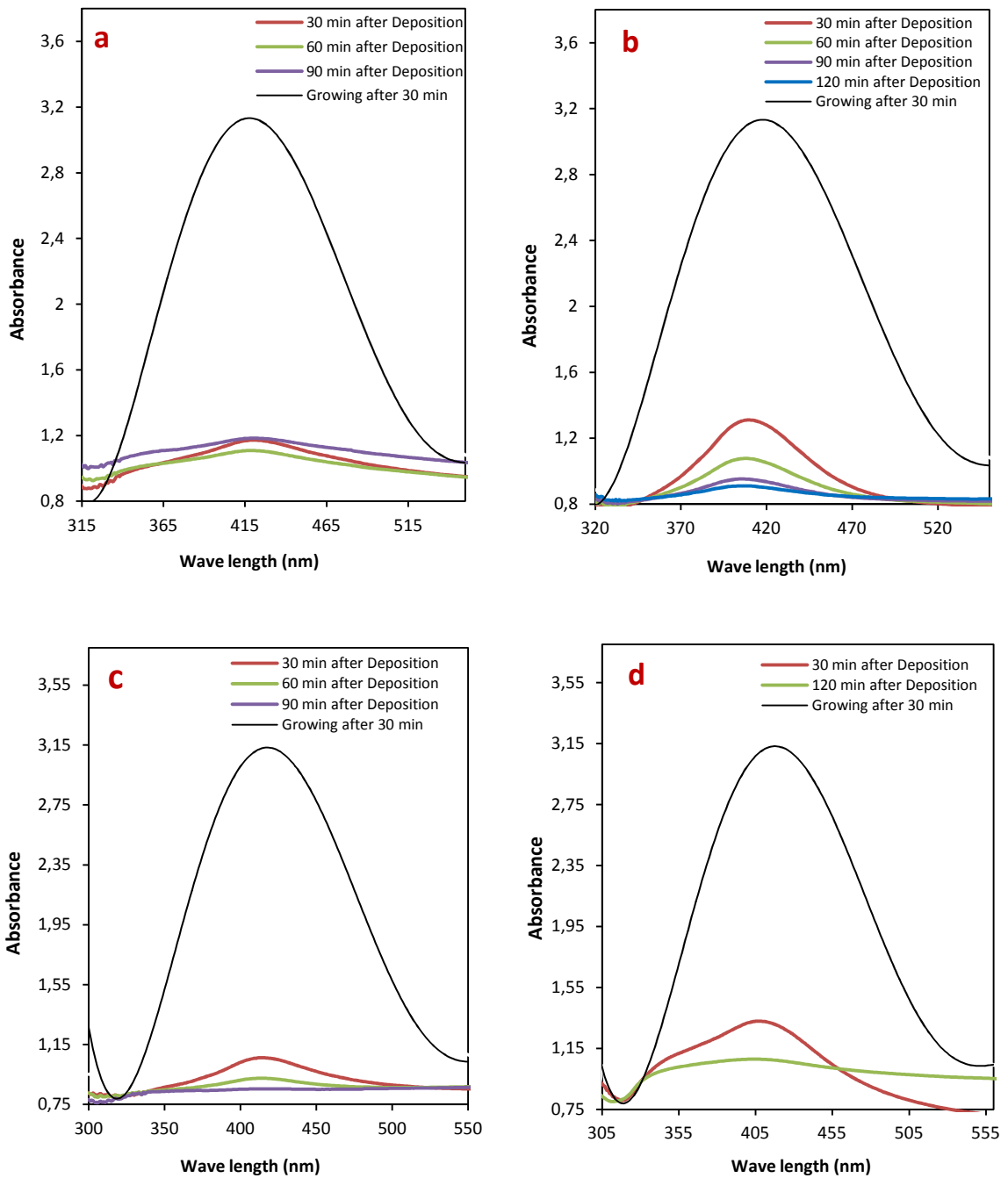


Figure B.2.3. Absorbance of the Ag nanoparticles that are measured with UV-vis spectrometer versus wave length of the microemulsions after growing and during deposition on: a) Evonik-sipernat b) Acid- Al_2O_3 c) Base- Al_2O_3 d) Neutral- Al_2O_3 .

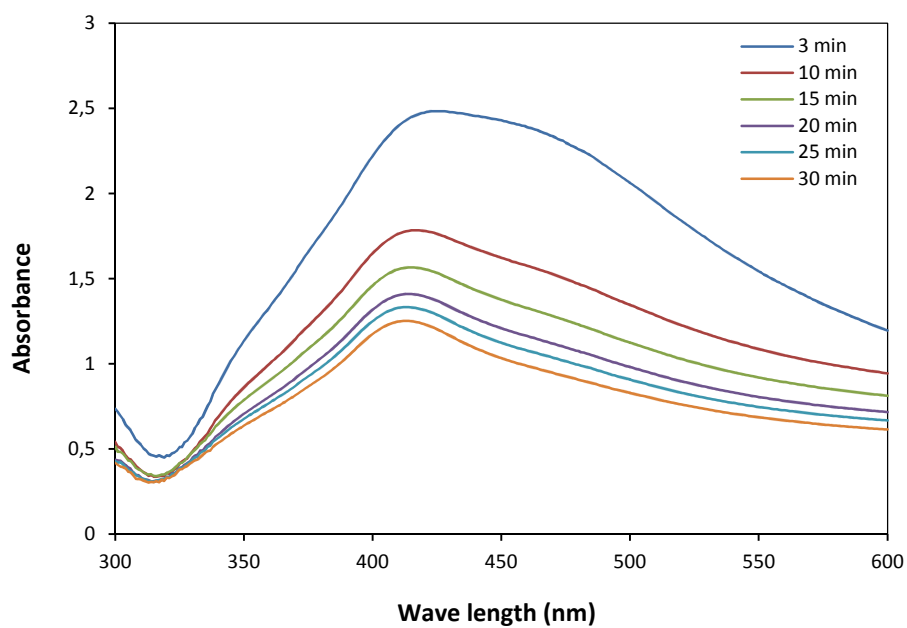


Figure B.2.4 Absorbance pattern for various growing time of the silver nanoparticles against the wave length for 3 mg of Ag ion.

Appendix C

Calculations

C.1 Calculation of the deposition yield and loading of the catalyst

A sample of catalyst is taken as an example. The amount of the Palladium in the water phase of the prepared microemulsions is 1.5 mg. The amount of Pd nanoparticles that are deposited on the Al₂O₃ support (1000 mg) measured with ICP is 0.21 mg.

$$\text{Deposition yield} = \frac{m_{\text{Pd,support}}}{m_{\text{Pd,microemulsion}}} \times 100\% = \frac{0.21 \text{ mg}}{1.5 \text{ mg}} \times 100\% = 14 \%$$

$$\% \text{ loading} = \frac{m_{\text{Pd,microemulsion}}}{m_{\text{support}}} \times 100\% = \frac{0.21 \text{ mg}}{1000 \text{ mg}} \times 100\% = 0.21\%$$

C.2 Calculation of the catalytic activity

The catalytic activity calculation for the above catalysts is following. Figure C.1 shows the volume intake of H₂ curve vs the time as recorded during the hydrogenation.

The calculation of catalytic activity is based on the ideal gas law:

$$P \cdot V = n \cdot R \cdot T$$

$$P \cdot \frac{dV}{dt} = \frac{dn}{dt} \cdot R \cdot T$$

$$r_o = \frac{dr_o}{dt} = \frac{P}{R \cdot T} \left. \frac{dV_0}{dt} \right|_{t=0 \text{ min}}^{t=5 \text{ min}} \quad [=] \frac{\mu\text{mol}}{\text{s}}$$

The activity of the catalyst, which is calculated with the equation:

$$\text{Activity} = \frac{r_o}{m_{\text{Pt}}} \quad [=] \frac{\mu\text{mol}}{\text{s} \cdot \text{g}}$$

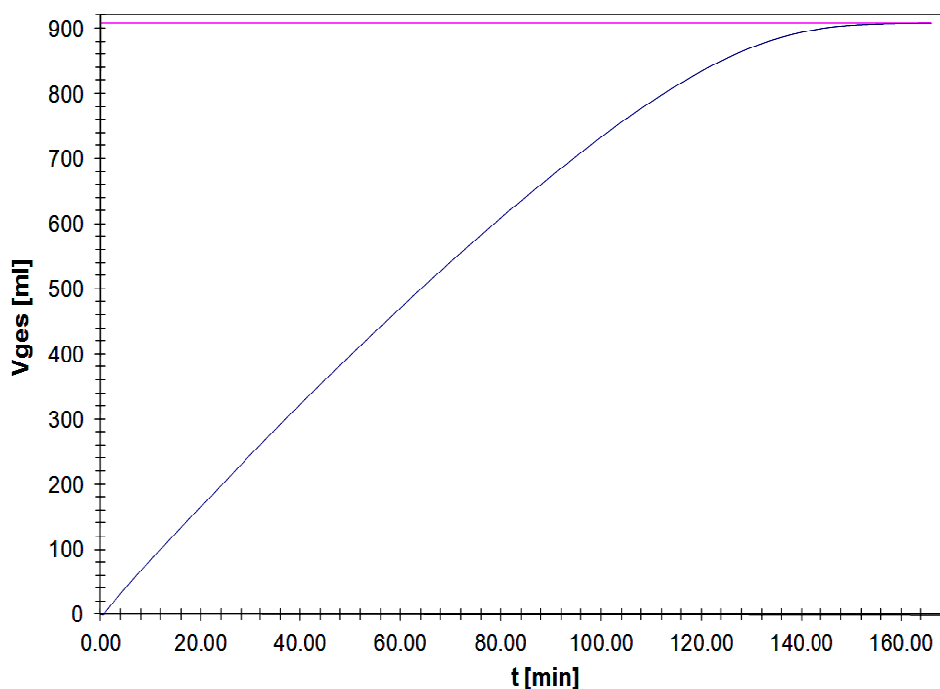


Figure C.2 Hydrogen volume intake versus time in hydrogenation of Methyl Crotonate (4 g) using methanol as solvent ($V = 100 \text{ ml}$) and 0.02 % Pd/Al₂O₃ as catalyst ($m = 640 \text{ mg}$) at 20°C and 1.11 bar.

The data shown in the Table C1 are used to determine the initial hydrogen volume intake against time (dV_0/dt). In this case only the time range from 1 to 5 min is considered in the calculation.

$$\frac{dV_0}{dt} = \left(\frac{V_{t=5} - V_{t=1}}{5 - 1} \right) = 9.2 \frac{\text{ml}}{\text{min}} = 1.5 \cdot 10^{-7} \frac{\text{m}^3}{\text{s}}$$

$$r_0 = \frac{dn_0}{dt} = \frac{P}{R \cdot T} \cdot \frac{dV_0}{dt} = \frac{1.11 \cdot 10^5 \text{ N/m}^2}{8.314 \frac{\text{J}}{\text{mol} \cdot \text{K}} \cdot 293 \text{ K}} \cdot 1.5 \cdot 10^{-7} \frac{\text{m}^3}{\text{s}} = 6.9 \cdot 10^{-6} \text{ mol/s}$$

Table C.2 The recorded volume intake of hydrogen for the first five minutes according to Figure C.2

t	dVdt	V	p
min	mln/min	mln	bar
0.08	0.21875	0.04	1.10125
0.33	0.1203125	0.04	1.1015625
0.58	0.0796875	0.04	1.0975
0.83	8.4484375	2.92	1.1003125
1.08	12.4984375	5.16	1.099375
1.33	12.5421875	7.57	1.099375
1.58	12.6984375	9.98	1.0996875
1.83	11.81875	12.34	1.099375
2.08	12.5328125	14.73	1.0996875
2.33	11.8515625	17.06	1.1003125
2.58	10.915625	19.43	1.099375
2.83	13.33125	21.81	1.0996875
3.08	10.8859375	24.05	1.0990625
3.33	10.66875	26.43	1.1
3.58	12.5078125	28.73	1.0996875
3.83	11.6078125	30.96	1.1003125
4.08	11.2375	33.19	1.099375
4.33	11.8609375	35.46	1.1003125
4.58	10.7046875	37.67	1.1003125
4.83	12.18125	39.85	1.1003125
5.08	11.309375	42.06	1.0996875

The catalytic activity of the catalyst:

$$A = \frac{r_0}{m_{\text{Pd}}} = \frac{6.9 \cdot 10^{-6} \text{ mol/s}}{0.09 \text{ mg}} = \frac{6.9 \cdot \mu\text{mol/s}}{0.09 \cdot 10^{-3} \text{ g}} = 77275 \frac{\mu\text{mol}}{\text{s} \cdot \text{g}_{\text{Pd}}}$$

The value is rounded up to 77000 $\frac{\mu\text{mol}}{\text{s} \cdot \text{g}_{\text{Pd}}}$

C3. Calculation of Pt dispersion

The dispersion of Pt on Al_2O_3 was calculated according to D. J. Bray et al.¹ A triangle section of the TEM picture was selected and within this section the Pt particles were marked. Figure C.3 demonstrates the construction of the Delaunay network over the particle positions. Only those Delaunay triangles (all triangles of which have been outlined in Figure C.3) are used in the analysis.

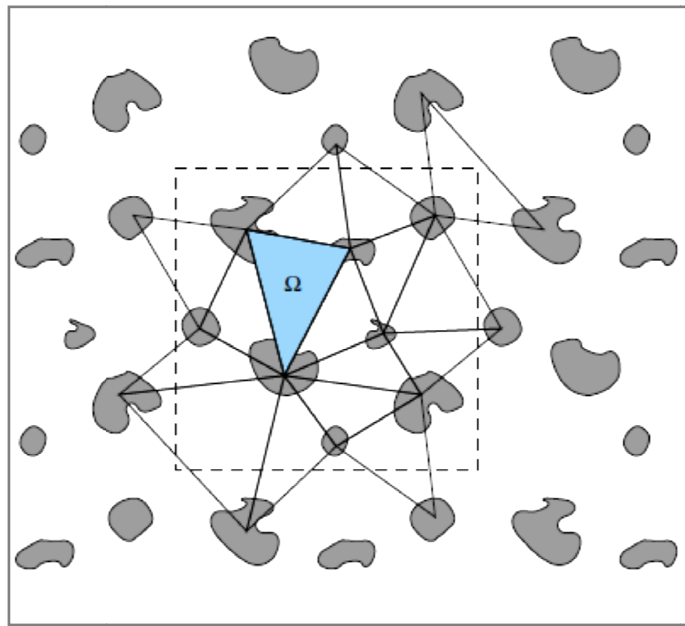


Figure C.3.1 Demonstration of the construction of Delaunay network

The area of marked Pt particles ($\sum a_i$) was calculated and divided by the area of the section (A_{section}) to obtain A_f , the area fraction covered by the nanoparticles. Then, a Pt nanoparticle was selected and connected to the next two Pt nanoparticles near-by to obtain a triangle. This procedure was repeated until all Pt nanoparticles were connected by triangles and the Delaunay network was obtained.

The Area Disorder of the Delaunay network (AD_{Del}) that is a dimensionless quantity with values between 0 and 1 is defined as:

$$AD_{\text{Del}} = 1 - (1 + s_{\Omega}/\bar{\Omega})^{-1}$$

Where $\bar{\Omega}$ is s_{Ω} are the mean and standard deviation of the Delaunay triangles' area, respectively. Finally, A_f and AD_{Del} were used to obtain the quality of dispersion from the classification diagram as shown Figure C.3.2.

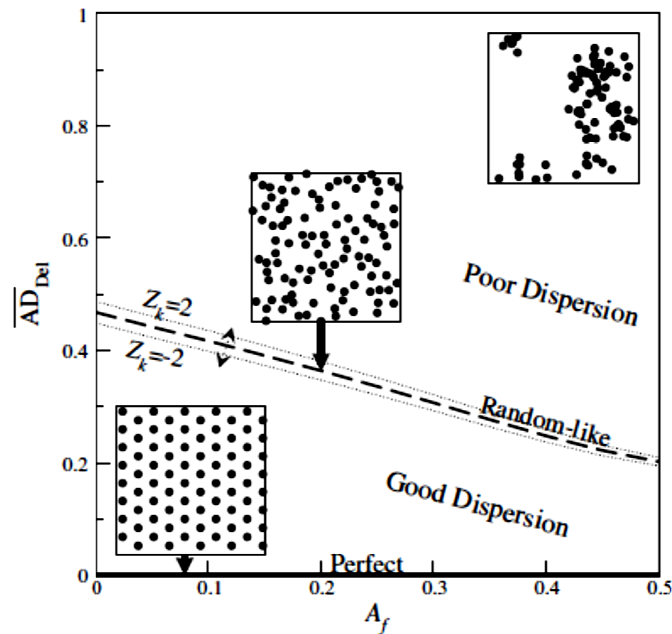


Figure C.3.2 Classification diagram of dispersion for given value of A_f and AD_{Del} ¹

Reference

1. D. J. Bray, S. G. Gilmour, F. J. Guild, T. H. Hsieh, K. Masania, and A. C. Taylor, *Journal of Materials Science*, 2011, **46**, 6437–6452.